CHARGE COLLECTION STUDIES ON INTEGRATED CIRCUIT TEST STRUCTURES USING HEAVY-ION MICROBEAMS AND MEDICI SIMULATION CALCULATIONS

Baonian Guo, B.S., M.S.-Physics, M.S.-Materials Science

Dissertation Prepared for the Degree of

DOCTOR OF PHILOSOPHY

UNIVERSITY OF NORTH TEXAS

May 2000

APPROVED:

Floyd D. McDaniel, Major Professor and Coordinator of the program in Physics Ph.D.
Jerome L. Duggan, Minor Professor
Barney L. Doyle, Committee Member
Samuel E. Matteson, Committee Member and Chair of the Department of Physics
Duncan L. Weathers, Committee Member and Graduate Advisor of the Department of Physics
C. Neal Tate, Dean of the Robert B. Toulouse School of Graduate Studies

Guo, Baonian, Charge Collection Studies on Integrated Circuit Test Structures using Heavy-Ion Microbeams and MEDICI Simulation Calculations. Doctor of Philosophy (Physics), May 2000, 134 pp., 3 tables, 38 illustrations, references, 163 titles.

Ion induced charge collection dynamics within Integrated Circuits (ICs) is important due to the presence of ionizing radiation in the IC environment. As the charge signals defining data states are reduced by voltage and area scaling, the semiconductor device will naturally have a higher susceptibility to ionizing radiation induced effects. The ionizing radiation can lead to the undesired generation and migration of charge within an IC. This can alter, for example, the memory state of a bit, and thereby produce what is called a "soft" error, or Single Event Upset (SEU). Therefore, the response of ICs to natural radiation is of great concern for the reliability of future devices. Immunity to soft errors is listed as a requirement in the 1997 National Technology Roadmap for Semiconductors prepared by the Semiconductor Industry Association in the United States. To design more robust devices, it is essential to create and test accurate models of induced charge collection and transport in semiconductor devices. A heavy ion microbeam produced by an accelerator is an ideal tool to study charge collection processes in ICs and to locate the weak nodes and structures for improvement through hardening design. In this dissertation, the Ion Beam Induced Charge Collection (IBICC) technique is utilized to simulate recoil effects of ions in ICs. These silicon or light ion recoils are usually produced by the elastic scattering or inelastic reactions between cosmic neutrons or protons and the lattice atoms in ICs. Specially designed test structures were experimentally studied, using microbeams produced at Sandia National

Laboratories. A new technique, Diffusion Time Resolved IBICC, is first proposed in this work to measure the average arrival time of the diffused charge, which can be related to the first moment (or the average time) of the arrival carrier density at the junction. A 2D device simulation tool, the MEDICI code, and heavy-ion microbeams are used to calculate and measure charge collection and relative arrival time on stripe-like test junctions. The MEDICI simulation is in qualitative and sometimes even quantitative agreement with the microbeam measurements. The amount of charge collection and the magnitude of average arrival time for diffused charge collection can be crucial to understanding and mitigating radiation induced circuit malfunctions during normal IC operations.

ACKNOWLEDGEMENTS

I am grateful to Dr. Floyd D. McDaniel, my research advisor, for his expert advise and supportive discussions in the course of my graduate study. I wish to thank him (and Dr. Linda McDaniel) for making thoughtful criticisms, putting up with numerous revisions, and translating the draft copy to the present form.

This work would not be possible without the help from many individuals and institutions. I am very grateful to Drs. Steve N. Renfrow, David S. Walsh, and Barney L. Doyle of Sandia National Laboratories for conducting microbeam experiments at the start-of-the-art microprobe facility. Thanks also go to Drs. Thomas J. Aton, Eric Smith, and Robert C. Baumann of the Silicon Technology Development of Texas Instruments Inc. for the kindness of providing test structures and simulation parameters. Especially, I wish to express my thanks to Dr. Doyle for many wise and valuable suggestions in the different states of the project. I also wish to thank Dr. Baumann for his support and encouragement during the computer simulations.

It is my privilege to acknowledge the committee members of academic guidance. I would like to thank Drs. Sameer A. Datar, Mohamed El Bouanani, Changyi Yang, and the crew of the Ion Beam Modification and Analysis Laboratory of the University of North Texas for technical support and useful discussions.

Finally, the most important support and encouragement through this journey have come from my wife, to whom this manuscript is dedicated. I would like to thank my parents for their love and encouragement over the years.

I also wish to acknowledge the financial support from the National Science Foundation, the State of Texas Coordinating Board - Texas Advanced Technology Program, and the Robert A. Welch Foundation. Work at Sandia supported by the U.S. DoE under contract DE-AC04-94AL85000.

TABLE OF CONTENTS

Page

LIST OF TABLES

Page

LIST OF ILLUSTRATIONS

Page

ACRONYMS

ADC	Analog-to-Digital Converter (ADC)
ASER	Accelerated Soft Error Rate
BGN	Band Gap Narrowing
BPSG	Borophososilicate Glass
CA	DAVINCI/MEDICI Circuit Analysis module
CCD	Charge Coupled Device
CCS	Carrier-Carrier Scattering
CFD	Constant Fraction Discriminator
CMOS	Complementary-Metal-Oxide-Semiconductor
CONSRH	CONcentration dependent Schockley-Real-Hall carrier lifetime
DMA	Direct Memory Access
DR	Depletion Region
DRAM	Dynamic Random Access Memory
DRB	Depletion Region Boundary
DTRIBICC	Diffusion Time Resolved Ion Beam Induced Charge Collection
DUT	Device Under Test
DVM	Digital Voltage Meter
ECC	Error Correcting Code
EDAC	Error Detection And Correction
ERDA	Elastic Recoil Detection Analysis
FDAC	Fast Data Acquisition Crate
FET	Field-Effect-Transistor
FHINM	Focused Heavy-Ion Nuclear Microprobe
GPIB	General Purpose Interface Bus
IBICC	Ion Beam Induced Charge Collection
IBIL	Ion Beam Induced Luminescence
IBMAL	Ion Beam Modification and Analysis Laboratory
IBMRL	Ion Beam Materials Research Laboratory
IC	Integrated Circuits
IEEM	Ion-Electron Emission Microscopy
IMT	Ion Micro-Tomography

LET	Linear Energy Transfer
MBU	Multiple Bit Upset
MOSFET	Metal-Oxide-Semiconductor Field Effect Transistor
MPSYS	MicroProbe SYStem
NIM	Nuclear Instrument Module
NRA	Nuclear Reaction Analysis
PDE	Partial Differential Equation
PIXE	Particle Induced X-ray Emission
PSD	Position Sensitive Detector
RBS	Rutherford Backscattering Spectrometry
R-G	Recombination and Generation
RISC	Reduced Instruction Set Computer
SCSI	Small Computer System Interface
SE	Secondary Electron
SEE	Single Event Effect
SER	Soft Error Rate
SEU	Single Event Upset
SNL	Sandia National Laboratories
SRAM	Static Random Access Memory
SRH	Schockley-Real-Hall theory
SRIM	The Stopping and Range of Ions in Matter
SSER	System Soft Error Rate
STIM	Scanning Transmission Ion Microscopy
TAC	Time-to-Amplitude Converter
TCAD	Technology Computer Aided Design
TEM	Transmission Electron Microscopy
TRIBICC	Time Resolved Ion Beam Induced Charge Collection
UNT	University of North Texas
VME	VersaModule Eurocard
WNR	Weapons Neutrons Research facility at Los Alamos National Laboratory

CHAPTER 1

INTRODUCTION

Natural Radiation Induced Effects on Semiconductor Devices

At the Integrated Circuit (IC) chip level, electronic information can be fundamentally expressed as a combination of states of digital electronic signals. The states of the signals, “0” or “1”, are determined by small packets of charge in the circuits. Any electronic noise, such as originating from a noisy power supply, may cause a change in the signals by modifying the small packets of charge. As semiconductor technology strives for higher circuit densities (product functionality), higher bandwidths (speed), and lower power requirements (battery operation, portability), the robustness of individual circuit elements decreases due to reductions in physical feature sizes and operating voltages and fewer electrons in a charge packet indicating a zero or a one data state. As the charge signal defining data states is reduced by voltage and area scaling, the device will naturally have a higher susceptibility to ionizing radiation induced effects in semiconductor devices.

The effects of radiation on electronic systems were observed from 1954 to 1957 during above ground nuclear bomb tests. “Hard-fail” was described as the failure of a device after a heavy dose of radiation. Other spurious electronic signals were attributed

to electronic noise from the nuclear bomb's electromagnetic pulse and termed as "soft-fails".

In 1975, the first observation of soft errors in the space environment was reported [1]. Space borne electronic systems are exposed to a harsh radiation environment: cosmic rays (solar energetic particles or galactic cosmic rays from deep space) and trapped protons within the Earth's geomagnetic belt. Based on an analysis of the four anomalies that occurred on satellites during 17 satellite-years of operation, 100 MeV iron ions in the solar wind were suggested as a principal source of satellite soft errors [1].

In 1978, May and Woods of Intel reported the first evidence of sea level soft errors from energetic particle impact [2]. They discovered that the problem originated from the ionizing decay products (alpha particles) of radioactive atoms, such as thorium, uranium etc., which exist in trace amounts in the IC fabrication materials. On-chip sources of natural alphas in ICs include the ceramic substrate, alumina, copper, aluminum metallization, gold used for bond wires and plating, and lead-tin solder.

To ensure the reliable performance of devices, ionizing radiation induced effects, such as a gradual deterioration of electronic characteristics or transient malfunctions of microcircuits, have to be evaluated [3]. Total dose effects are due to the accumulation of trapped charges from many forms of radiation that affect the electronic characteristics in the long term. On the other hand, the functional disturbances induced by ionizing particles along the ion tracks are called Single Event Effects (SEEs). One of the SEE subcategories, Single Event Upset (SEU), or soft error, is the primary cause for concern in digital devices, especially for SRAMs and DRAMs (Static and Dynamic Random Access Memories), and microprocessors. For example, exposure to ionizing radiation can

lead to the undesirable generation and migration of charge within an SRAM or DRAM device. If the induced charged collection by the IC charge storage cell exceeds a critical threshold charge, the memory state of a bit can be altered, thereby producing an SEU.

The physical picture of alpha induced soft errors can be described in the following manner. Low energy alpha particles, emitted from radioactive isotopes in for example the packaging materials, pass through an IC, deposit energy along the penetrating track, and generate excess electron-hole pairs. If the induced charge is in the neighborhood of a device junction, the charge can be collected before electron-hole recombination occurs. High electric field gradients present near the junction can enhance charge separation and collection (the funneling effect) [4-6]. Electron-hole pairs developed along the penetrating ion track can partially collapse the junction depletion region. The voltage drop previously on the junction depletion region is partially balanced by the voltage drop across the substrate. Along the ion track, the track conductivity is large near the central line of the track and becomes smaller with increasing radial distance from the central line. The electric field in the upper track region is weakest near the central track and stronger at larger radial distances. This means that central equipotential surfaces form a funnel shape [7,8]. This distortion of local electrical fields can sometimes assist the induced minority charge in the substrate to drift toward the device junctions, which would have otherwise dissipated through diffusion into the silicon bulk. If funneling occurs, it will lead to a large amount of charge collected at the struck junction and result in greatly increased susceptibility of the device to SEUs. Also, this funneling assisted charge collection will localize more induced charge around the struck junction, and less charge will diffuse away to be collected by other junctions (FIGURE 1). When the

induced charge is shared and collected among charge storage cells, Multiple Bit Upsets (MBUs) can occur. A key parameter here is the stopping power or energy loss per unit track length, which is a measure of the deposited energy by the incoming particle in the medium. The induced charge is due to the electronic contribution of the stopping power, referred to as Linear Energy Transfer (LET) in units of MeV/mg/cm^2. The program SRIM, which simulates ion implantation in amorphous materials, is routinely used to calculate the stopping power [9].

The critical volume V_c is defined as the volume enclosing the ionizing particle track, which contains just enough induced charge (or critical charge Q_c) to cause a circuit upset. Since Q_c is a function of the design and operation of the IC, the above definition is not totally appropriate in all circuit cases. For example, Q_c may not be a circuit constant but can vary with the timing of the strike relative to the dynamic operation of the circuit, the location of the strike relative to the sensitive node, charge pulse shape, power supply voltages etc. [10,11]. Still, Q_c remains the single most useful comparative measure of the soft error tolerance of a circuit type. Generally, the critical charge for an unhardened device decreases with reduced feature sizes. FIGURE 2 shows SEU critical charge (Q_c) versus feature size (l) for a broad range of technologies. The curve shows the l^2 scaling trend together with a lack of dependence on the device technology [12].

To study and model SEUs, the SEU cross section is another important parameter. This parameter is the product of the number of upsets and the secant of the tilt angle of a beam divided by the beam fluence. From different ion species and different energies, induced SEU cross-sections, the sensitive depth, and therefore the sensitive volume can be experimentally determined [13-16].

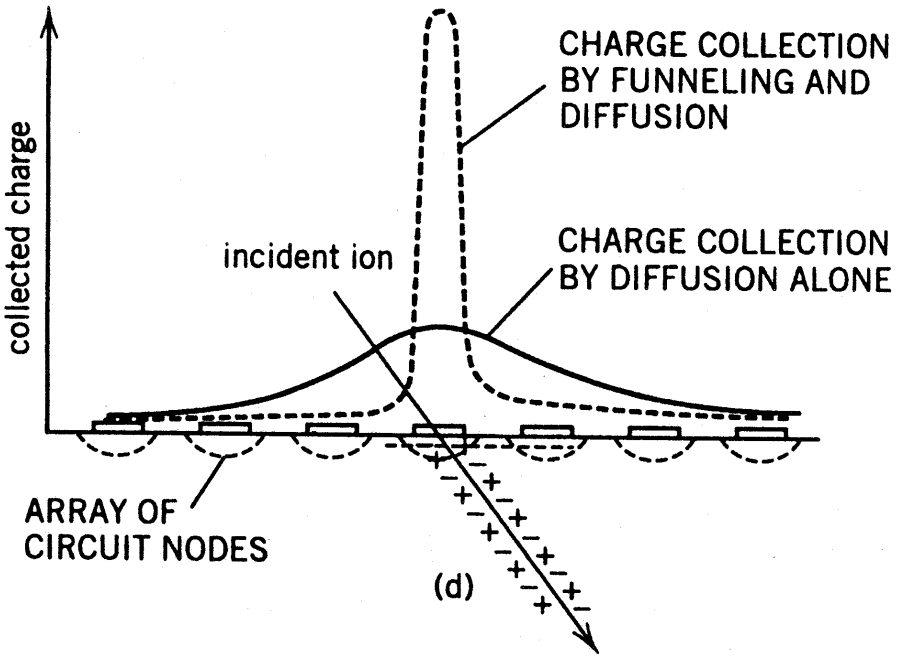

FIGURE 1. The charge collection profiles over a circuit array show that the funneling assisted charge collection is localized to the directly struck junction rather than diffused to nearby junctions [7].

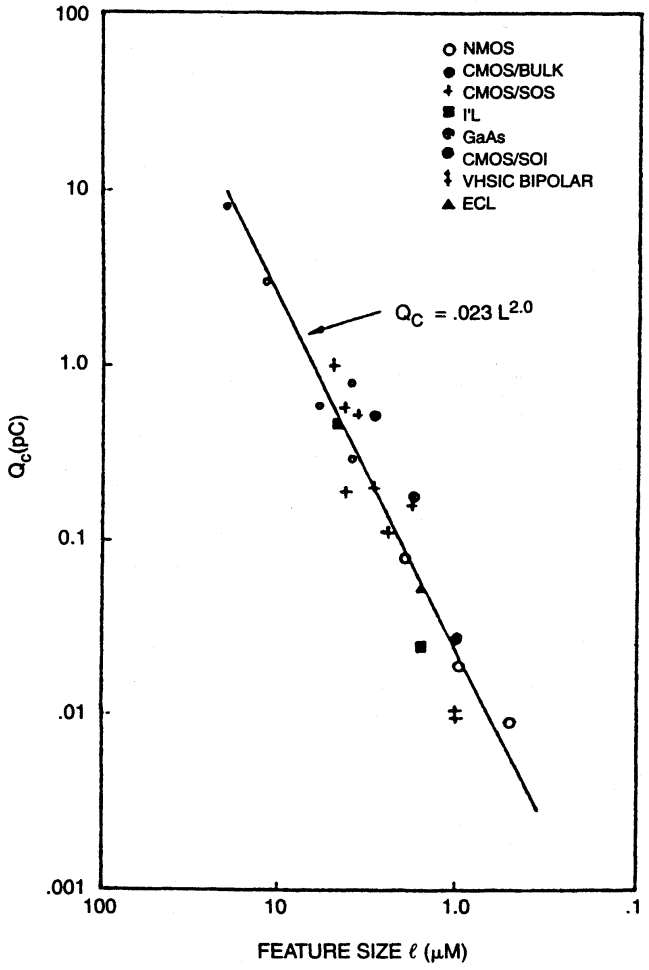

FIGURE 2. SEU critical charge (Q_c) versus feature size (l) for a broad range of technologies. The curve shows the l^2 scaling trend with the lack of dependence on the device technology [12].

Since the discovery of SEUs in DRAMs in the terrestrial environment [2], this phenomenon has been investigated by chip manufacturers. Extensive studies and design initiatives have been undertaken to make electronic devices immune to such ionizing radiation [17-33]. For example, IBM undertook a very large proprietary effort to understand the phenomenon of upsets at ground level. These efforts included: field testing of memories with environmental monitoring, accelerated testing using cyclotron beams, and detailed model development coordination with device designers [34]. So far, several processing techniques have been proposed and realized to mitigate charge collection at sensitive nodes, such as a shallow well with a second junction, a thin epitaxial layer, retrograde doping within the well, etc. Also, detection and correction of soft errors can be done with extra circuitry. For example, a Hamming Error Detection And Correction (EDAC) code can detect two errors and correct one within the Error Correction Code (ECC) word group [35]. Logic Hamming groups can be disbursed physically in the memory array to reduce MBU (speed is scarified). The alpha particle flux emitted by packaging and processing materials has been reduced to the tolerable levels of <0.01 alpha/cm^2-hr [36], and an alpha induced System Soft Error Rate (SSER) test procedure has been standardized using alpha sources to conduct the Accelerated SER (ASER) tests [37]. However, the SER at ground level can not be all attributed to the alpha induced SEUs.

As early as 1979, Ziegler and Lanford suggested that cosmic ray particles could be a source responsible for SEUs in DRAMs and other electronic devices [38]. Since then, many reports have shown that the cosmic ray neutrons are a significant source of errors in electronic devices at aircraft flight altitudes [39-42]. Recent research has

demonstrated that cosmic ray neutrons are the primary SEU cause in SRAMs, DRAMs, and other devices even at ground level [43,44]. FIGURE 3 shows the comic ray induced SEU error rate (SEU bit error rate per transistor per day) as a function of Q_c for various sensitive region transistor dimensions of a CMOS SRAM (Complementary-Metal-Oxide-Semiconductor SRAM) [45]. As the dimension of the critical volume V_c decreases for smaller feature sizes of ICs, the critical charge Q_c also tends to decrease due to voltage scaling, lower cell capacitance, etc. High-energy neutrons produced by cosmic rays can be the major contributor to the SER for the current 64M DRAM generation and for future generations of memory devices compared with the alpha-induced SER. The reason is the higher LET for neutron-induced recoils or reaction products than that for alpha particles within the smaller critical volume [46].

The sensitivity of ICs to natural radiation is increasing as a result of reduced feature sizes, particularly for SRAMs and DRAMs. The response of ICs to natural radiation is therefore of great concern for the reliability of future devices as well as other failure mechanisms [47]. Immunity to soft errors is listed as a requirement in the 1997 National Technology Roadmap for Semiconductors prepared by the Semiconductor Industry Association in the United States [48].

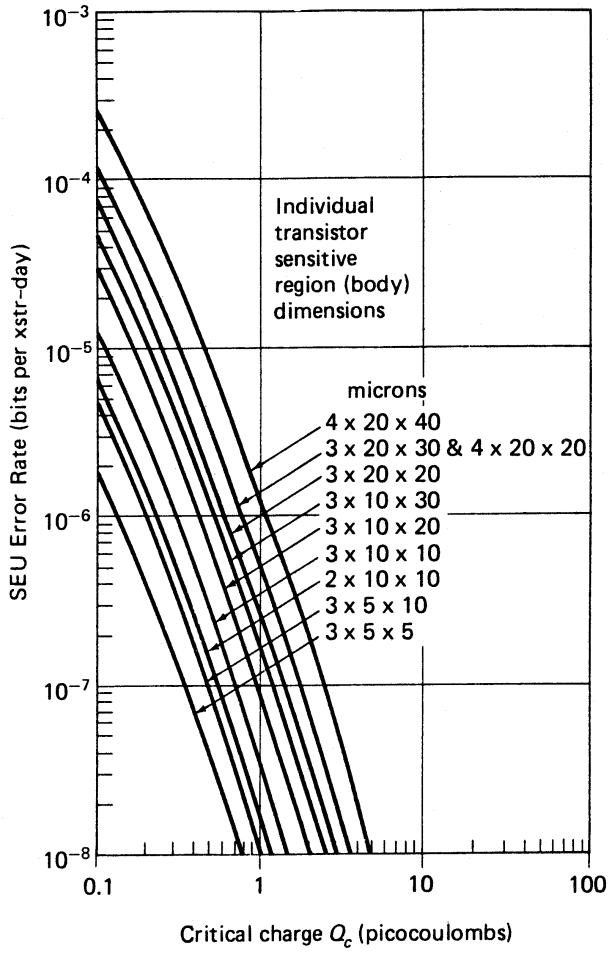

FIGURE 3. Comic ray induced SEU error rate (SEU bit error rate per transistor per day) as a function of Q_c for various sensitive region transistor dimensions of a CMOS SRAM [45].

The primary cosmic ray flux consists of 92% protons, 6% alpha particles, with the remaining 2% being heavy nuclei with energies up to ~10^{19} eV. The distribution of trajectories of these particles can be considered isotropic and source independent [49,50]. When cosmic ray particles penetrate the atmosphere, they create a cascade of secondary particles through spallation interactions with nitrogen and oxygen nuclei, which create further cascades and hence some particles may reach sea level. The maximum cascade density of particles occurs at about 15 km above the surface, with increasing absorption as they approach the surface. The particle cascades at sea level include protons, neutrons, pions, muons, electrons, photons, etc. At ground level, the flux of particles is more than 97% neutrons [50]. The effects of the induced charge with other particles in semiconductor materials are minor in comparison to that of cosmic ray neutrons and protons.

Neutrons and protons can lead to recoil reactions and heavy ion generation. Because of the small interaction cross section, high-energy neutrons will for the most part pass through silicon without interacting. For example, only one out 40,000 incident neutrons will interact within 10 μm of the device silicon surface [50]. However, whenever neutrons collide with the atomic nuclei in devices, the collision typically results in the emission of secondary nuclear fragments. These fragments consist of pions, protons, neutrons, deuterons, tritons, helium, magnesium, oxygen, carbon, etc. With the exception of neutrons, all of these reaction products contribute to the creation of electron-hole pairs. Neutrons can only be stopped by neutron-nucleus interactions, which produce secondary charged fragments. Each of these fragments induces hundreds of fC of charge within a few microns, which can upset almost any circuit [51]. It is estimated that almost

every silicon-neutron collision within 1 μm of an IC will result in a soft error [50]. It has been observed that the thermal neutrons (E~ 0.025 eV) can also lead to SEUs. In this case, the mechanism is the interaction of thermal neutrons with ^{10}B, a fractional component in the borophososilicate glass (BPSG) within the glassivation layer over the die. This interaction produce alpha particle by the $^{10}B(n,\alpha)^{7}Li$ reaction. The energy deposition by the alphas leads to the upsets [52]. Since boron is a common dopant in chip fabrication, a very similar mechanism was investigated earlier with respect to the ^{10}B content of boron dopant in devices [53]. Both the 1.5 MeV alpha and the 0.8 MeV Li, produced by thermal neutron interactions with ^{10}B, were found to cause upsets [53].

Protons with energies from 10 MeV to hundreds of MeV exist in the Earth's geomagnetic belts with very high flux densities. In ICs, the direct ionization by protons is of less concern than the effects by secondary reactions. These reactions include elastic scattering of the target nucleus and inelastic reactions with the target nucleus. Inelastic scattering can lead to the emission of alpha particles and gamma rays, recoil of the daughter nucleus, and neutron spallation [51,54-56]. Thus, both neutrons and protons can lead to circuit effects similar to that produced by heavy ions through recoil reactions and heavy ion generation. Since the proton flux is significantly attenuated as protons approach sea level, neutrons are considered as the major source of the SEEs at ground level [50].

The shape of the neutron spectrum is similar at all altitudes. The integrated neutron flux is greatest between 1 and 10 MeV, and the 10-100 MeV neutron flux falls off approximately linearly with latitude. The maximum neutron intensity is maintained at altitudes between 9 km and 18 km, and the integrated neutron flux above 1 MeV varies

from about 1 $cm^{-2}s^{-1}$ at high altitudes down to 10^{-3} $cm^{-2}s^{-1}$ at sea level. Since the neutron spectrum produced by the Los Alamos National Laboratory Weapons Neutrons Research (WNR) facility is generated through high-energy proton spallation on a tungsten target, it is essentially identical to the neutron production mechanism for atmospheric neutrons. The shape of the WNR neutron spectrum is very similar to that for atmospheric neutrons, and one hour in the WNR beam is equivalent to $6\sim9x10^7$ hours at ground level. The SEU cross section obtained through Accelerated SER (ASER) testing with the WNR neutron beam was about three orders magnitude higher than that obtained with thermal neutrons [44]. Therefore, it can be concluded that high-energy cosmic neutrons are the main cause of SEUs at ground level [44].

Besides the WNR neutron spallation source, there are two other types of research methods that have been proposed and used to conduct ASER testing. IBM uses 150 MeV protons to simulate the cosmic neutrons and scales the measured SEU cross sections so that the results with proton beams can also be used for neutrons [57]. Boeing uses a 14 MeV neutron generator combined with theoretical calculations to justify and normalize the experimental results before relating them to atmospheric neutrons [58]. Due to the spectrum similarity between the WNR neutrons and atmospheric neutrons, the WRN neutron source probably is the best for ASER testing.

Experimental Research Methodology

A limitation of using a neutron beam for the ASER testing is that the beam is difficult to control experimentally. An alternative experimental procedure was demonstrated using energetic heavy ions directly striking the devices, thus simulating the typical recoil nuclei from neutron collisions [59-61]. The induced dense plasma around the track of the high-energy heavy ions can be regarded as a reasonable experimental analogue for strongly ionizing cosmic ray particles passing through devices.

It is important to evaluate the completed devices, such as ASER testing using the WNR neutron beam, for susceptibility to the ionizing radiation induced effects. To design more robust devices, it is also essential to create and test accurate models of induced charge collection dynamics within devices [62], critical charge formation [10,11], and predicted SER rates in standard environments [63-67]. Such model-based testing requires energetic heavy ions whose number, arrival time, spatial location, energy, and incidence angle can be controlled, vis-à-vis their interaction with ICs. As the sizes of the *pn* junctions decrease and their speed increases, more precise spatial focusing and higher fluxes will be required. Experiments with better spatial and time resolution would produce less ambiguous and easier to analyze results. More precise comparisons to theoretical models would also be possible. A heavy ion microbeam produced by an accelerator is an ideal tool to study charge collection processes in devices and to locate the weak nodes and structures for improvement through hardening design [68].

Traditionally, a broad beam obtained from an accelerator has been used to measure the device response. It is very difficult for these kinds of measurement to

identify and determine the mechanisms responsible for upset. Since the early 1980's, apertured microbeam systems have been used to study charge collection [59-61,69,70]. With an apertured microbeam, a pin-hole aperture is used to collimate the ion beam to a diameter of several μm. A specific test region is exposed to the microbeam by moving the device with an x-y stage. In all apertured systems, the distance between the aperture and the sample (~0.5 cm) results in ion beam blooming and limits the spot size to about 2 μm. Also, the scattering of the beam from the aperture deteriorates beam size and quality. Microbeam systems using magnetic or electrostatic focusing lenses with rastering ability have been developed and are now widely used [68]. Beam spot size as small as 0.05 μm has been achieved [71]. The focused microbeam can deliver much brighter beam with sub-micron spatial resolution. It has been widely used to study charge collection processes in ICs and to locate weak nodes and structures, which are candidates for improvement through design hardening [72-83].

In the microbeam experimental techniques, SEU imaging [84,85] and Ion Beam Induced Charge Collection (IBICC) [86-89], are two complementary techniques to study the device response. SEU imaging directly indicates those weak nodes within a device, where upsets or malfunctions are caused when exposed to energetic heavy ions. However, SEU imaging does not provide quantitative information concerning the amount of charge that produced the upsets. IBICC provides a means to quantitatively measure the amount of charge collected by these circuit nodes when struck by ions, but does not reflect the effect of the ion strike on the circuit's operation. The combination of these two techniques allows quantitative investigation of the upset process within a circuit [87]. Microbeam techniques are also essential for transient charge collection measurement to

ensure that a signal arises from only the region of interest. Time Resolved IBICC (TRIBICC) has been proposed by Sandia National Laboratories (SNL) and it is used to measure the transient charge collection on MOSFET structures using a high bandwidth data acquisition system and a microbeam [90]. TRIBICC also provides a means to experimentally verify computer simulation results.

Modeling Methodology

As the feature sizes of devices shrink below 0.5 micron, the complexity and functionality of devices have reached the level where the cost of manufacturing test lots for design studies is prohibitive. Therefore, Technology Computer Aided Design (TCAD) tools, including device simulations, are widely used at all levels of device design and manufacture. TCAD enables comprehensive studies to optimize technology with much less cost and time and therefore drastically reduce the design cycle, which is especially important for the semiconductor industry. At the same time, experiments are necessary to validate models and establish their limitations. Therefore, an effective design process requires a combination of experimental studies as well as TCAD simulations.

Once a process for device fabrication is established, it is necessary to evaluate the electrical characteristics of the design through device modeling. The drift-diffusion model is one of most commonly used models in device simulation due to its computing efficiency. In the drift-diffusion model, the device equations (Poisson equation, and current continuity equations, and energy balance equations) can be made discrete and

solved using finite-element techniques. When high energetic particles penetrate through devices, electron-hole pairs are generated along the ion tracks. The effects of electron-hole pairs can be incorporated into the drift-diffusion model through the generation terms. Therefore, computational modeling can provide insight into the effects of ionizing radiation on microelectronic devices [91-93]. Also, simulations can assist technology developers in making design decisions to improve the SEU hardness of a particular technology. These predictive simulations enable improved process and design optimization, lower testing costs, the discovery of new SEU mechanisms, and potentially new SEU hardening techniques [94,95].

Since the drift-diffusion charge transport is influenced by the potential and carrier concentration gradients, the simulation requires 3D tools to deal with 3D problems [95], which require intensive computing resources. Simplified 1D or 2D simulations have been used and provide an enormous amount of insight into how the induced charge is transported within devices. An example is the discovery of the field-funneling effect by IBM using the two-dimensional finite-element device simulator FIELDAY [4-6].

A wide variety of computer simulation tools based on theoretical models are commercially available to simulate the effects of particle strikes on sensitive nodes on devices. For example, Avant! Corporation provides the device simulation software package, DAVINCI for 3D device simulations, and MEDICI for 2D simulations [96]. Both packages are based on the drift-diffusion models. Both simulation codes account for effects such as Schockley-Read-Hall and Auger recombination, carrier mobility (affected by concentration, field, and carrier-carrier scattering), etc. To simulate the induced charge in the devices, a localized generation of electron-hole pairs can be used.

DAVINCI/MEDICI also incorporate a circuit simulation module, and its mix-mode (device and circuit) simulation abilities are important to study the responses of loaded devices during ion strikes.

Present Work

In the present work, Ion Beam Induced Charge Collection (IBICC) is utilized to simulate recoil effects in ICs. As was mentioned earlier, these silicon or light ion recoils are usually produced by cosmic neutrons or protons interacting with the lattice atoms in ICs through elastic scattering or inelastic reactions. FIGURE 4 shows Bragg curves (charge generation vs. particle penetration length) of Si, Al, Mg, Na, F, C, and He, which were obtained by the data conversion of Linear Energy Transfer (LET) versus depth using SRIM-96 [9]. The integrated area over the path length for each curve is the total charge generated by the respective ion. The Bragg curves in FIGURE 4 show that ions (except He) have similar energy loss curves in the first several microns, and each ion (except He) can induce hundreds of fC of charge within a few microns to upset almost any modern circuit.

In the present work, specially designed test structures were experimentally studied, using microbeams produced by the accelerator at the Ion Beam Materials and Research Laboratory (IBMRL) at Sandia National Laboratories (SNL). As shown in FIGURE 4, carbon ions (10 MeV and 12 MeV) have a relative constant induced charge (~50 fC/μm) along their range, which can simplify data interpretation and modeling. Also, carbon ions can be easily obtained and are able to penetrate the protective oxide

layers on ICs. Other ions can also be easily substituted. Similar test structures have been studied using a moderate resolution (~2 μm) pin-hole external beam system with alpha and fluorine ions at the University of North Texas (UNT) [59-61]. A 28 MeV silicon microbeam has also been used to study charge collection dynamics from stripe-like test junctions.

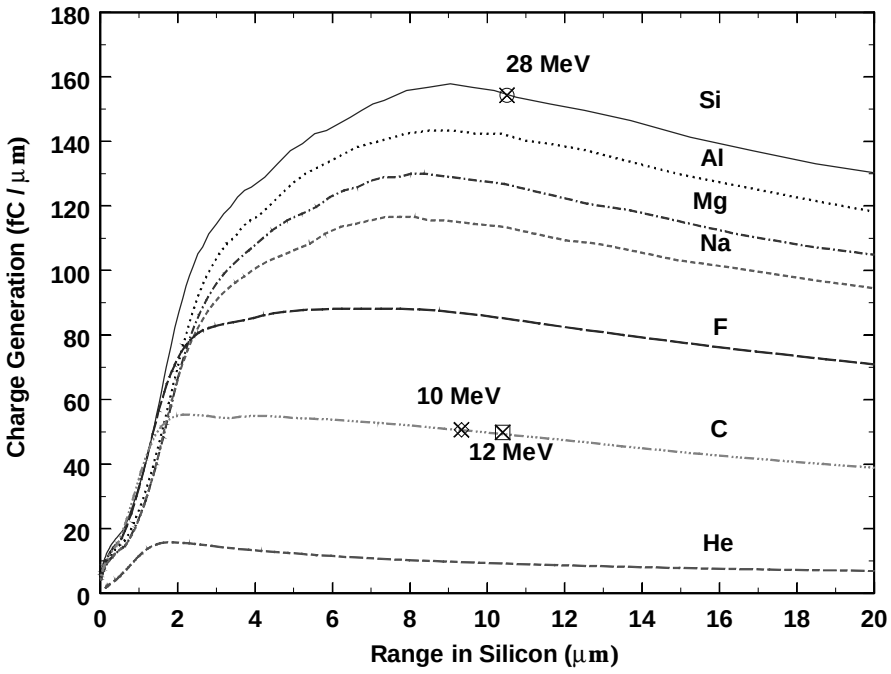

FIGURE 4. Bragg curves of Si, Al, Mg, Na, F, C, and He from the data conversion of Linear Energy Transfer (LET) versus depth obtained using SRIM-96 [9]. Carbon (10 MeV and 12 MeV) and silicon (28 MeV) microbeams were used to experimentally study the charge collection dynamics on IC test structures. Microbeams were produced by the accelerator at the Ion Beam Materials and Research Laboratory (IBMRL) at Sandia National Laboratories (SNL).

In Chapter 2, carrier transport based on the drift-diffusion model and a 2D device simulation tool, the MEDICI code, are discussed. In Chapter 3, the IBICC experimental results on test structures (ring-gate-inner and large diode) are presented. With the aid of IC layout information, an analysis of the charge collection efficiency from different test areas is given. In Chapter 4, the idea of Diffusion Time Resolved IBICC (DTRIBICC) is first proposed in this dissertation research to estimate the time duration of diffused charge collection. The use of the DTRIBICC technique to measure the relative average arrival time between stripe-like junctions is described. Also, MEDICI simulation results are compared with the experimental data. In Chapter 5, conclusions are drawn. In Appendix A, an overview of the microbeam systems based on the apertured microbeam and focused heavy ion microprobe facility at the University of North Texas is presented. Preliminary results are presented, using the focused heavy ion microprobe system. In Appendix B, MEDICI codes are given and some results are discussed.

CHAPTER 2

THEORY FOR CHARGE COLLECTION DYNAMICS

Structures of Integrated Circuits

Modern Integrated Circuits (ICs) are typically formed using planar technology at the semiconductor substrate with a patterned array of different kinds of components, such as diodes, transistors, resistors, capacitors, etc. Above the semiconductor surface, there are usually thin patterned layers of insulating materials and metal tracks that make up the interconnecting device layers, with a thick passivation layer over the device surface. The total thickness of all the surface layers present can be several microns. On the same semiconductor wafer, *pn* junctions are usually formed by selectively doping different regions using processes such as ion implantation and impurity diffusion. The behavior of the doped impurity atoms (acceptors for *p*-type such as boron, and donors for *n*-type such as arensic) in the semiconductor determines the fundamental electronic characteristics that underlie the functions of an IC [97-100].

Because of the concentration gradients of charge carriers around the regions with contrasting doping characteristics in the semiconductor, the diffusion of electrons and holes will result in the formation of the depletion regions. Also, an electric field is formed with a maximum strength at the junction that extends into the material on each side.

FIGURE 5 shows an abrupt *pn* junction in thermal equilibrium, which is formed by an abrupt impurity concentration transition from acceptor impurities N_A to donor impurities N_D in a semiconductor (FIGURE 5-A) [97]. N_A and N_D are the doping concentrations (atoms/cm^3) in the *p*-type and *n*-type materials, respectively. At thermal equilibrium, the shaded area corresponds to the built-in potential, V_{bi}, across the junction as shown in FIGURE 5-B. The thickness of the depletion region of the junction [97] is

$$W = \sqrt{\frac{2\varepsilon_s}{q}(V_{bi} + V_e)\left[\frac{N_A + N_D}{N_A N_D}\right]} \quad , \tag{1}$$

where ε_s is the dielectric constant and q is elementary charge, and the *n*-type material is at a higher positive potential than the *p*-type material in the depletion region. V_e is an externally applied bias voltage that is defined as being positive for the reverse bias.

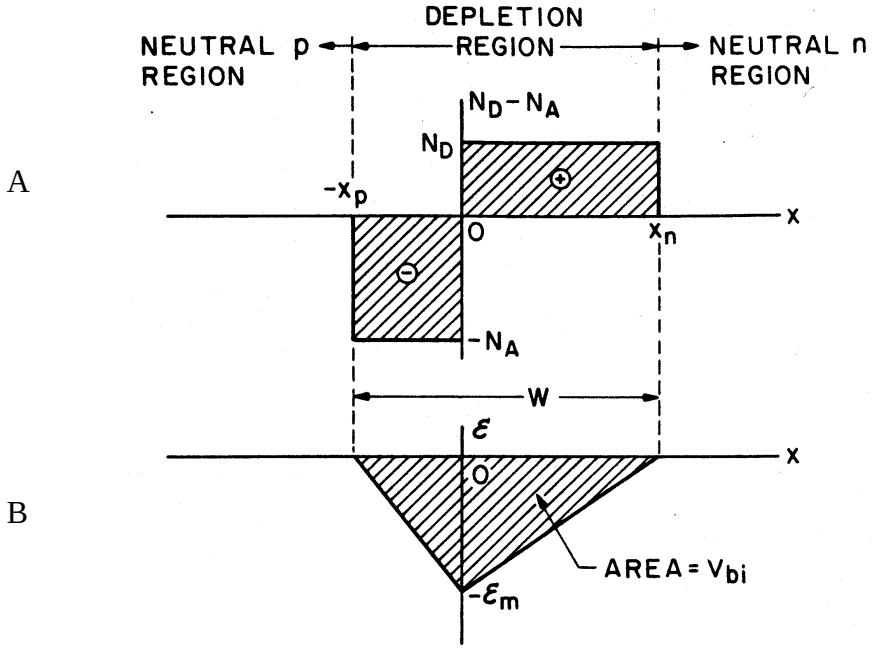

FIGURE 5. An abrupt pn junction in thermal equilibrium. (A) space charge distribution, and (B) electric field distribution. The shaded area in (B) corresponds to the built-in potential V_{bi} [97].

Charge Transport in Semiconductor Devices

The charge carrier transport in semiconductor materials can be described, using a drift-diffusion model [101]. The basic equations for the drift-diffusion model are

$$\nabla^2 \varphi = \frac{\rho}{\varepsilon_s} \tag{2}$$

$$\nabla \cdot \vec{J}_n = q(r - g - \frac{\partial n}{\partial t}) \tag{3}$$

$$\nabla \cdot \vec{J}_p = q(-r + g - \frac{\partial p}{\partial t}) \tag{4}$$

$$\vec{J}_n = \vec{J}_{n,drift} + \vec{J}_{n,diffusion} = q\mu_n n\vec{E} + qD_n \nabla n = -q\mu_n \, n\nabla\varphi + qD_n \nabla n \tag{5}$$

$$\vec{J}_p = \vec{J}_{p,drift} + \vec{J}_{p,diffusion} = q\mu_p \, p\vec{E} - qD_p \nabla p = -q\mu_p \; p\nabla\varphi - qD_p \nabla p \tag{6}$$

$$D_n = (\frac{kT_0}{q})\mu_n \tag{7}$$

$$D_p = (\frac{kT_0}{q})\mu_p \, . \tag{8}$$

In the equations (2-8), φ is the scalar potential, ρ is the net charge density, ε_s is the dielectric constant, r and g are carrier recombination and generation rates, n and p are the electron and hole densities, μ_n and μ_p are the electron and hole mobilities (in $cm^2/V/s$). D_n and D_p are the electron and hole diffusion coefficients (in cm^2/s), k is Boltzmann's constant. T_0 is the lattice temperature (in absolute temperature K).

In the drift-diffusion model, the semiconductor device equations are derived from the Boltzmann transport equations, using numerous approximations [101]. Equation 2 is

the Poisson equation. The continuity equations 3 and 4 are for the electron and holes, respectively. The constitutive relation equations 5 and 6, including a diffusion component and a drift component, give the electron and hole current densities, $\vec{J}_n$ and $\vec{J}_p$, respectively. Equations 7 and 8 are Einstein relations that link carrier mobilities and diffusion coefficients [97].

Device Simulation Methodology

Technology Computer Aided Design (TCAD) tools, including circuit, device and process simulation, has been widely used at all levels of IC design and manufacturing. The following discussion is concentrated on the device simulation issues related to the induced charge collection dynamics studies in semiconductor devices.

The drift-diffusion model, described by the set equations 2-8, is one of most commonly adopted models in device simulation. These equations (Poisson equation, current continuity equations, and constitutive equations) can be made discrete and solved using finite-element techniques. The next level in the device simulation hierarchy uses hydrodynamic and energy balance codes. The hydrodynamic model treats non-local effects, such as local carrier heating in high and spatially rapidly varying electric fields, using energy balance equations. The most complicated device simulations use Monte Carlo methods. Instead of using complicated macroscopic equations, Monte Carlo methods describe carrier transport on a fundamental, microscopic scale using the classical equations of motion. The motion of individual carriers is followed using classical physics

as they drift in fields and scatter from scattering centers until statistical significance is achieved [92,102-104]. Comparing the computational intensities of device simulation tools based on the above three modeling methodologies, the drift-diffusion model is the most efficient and remains the workhorse of device simulation.

To solve the Partial Differential Equations (PDEs) of the drift-diffusion model on a computer, the PDEs must be discretized on a simulation grid (or mesh). The continuous functions of the PDEs are represented by vector of function values at the nodes, and suitable difference operators replace the differential operators. The resulting set of algebraic equations is coupled and nonlinear. The total number of equations in each system is on the order of 1-4 times the number of the grid points. This nonlinear system can be solved by a nonlinear iteration method, and the total cost of a simulation is the product of the number of matrix solutions and the cost of each solution.

The specification of boundary conditions is one of the most important aspects to solving the PDE system [105]. In the device simulations, boundary conditions are difficult to accurately specify. Physically, the underly processes around the boundaries are less well known than the behavior in other regions. Numerically, simulation may fail to converge with boundary conditions that are believed to be appropriate. The three types of boundary conditions to the PDEs are commonly referred to as Dirichlet, Neumann, and Cauchy conditions. 1) Dirichlet boundary conditions specify the quantity of interest on the boundary, such as the potential or the density at a boundary. 2) Neumann boundary conditions specify the normal derivative of the quantity at the boundary, such as the flux through a boundary. 3) Cauchy boundary conditions specify the quantity and its derivative along part of the boundary. In semiconductor devices, the boundaries are likely

to be either Ohmic contacts or semiconductor-insulating interfaces. At the Ohmic contacts, it is generally assumed that the carrier densities are equal to their equilibrium values and the semiconductor is neutral. On insulating surfaces, the flux will be determined by the surface recombination velocity (or rate). If charge is not building up on the surface, then the electron and hole fluxes must be the same and equal to the surface recombination rate. If the surface recombination rate is infinite, such as at a conducting boundary, the carrier densities will take their equilibrium values. At the insulator, however, it is more common to assume the reflective boundary with zero surface recombination rates. In reality, the surface recombination rate should be some value between 0 and infinite [105].

Since the drift-diffusion charge transport is influenced by the potential and carrier concentration gradients, the simulation requires 3D tools to deal with reality. Still, due to simplified computing efficiency for 1D or 2D simulations, the latter can provide insight into how the induced charge is transported within devices. A wide variety of computer simulation tools based on drift-diffusion models are commercially available to simulate the effects of particles striking ICs. For example, Avant! Corporation provides simulation software packages, DAVINCI for 3D, and MEDICI for 2D device simulations [96], which include effects such as Schockley-Read-Hall (SRH) and Auger recombination, carrier mobility (affected by concentration, field, and carrier-carrier scattering), etc.

Both DAVINCI and MEDICI can be used to study steady state or time dependent injection of electrons and holes. A localized electron-hole pair generation term, which is incorporated into the continuity equations to simulate the induced charge in the devices, has the following form:

$$G_n(l,r,t) = G_p(l,r,t) = L(l) \cdot R(r) \cdot T(t). \quad (9)$$

The length dependent term is defined as

$$L(l) = A1 + A2 \cdot l + A3 \cdot e^{A4 \cdot l} + k \cdot \left[C1 \cdot (C2 + C3 \cdot l)^4 + L_f(l) \right]. \quad (10)$$

Parameters A1, A2, A3, and A4 can be used to describe the length dependence of the generation rate. Parameters C1, C2, C3 and C4 can be used to define the Linear Energy Transfer (LET) for the SEU simulation. The term L_f represents a table of LET values as a function of track length. In this work, a table of LET in pC/μm is read from a formatted file based on calculations with SRIM96 to represent the length dependence of the generation along the incident ion track.

The radial term is defined as

$$R(r) = \begin{cases} e^{-(r/DCHR)^2} & if\ DCHR > 0 \\ 1 & if\ DCHR = 0 \end{cases}, \quad (11)$$

where DCHR is the radial characteristic length. DCHR=0.2 μm was chosen to represent the initial induced electron-hole plasma along the ion track in the present work. The time-dependent term may be chosen as one of the four forms, Gaussian, Delta, Uniform, or Pulse. In this work, the Gaussian generation form is chosen and defined as

$$T(t) = \frac{2 \cdot e^{\left[-(t-T_0/T_C)^2\right]}}{T_c \cdot \sqrt{\pi} \cdot erfc(-T_0 / T_c)}, \quad (12)$$

where T_0 is the time of the peak of the Gaussian pulse and T_c is the characteristic time of the generation pulse. In this work, T_c=1.5x10^{-12} s and T_0=3.0x10^{-12} s were chosen to simulate the induced charge along the ion track.

Both DAVINCI and MEDICI incorporate several advanced application modules. One such module is the Circuit Analysis (CA) module. With the CA module, MEDICI can simulate device response in mix-mode, including both physical device and circuit models at the same time. The mixed mode simulations have been widely used to study the responses of devices loaded with extra circuit elements during ion strikes and generated a lot of insight into the responses of devices [106-110].

The following discussions and later simulation results are based on the available 2D simulation tool, MEDICI [111]. MEDICI has the same physical fundamentals as its counterpart 3D simulation tool, DAVINICI. Since the charge column generated as the ion passes through the device shows cylindrical symmetry, 2D MEDICI can not simultaneously represent the charge column and the geometry of the problem. It is expected that the 2D MEDICI numerical simulation results will be slightly different from the numerical results based on the 3D code. However, the problem can be simplified by assuming that the ion enters the semiconductor at normal incidence. This places the charge column along the z-axis of a cylindrical coordinate system and the full 3D accuracy can be obtained by only simulating the radial (r) and depth (z) dependence. Otherwise, a full 3D-simulation tool (such as DAVINCI) is needed to better represent the geometry as well as the charge column.

FIGURE 6 illustrate the effects of simulating an ion track in 2D, quasi-3D, and 3D [92]. In a 2D simulation, all quantities are extended into the third dimension. Therefore, only the correct induced charge density or the correct total induced charge can be simulated. It is impossible to describe the ion track correctly in 2D (FIGURE 6-A). As shown in FIGURE 6-B, if devices exhibit circular symmetry, then cylindrical ion track

can be simulated in quasi-3D (radial r and depth z). However, for less ideal circular symmetric devices, the geometrical approximations have to be used. To describe the ion track (induced charge density and total induced charge) and device geometry correctly, the 3D simulator should be used and truly predictive results can be obtained (FIGURE 6-C).

Since the 2D MEDICI code is much less computationally intensive than the 3D simulation code, it is still widely used to understand the underlying physics of device performance. As a device simulation tool, MEDICI can predicts the electrical characterization of arbitrary 2D structures under specified operating conditions. Also, it can predict internal device operation through potential, field, carrier, carrier temperature, ionization rate, and current density distributions.

FIGURE 6-A

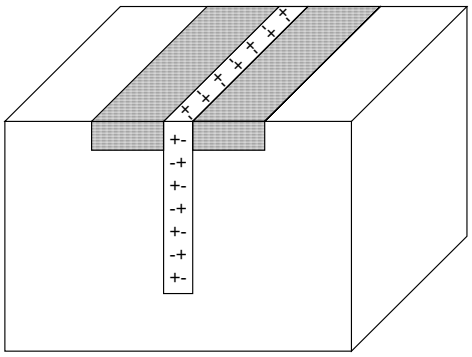

FIGURE 6-B

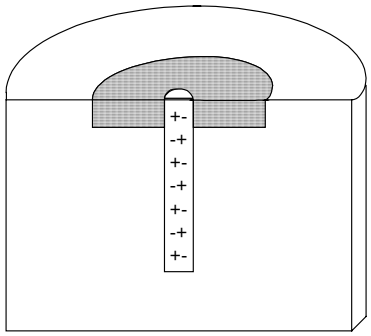

FIGURE 6-B

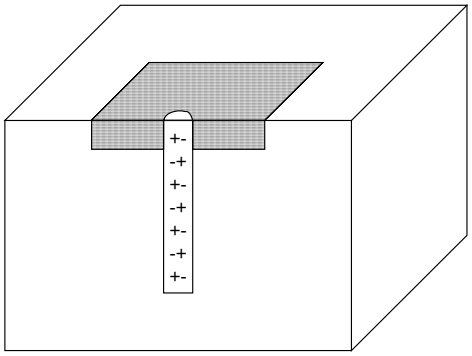

FIGURE 6. Ion track descriptions in 2D, quasi-3D, and 3D. A simulates ion track in 2D, all quantities are extended into the third dimension. B simulates ion track if devices exhibit circular symmetry in quasi-3D (radial r and depth z). C simulates ion track and device geometry in 3D. Simulations in 3D are much more computationally intensive than that in 2D and quasi-3D [92].

Physical Parameters

The physical models adopted by the device simulation can be tracked through the semiconductor parameters [105]. MEDICI incorporates a number of analytical, empirical functions to account for the semiconductor parameter dependence on doping concentration, electric field, temperature, and etc.

Permittivity In general, permittivity ε is a tensor and may be time dependent and a function of the applied field. Since silicon based semiconductor devices are isotropic and nonmagnetic, ε is often regarded as a constant. But it should be acknowledged that this assumption may not be suitable to represent the physical picture when ion induced charge transients are too fast relative to the dielectric relaxation time. Therefore, the quasi-static Poisson equation may have some limitations when it is used to describe transient phenomena due to the inclusion of the well-defined low-frequency permittivity [8]. The relative permittivities of Si, SiO_2, and Si_3N_4 are 11.8, 3.9, and 7.2, respectively. The absolute permittivities of the materials are equal to the relative permittivities multiplied by the permittivity of free space, which is equal to 8.854×10^{-14} F/cm.

Carrier mobilities Low field values of the mobility for silicon at 300 K are 1450 $cm^2/V/s$ for electrons and 450 $cm^2/V/s$ for holes. The carrier mobilities can be affected by many mechanisms such as scattering by thermal lattice vibrations, ionized impurities, neutral impurities, vacancies, interstitials, dislocations, surfaces, and by electrons and holes themselves. The net effect is reduced mobilities. Further reduction in mobilities is

possible due to the saturation of the drift velocity. Depending on the electric field, MEDICI includes low field mobility models and high field dependent (transverse and parallel field) models. Detailed discussions of these mobility models are given in the MEDICI manual [111]. In this work, the CCSMOB semi-empirical mobility model is chosen to account for the carrier-carrier scattering (CCS) effects due to the high concentration of induced electron-hole pairs, the effects of lattice scattering and ionization impurity scattering, and the effects of doping and temperature on mobility.

Diffusion coefficients For non-degenerately doped semiconductors where Boltzmann statistics are applicable, the Einstein relationship bridges the carrier mobilities and diffusion coefficients. The Einstein relations are derived from the assumption that the doping density is light enough so that the Boltzmann statistics still apply. There are some uncertainties about whether Einstein relations still apply for highly concentrated induced electron-hole pairs along the ion track. A theoretical analysis predicts that the Einstein relations should be modified so that CCS does not affect the ambipolar diffusion coefficients due to the formation of electron-hole plasma along the ion track, even though mobilities are affected [112]. However, experimental investigation indicates a contradiction that CCS does affect the ambipolar diffusion coefficients, and the Einstein relations still apply [113]. MEDICI assumes that the Einstein relations are still valid even with the existence of transient high concentrations of electron-hole pairs along the ion track.

Carrier Recombination and Generation (R-G) The dominated carrier R-G mechanisms are photon transitions, phonon transitions, three particle (Auger) transitions, and impact ionization. 1) Photogeneration occurs when sufficiently energetic photons are

absorbed, which lead to the creation of electron-hole pairs. This is the basic mechanism to create electron-hole pairs along a laser path and therefore to simulate a highly dense plasma in the device to study the charge collection dynamics. The opposite process, radiative recombination, occurs when a conduction-band electron falls back to the valence-band and releases its energy in the form of light. 2) Phonon transitions are primarily two step processes and occur at traps located between the conduction-band and valence-band. One step phonon transition is unlikely to occur in silicon, an indirect band gap semiconductor. The conservation of energy and crystal momentum prohibits carrier recombination from occurring directly between the conduction band and the valence band without a simultaneous lattice interaction. Therefore, the dominant recombination process is indirect transition via localized energy states or defect energy states in the silicon band gap [97]. MEDICI incorporates phonon R-G based on SRH theory [114,115], and has the choices between constant carrier lifetime and CONcentration dependent SRH carrier lifetime (CONSRH). 3) Three particle Auger recombination (AUGER) is included to account for Auger recombination when the carrier concentrations become very large as in the cases of high level current injection in power devices, or highly concentrated electron-hole pairs along the ion track.

Minority carrier lifetimes To preserve the charge neutrality in semiconductor materials, the motion of the excess minority carriers determines the motion of the excess majority carriers. Excess majority carriers follow the motion of the induced minority carriers. If a minority carrier is trapped at a defect, a majority carrier might also make the transition to the defect level, depending on the nature of the defect, leading to the occurrence of electron-hole recombination. Physically, the minority carrier lifetime τ_n or

τ_p is interpreted as the average time that an excess minority carrier will live in a sea of majority carriers. Mathematically, τ_n and τ_p are defined as the reciprocals of the electron and hole capture rates. MEDICI adopts the concentration dependent lifetimes as well as lattice temperature dependent lifetimes. The average lifetime of minority carriers [97] is

$$\tau = \frac{1}{N_d \, \sigma_d \, v_{th}}, \tag{13}$$

where N_d is the defect density (cm^{-3}), σ_d is the trapping cross-section (10^{-13} to 10^{-17} cm^2) of initial defects present, and v_{th} is the carrier thermal velocity (~10^7 cm/s). Experimental results suggest that the carrier lifetimes should be functions of the doping concentration. Also, the carrier lifetimes can be influenced by various process procedures, such as gettering, gold doping etc. Values of the minority carrier lifetimes can range from ms for very pure silicon to ns for heavily doped materials or those with a high defect density. For example, for a material with a defect density of 10^{15} cm^{-3} and a typical defect trap cross-section of 10^{-15} cm^2, the equation (13) gives τ ~ 100 ns [116]. Also the minority carrier diffusion length L can be expressed as

$$L = \sqrt{D\tau} = \sqrt{\frac{D}{N_d \, \sigma_d \, v_{th}}}. \tag{14}$$

Degeneracy and band gap narrowing Boltzmann statistics do not apply to the degenerately doped devices, such as power devices. One approach to deal with a degenerately doped semiconductor is to use Fermi-Dirac statistics and introduce degeneracy factors into the semiconductor equations. And alternative approach is to assume that the semiconductor's band gap narrows as the dopant concentration increases. The second approach can be argued as follows. At low concentrations, the dopant atoms

only introduce a single allowable impurity energy level in the band gap with negligible dopant-dopant interactions. At high dopant concentrations, the interactions among dopant atoms lead to a continuum of energies in the band-gap rather than a single allowable energy level. These energies merge into the valence band in the case of acceptors or the conduction band in the case of donors. The net effect is Band Gap Narrowing (BGN). In the following sections, the MEDICI simulation uses Boltzmann statistics and BGN.

Charge Collection Dynamics in Semiconductor Devices

Ionizing radiation can create numerous electron-hole pairs in semiconductor materials. The average energy, E_{eh}, needed to create the electron-hole pairs is material dependent and typically about three times the energy band gap E_g. For silicon, E_{eh} is 3.6 eV, and E_g is 1.1 eV. If a heavy ion passes through the depletion region of a *pn* junction, electron-hole pairs form an ion track. Immediately after the ion hits, the electronic energy loss will induce a high-energy, electron-hole plasma, which decays into a cylindrical column of electron-hole pairs after thermalization within a time period of the order of picoseconds. Electron-hole pairs form an ion track with a radius of about 0.1 μm for alpha particles [4]. In order to characterize the charge collection dynamics, it is important to know the ion track structure [117,118]. Some stripe-like test structures have been used to experimentally measure the ion induced carrier intensity [119-121].

If the semiconductor contains no electric field, the induced charge carriers diffuse randomly through the semiconductor lattice, the become trapped, and recombine. If the

semiconductor contains an electric field like that near a *pn* junction, the charge carriers are separated in the field region and the net charge flow can be measured in an external circuit. Ion induced charge carriers created in the depletion region are separated under the influence of the electric field, and move with a drift velocity $v_d = \mu E$, where μ is the carrier mobility and E is the electric field strength. For a 1 μm thick depletion layer with 1 V across it, and a mobility of μ=1450 cm^2/V/s, carriers take about 10 ps to cross the depletion layer. Compared with the ns or longer carrier lifetimes in doped semiconductors, charge carriers have a low probability of being trapped at any defect present in the depletion layer. It is therefore generally assumed that 100% charge collection in the depletion layer occurs unless the transient charge collection is considered.

Low injection carrier conditions

If the induced charge does not exceed the doping level in the semiconductor, and the electric field perturbation by the excess carrier is not strong enough to distort the junction depletion region, then the low injection carrier condition is satisfied. It is assumed that carriers generated in the depletion region and those that diffuse to its edges are all collected independent of the electric field strength. The collected charge Q along the ionization track can be calculated by integrating the electronic energy loss dE/dz between the semiconductor surface z=0 and the ion range $z=R_i$.

For the short-range ions stopped in the depletion region, all energy is deposited within the depletion region, generating the electron-hole pairs. The total collected charge Q can be obtained by converting the total energy loss into the amount of charge. For the

long-range ions, electron-hole pairs are generated not only in the depletion layer but also in the silicon bulk. It is assumed that an incident ion at normal angle of incidence penetrates a depletion layer, and the lateral size of the depletion layer is much larger than the ion range and the diffusion length. The 3D carrier generation volume can be simplified by a one-dimensional depth distribution. The total collected charge Q is given by [122]

$$Q = \int_0^{z_d} \frac{dE}{dz} \frac{q\,dz}{E_{eh}} + \int_{z_d}^{R_i} \frac{dE}{dz} e^{-(z-z_d)/L} \frac{q\,dz}{E_{eh}} \quad , \tag{15}$$

where L is the diffusion length (μm) in the sample, and dE/dz is the electronic stopping power in eV/μm. The first term is the induced charge within the depletion region with thickness z_d μm. The second term is the diffusive component to the depletion region for the induced charge in the substrate. If an actual IC device is considered, the passivation layer (silicon oxide or silicon nitride with thickness z_p μm) must be taken into account and the lower limit of integration for the first term starts at the z_p. If the incident ion is at an angle to the surface plane, the increased ion track must be taken into account and the integration limits should also change correspondingly.

High injection carrier conditions

Along a heavy ion track in the semiconductor, the induced carrier density can reach up to $10^{20}/cm^3$, which is much greater than the typical device substrate doping density. This dense plasma formation can thus distort the shape of the electric field around the depletion region of the *pn* junction, giving rise to funneling assisted charge collection [4-8].

The following description about funneling assisted charge collection is for an *n+/p* junction and is supported by simulation [8,123]. The statements should apply for a *p+/n* junction with corresponding modifications. The external reverse bias is applied to the junction by an external circuit.

Immediately after ion track formation, the two stages, the collapse of depletion region (DR) and the recovery of DR, can be described as follows (FIGURE 7). Because of the reverse electric field (external and built-in) inside the DR, a rearrangement of charge carriers (electrons move up and holes move down) occurs. The neutralization of the previously uncompensated ionized donors and acceptors results in the DR shrinking and the DR Boundary (DRB) moving up. The DRB is defined when there are two distinct regions consisting of the DR and a quasi-neutral region in the substrate. Even in the presence of ion tracks, simulations have shown the existence of the quasi-neutral region, which is defined as the region where the charge imbalance is small compared to the majority carrier density [8]. Since the electric field in the DR is much stronger than anywhere else, the primary significance of this fast DR collapse is to establish the initial conditions for what follows. As the electric field continues to force holes downward, they move below the previously screened negative acceptor ions. When the DR reaches the minimum size, the DR collapse is over and the DR recovery begins. Since the duration of the DR collapse is very short (picoseconds), very little charge will be collected even though the funneling has already started. Because of the DR collapse, the potential held previously by the DR is reduced. This implies that some or nearly all (depending on external circuit impedance) of the DR potential loss is balanced across the substrate. The

substrate potential drop enhances the minority carrier (electron) flow from the substrate to the DR. This enhanced flow is known as funneling.

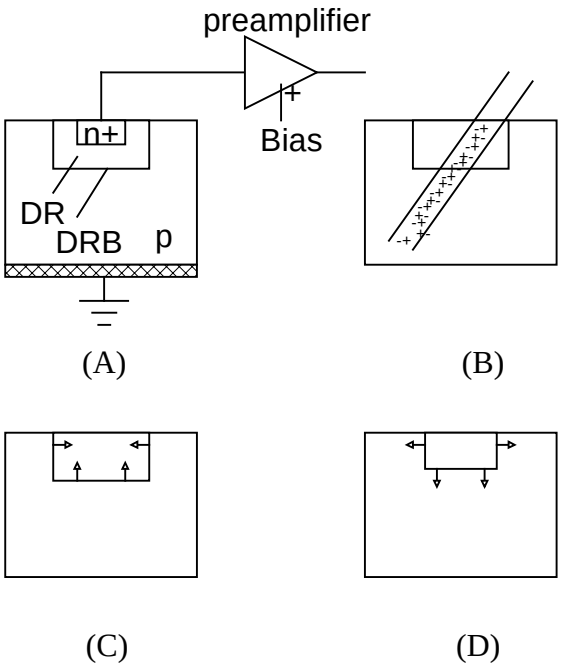

FIGURE 7. Funneling assistant charge collection [123]. (A) An n+/p junction before the ion hit. The preamplifier is used to collect the charge, and the junction is reverse biased through the preamplifier. (B) after the ion hit and before the charge separation occurs, (C) the Depletion Region (DR) collapse caused by the carrier rearrangement, and (D) the DR is recovering. Most of the charge is collected during the DR recovery. Arrows show the DR Boundary (DRB) motion.

During the DR recovery, there is essentially no hole replacement from the *n*+ region due to recombination in the *n*+ region as holes are pushed down. For the electrons, they are moving up and out of the DR and are replaced by the electrons in the lightly doped *p* substrate. Therefore, during the DR recovery, there is a high electron density with virtually no holes inside of the DR. The duration of the DR recovery depends on the external circuit, substrate, and ion track characteristics. The DR recovery can range from tens of picoseconds to nanoseconds.

The currents pass through a stationary surface *SS*, which is the same as the pre-ion-hit DRB. The drift and diffusion currents can be described using equations 5 and 6. In the substrate, the induced electrons and holes are generated in pairs and the density is much higher than the intrinsic level. Combined with the Einstein relation (equations 7 and 8), the following equations can be applied to the substrate

$$\vec{J}_n = \frac{\mu_n}{\mu_p}\vec{J}_{p,drift} - \frac{\mu_n}{\mu_p}\vec{J}_{p,diffusion} = \frac{\mu_n}{\mu_p}\vec{J}_p - 2\frac{\mu_n}{\mu_p}\vec{J}_{p,diffusion} = \frac{\mu_n}{\mu_p}\vec{J}_p + 2\vec{J}_{n,diffusion} \quad (16)$$

$$\vec{J}_T = \vec{J}_p + \vec{J}_n = (1+\frac{\mu_n}{\mu_p})\vec{J}_p + 2\vec{J}_{n,diffusion} \quad (17)$$

Integrating over the surface *SS* with downward normal direction, the total current is

$$I_T = I_p + I_n = (1+\frac{\mu_n}{\mu_p})I_p + 2I_{n,diffusion} \quad (18)$$

As discussed above, the depletion of holes in the DR implies that the time integrated flow of holes across *SS* equals the total number of holes initially induced in the DR by the ion. Let t_r represents the DR recovery time, which is large enough so that almost all the holes are pushed out and through the *SS*. Integrating the hole current over the recovery time gives

$$Q_T(t) = (1+\frac{\mu_n}{\mu_p})Q_D + 2Q_{n,diff}(t) = (1+\frac{\mu_n}{\mu_p})\cdot W\cdot q\alpha + 2Q_{n,diff}(t), \qquad t > t_r \quad (19)$$

where $Q_T(t)$ is the total charge collected at time t, Q_D is the charge induced by the ion in the pre-ion-hit DR, $Q_{n,diff}(t)$ is the time integral of the electron diffusion current, $q\alpha$ is the induced charge density per unit length, W is the thickness of depletion region, and $(1+\mu_n/\mu_p)W$ is the funneling length [124].

Based on the drift and diffusion equations and accounting for the drift and diffusion currents of majority and minority carriers, a modified form of Ohm's law has been derived to describe the electric currents through ion tracks [8]. Assuming that the ratio of the majority carrier to minority carrier mobility is spatially uniform through the quasi-neutral region, the modified Ohm's law [8] can be stated as

$$\vec{J}_T = -\sigma \nabla \psi \tag{20}$$

$$\sigma \equiv q(\mu_p (P + p_0) + \mu_n (P + n_0)) \tag{21}$$

$$\psi = \phi - B(\frac{kT_0}{q}) \ln(\frac{P + A}{A}) \tag{22}$$

$$A \equiv \frac{\mu_n n_0 + \mu_p p_0}{\mu_n + \mu_p} \approx \begin{cases} \frac{\mu_p}{\mu_n + \mu_p} \times [\textit{doping density}] & \textit{for } p-\textit{type region} \\ \frac{\mu_n}{\mu_n + \mu_p} \times [\textit{doping density}] & \textit{for } n-\textit{type region} \end{cases} \tag{23}$$

$$B \equiv \frac{\mu_n - \mu_p}{\mu_n + \mu_p} \tag{24}$$

where ψ is the modified potential instead of the true electrostatic potential φ in the classical forms of Ohm's law, σ is the conductivity, and P is the induced electron and hole pair density. Also n_0 and p_0 are the equilibrium electron and hole densities, respectively.

During the DR recovery, funneling is occurring as some voltage is dropped across the substrate. With a known substrate potential drop, the current calculation can be converted using Ohm's law into calculation of the substrate 3D spreading resistance (including the ion track). The conductivity function can be divided two regions, a high

conductivity region along the track and a low conductivity region below the track. The track conductivity is large near the central line of the track and becomes smaller radially far away from the central line. The electric field in the upper track region is weakest near the central track and stronger at longer radial distances. This means that the central equipotential surfaces form the funnel shape.

Experimental studies concerning the size of the funneling region as a function of doping, junction bias, and the angle between the particle track and the junction depletion edge have been conducted [4-7]. An analytical model has also been described to calculate the effective length of the charge funnel and the additional charge collected by the struck junction due to the charge funneling [7,125,126]. Serious doubts [127] have been raised about the validity of the model, which uses the assumption that the time-average electric field is confined to a depth equal to the funneling charge collection depth. The model also does not recognize that the partially recovered DR holds the device voltage across the relative narrower depletion region. Therefore, the model overestimates the time-average electric field strength in the substrate, which is partially compensated by using field dependent mobility and ignorance of the diffusive charge collection [127].

Ion Induced Damage Effects

Ion induced damage to the semiconductor lattice structure may occur along the ion track, the main mechanism being the creation of vacancy/interstitial pairs (Frenkel

defects) [99]. The primary effect of these defects in semiconductors is a reduction in the minority carrier diffusion length through carrier recombination and trapping processes. A non-uniform spatial distribution of recombination centers in the semiconductor substrate will result in a non-uniform diffusion length function. Therefore, the substrate diffusion length may influence charge collected by diffusion from ion tracks in the substrate. A theoretical analysis shows that charge collection is not sensitive to the spatial variations in the diffusion length function, so it is possible to define an effective diffusion length as a uniform diffusion length [128].

MEDICI provides a method to modify the reduced Schockley-Read-Hall (SRH) carrier lifetimes. For the electrons, the reduced lifetime along the ion track with SRH lifetime modifier is defined as

$$\frac{1}{\tau_n(x,y)} = \frac{1}{\tau_{n0}(x,y)} + RECO \cdot G_n(x,y) \qquad (25)$$

where τ_n is the reduced SRH lifetime, τ_{n0} is the original SRH lifetime, *RECO* is the radiation induced carrier lifetime reduction modifier, and $G_n(x,y)$ is the electron generation rate without time-dependence ($T(t)=1$). The reduced hole lifetime can be defined in a similar manner.

The reduction of charge collection can also be used to measure defects present in devices. It is assumed that a low ion irradiation dose is used, such that ion induced Frenkel defects do not change the doping concentration of the semiconductor substrate. Only the effects of single defects are considered, and the effects of defect clusters are ignored. Also, the effects of defect mobility, thermal annealing, or self-annealing on the collected charge are not taken into account. The initial defects are the defects present

before the creation of any ion induced defects. The ion induced defects can be characterized by a trap cross-section $\gamma\sigma_d$, where the factor γ is used to take into account the energy level dependence of the detrapping time and occupation statistics at a given temperature. It is assumed that the same type of defect created along the full ion range has the same γ factor. The effect of ion induced damage on the diffusion length can be expressed as [122]

$$L = \sqrt{\frac{D}{(N_d + N_{dd}\gamma)\sigma_d v_{th}}}, \tag{26}$$

where N_{dd} is the ion induced defect density. Measuring the change of the diffusion length is a simple approach to characterize the effects of ion induced damage. The collected charge reduction can be studied using equation 26 to account for the effects of the ion damage.

In another equivalent damage factor model [129], induced charge in the depletion region is assumed to be collected with 100% efficiency. Thus, the charge collection in the substrate is modified by the effect of damage on minority carrier lifetime. Therefore, the model can be expressed as

$$Q = Q_0\left[(1-F) + \left(\frac{F}{1+K\Phi F Q_0}\right)\right], \tag{27}$$

where Q_0 is the initial charge, F is the fraction of charge in the damage sensitive region, K is the damage factor, and Φ is the fluence. With a series of data points of ion doses and collected charge, it is possible to fit the data and obtain the initial charge Q_0.

CHAPTER 3

ION BEAM INDUCED CHARGE COLLECTION (IBICC) EXPERIMENTAL MEASUREMENTS ON IC TEST STRUCTURES

IBICC Experimental Configuration

The first Ion Beam Induced Charge Collection (IBICC) image was obtained from a region of ion induced damage in a *pn* junction with an ion microbeam [130]. The Single Event Upset (SEU) studies in Integrated Circuit (IC) memory devices also helped the development of IBICC as an imaging technique [84-89]. Depending on the experimental configuration, the IBICC technique can be categorized as frontal IBICC or lateral IBICC (FIGURE 8). The induced charge can be measured using standard charged particle detection electronics, except that the detector is the sample itself with 100% counting efficiency. To avoid the radiation damage effects to the samples and the saturation of data acquisition electronics, the IBICC technique requires a low beam current (<pA) [116].

Frontal IBICC configuration (FIGURE 8-A) has been widely used to image the distribution of deeply buried junctions in semiconductor devices [86-89] and to investigate ion induced damage effects on charge collection efficiency [131-137]. With known device geometry, IBICC can also be used to study charge collection dynamics

near junctions, such as the test structures with highly symmetric geometry used in the present work. For non-homogeneous samples, it is very difficult for frontal IBICC to resolve the effects due to the properties of carriers from the local electrical field. Lateral IBICC (FIGURE 8-B) was therefore introduced to investigate charge collection properties laterally in radiation detector materials (such as diamond like carbon film) [138-140]. Carrier transport properties such as bulk mobility and the lifetime of charge carriers as well as the electric field profiles have been quantitatively mapped. For lateral IBICC, the samples are cut and the cross section should be finely polished. Also, the two electrodes that are used to sandwich samples should be carefully matched to the exposed lateral surface to avoid fringing field effects.

The advantages of using the focused ion microbeam include high spatial resolution in buried layers as well as the choice of being sensitive or insensitive to topographical information by choosing different ion species and energies [141]. Ion induced damage is the main limitation for the IBICC, which also limits the maximum number of ions that can be used to form an IBICC image. In addition, IBICC images can be statistically noisy. With an event-by-event data acquisition system, different types of image contrast can be achieved.

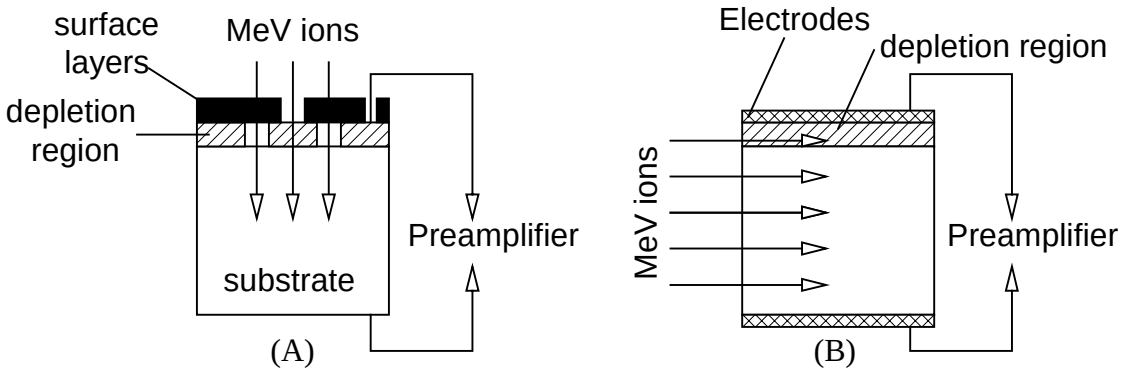

FIGURE 8. Ion Beam Induced Charge Collection (IBICC) experimental configuration, (A) frontal IBICC, and (B) lateral IBICC.

Experimental Details

Nuclear microprobe and data acquisition

The important components of a nuclear microprobe are the accelerator, the microprobe beamline, the focusing lens system, the sample chamber with detectors, the microbeam scanning system, and the data acquisition and analysis system [142]. In Appendix A, a detail description is given of the focused heavy ion microprobe facility at the University of North Texas (UNT). The UNT microprobe was not completely operational at the time the present work was conducted. Therefore, the measurements were made at Sandia National Laboratories (SNL).

The IBICC measurements, conducted at the Ion Beam Materials Research Laboratory (IBMRL) at SNL, employed a carbon ion microprobe with a 1 μm diameter beam spot size to scan test structures on specially designed ICs. A small magnetic quadrupole doublet lens manufactured by Dyer Energy Systems, and based on the design of Fred Martin, is used for focusing the SNL microprobe. This lens has a 3.38 mm bore, and each polepiece is 6 cm long. A unique feature of this lens is that the iron polepieces are electrically isolated, and the interior of the lens is vacuum tight, which allows the application of high voltages to each of the 8 individual poles, and to thereby scan the beam over the target [143,144].

Ion beam spots of 0.5 μm x 0.3 μm size at currents of a few thousand ions/second have been obtained using the SNL microprobe, and ion beams of 1 μm diameter are routine. The beam spot size is determined from STIM (Scanning Transmission Ion Microscopy) images of a 1000 mesh TEM grid (bar 9 μm wide, hole 16 μm on a side).

The TEM grid is adhered to the top of a pin diode (Hamamatsu Model S1223) using conducting silver paint. FIGURE 9 is a STIM 3D image. The 3D image (or datacube) was obtained using Sandia data acquisition system. The coordinate (X,Y) represent the beam striking position, and the Z direction is the charge collection by pin diode. The area of the beam scan is calibrated using the pitch of the grid in the STIM image or known feature sizes of scanning test structures. The STIM image can be used as the standard to calibrate data collection electronics. Also, the image can be used to locate the beam from a special feature image, such as the edge. Samples can be located on the same beam focal plane as the grid using a front viewing microscope.

FIGURE 10 shows an RBS measurement on a pin diode (Hamamatsu Model S1223) using a 1 MeV He^{+} beam with a detector at 150 degrees. The thickness of the silicon dioxide is about 1000 Å from curve fitting with the code RUMP [145]. Therefore, the energy loss (~25 keV) for the 10 MeV carbon beam through the silicon dioxide layer is ignored.

Charge was collected by junctions on the test structure under various conditions of junction back bias. The induced charge was measured using standard charged particle detection electronics, except that the detector was the IC itself. The collected charge was converted to charge pulse heights after passing through a charge-sensitive preamplifier (Ortec 142A) and an amplifier (Ortec590). The pulse heights were digitized by an Analog-to-Digital Converter (ADC) and recorded along with the scanning beam (X,Y) coordination in list mode by a computer for off-line analysis. In order to minimize ion induced damage effects on samples, the test structures were optically positioned using a front viewing microscope before being scanned by the beam [143].

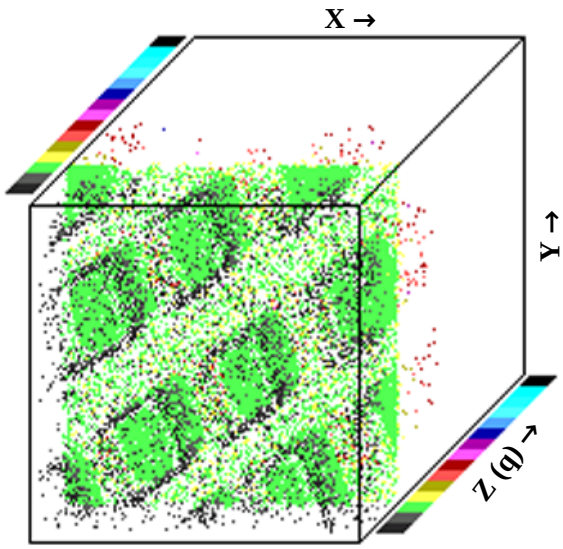

FIGURE 9. A Scanning Transmission Ion Microscopy (STIM) 3D image (in color) of a TEM grid (1000 mesh). The Z direction is charge collection by the pin diode. The special feature of the image, such as the edge, can be used to locate the beam. Samples can be located on the same beam focal plane as the grid using a front viewing microscope.

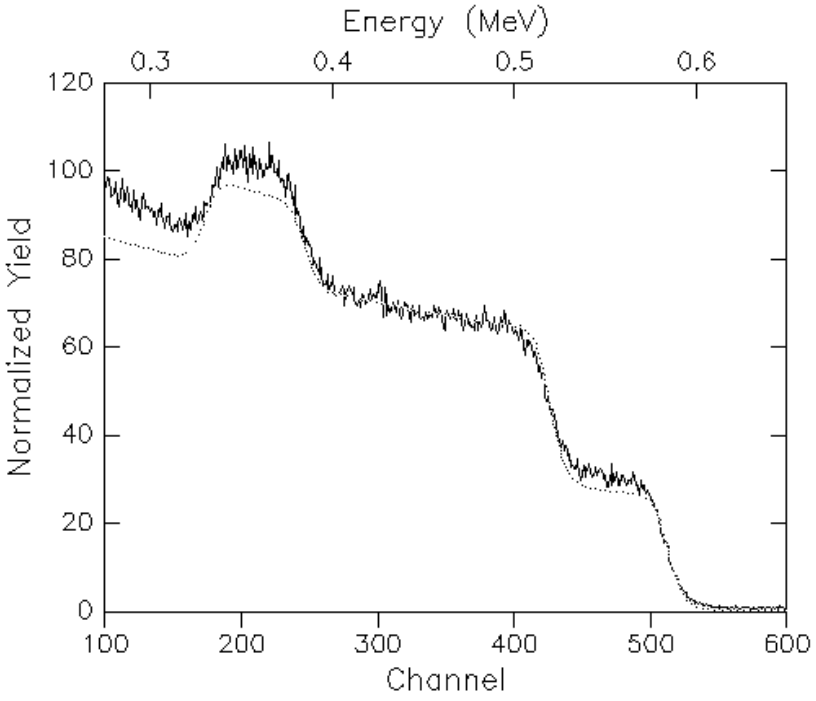

FIGURE 10. RBS measurement on a pin diode (Hamamatsu Model S1223) using 1 MeV He^+ beam with a detector at 150 degrees. The thickness of the silicon dioxide is about 1000 Å and was fitted (dotted line) with the code RUMP [145]. Therefore, the energy loss (~25 keV) for the 10 MeV carbon beam through the silicon dioxide layer is ignored.

IC test structures

The specially designed ICs contain various kinds of test structures. The ring-gate-inner diodes and large diode were used for the IBICC measurements. These diodes are formed from diffusions in a *p*-substrate. There is a window cover on the packaged IC, which can be removed to expose the IC to an optical microscope for examination or microbeam for measurements. Test structures are separately connected through different metal pads to outside package wiring to allow the operating voltages of test structures to be controlled independently. The charge collection outer ring and inner diodes are formed from the contact diffusions of an *n*-channel MOSFET (Metal-Oxide-Semiconductor Field Effect Transistor) in a *p*-substrate. The ring-gate-inner FET is one test node of a 6T-CMOS (Six Transistor Complementary-Metal-Oxide-Semiconductor) test structure, which is specifically designed to measure the charge collection from junctions typical of SRAMs and DRAMs (Static and Dynamic Random Access Memories) [59-61]. FIGURE 11 is the 6T-CMOS design layout (A), the equivalent circuit diagram (B) and charge collection node (C) with cross sectional view (D). The gate (G3) of the ring-gate-inner FET is a square ring, completely enclosing the inner diffusion diode. The ring diode is the ring-shaped diffusions surrounding the gate. The diode voltages can be continuously monitored by Source Follower (SF) transistors. The gate width was chosen to be the approximate node-to-node spacing of memories instead of typical of the pass gate width of DRAMs. The measured FET test structure has a 10 μm x 10 μm inner diode and a 25 μm x 25 μm outer ring diode separated by a 2 μm gate width. The shape of the large diode is defined in FIGURE 12. The metal lines are mapped on the top of the large diode.

The large diode contains three metal pads: the middle one is used for wiring, and the other two are only used as references. The area enclosed by the square box corresponds to the beam scanning area (240 μm x 240 μm). The labeled areas A, B, and C in FIGURE 12 were selected to study the charge collection efficiency with different reverse biases applied to the large diode. The following charge collection studies on the ring-gate-inner FET and large diode were reported previously in the literature by our research group [146,147].

FIGURE 11-A (in color)

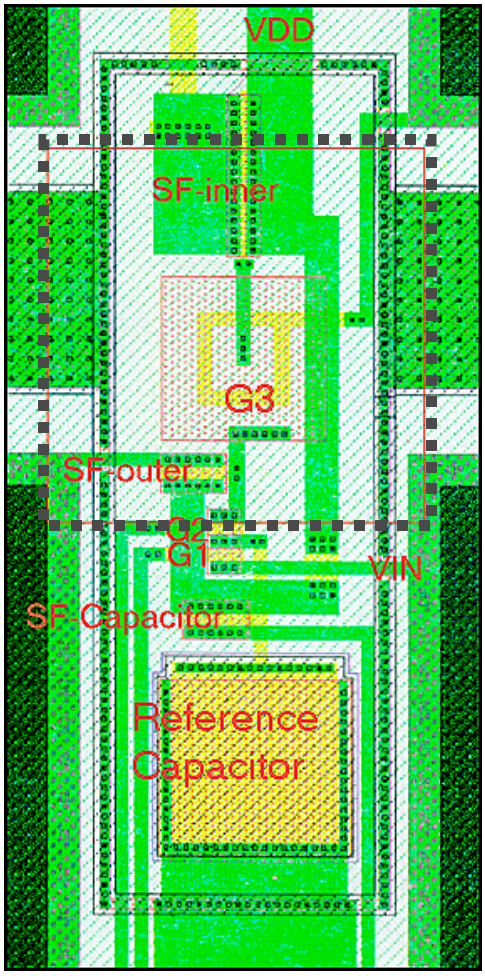

FIGURE 11-B

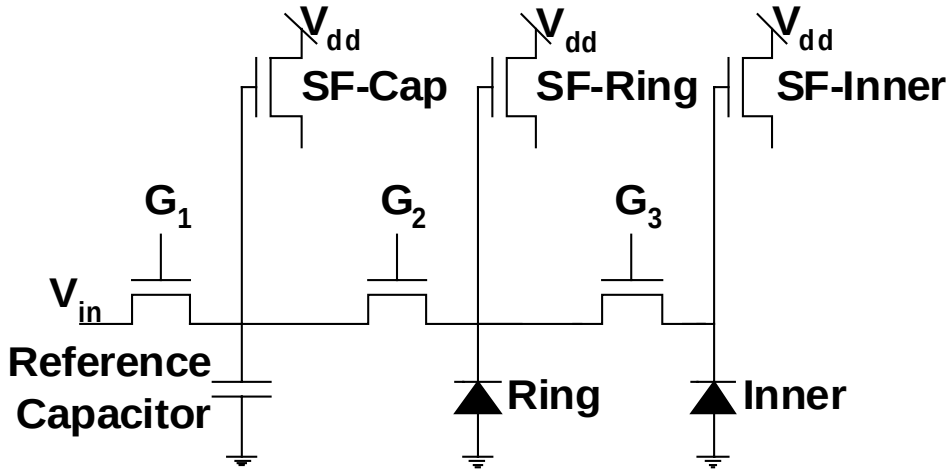

FIGURE 11-C

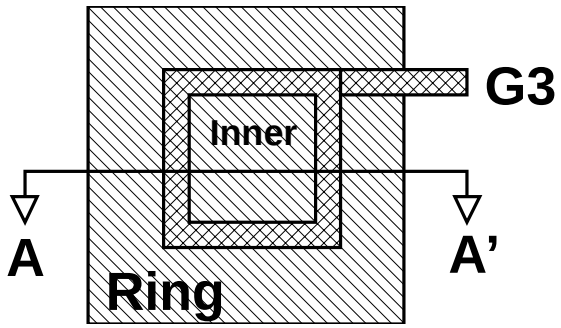

FIGURE 11-D

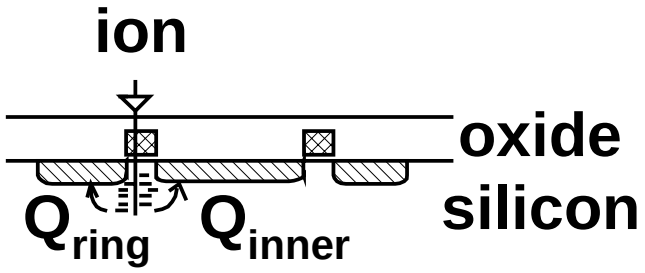

FIGURE 11. 6T-CMOS (Six Transistor Complementary-Metal-Oxide-Semiconductor) test structure design layout (A in color), the equivalent circuit diagram (B) and charge collection node (C) with cross sectional view (D). The area in A surrounded by the thick dash line is the outer ring-gate-inner FET test structure. The labels in A correspond to circuit components in B, which mainly consist of inner-, ring-, capacitor- Source Followers (SFs), gates G1, G2, and G3, inner and ring diodes, and reference capacitor. The charge collection ring and inner diodes (C and D) are formed from the contact diffusions of an *n*-channel MOSFET transistor in a *p*-substrate. The gate (G3) of this transistor is a square ring, completely enclosing the inner diffusion diode.

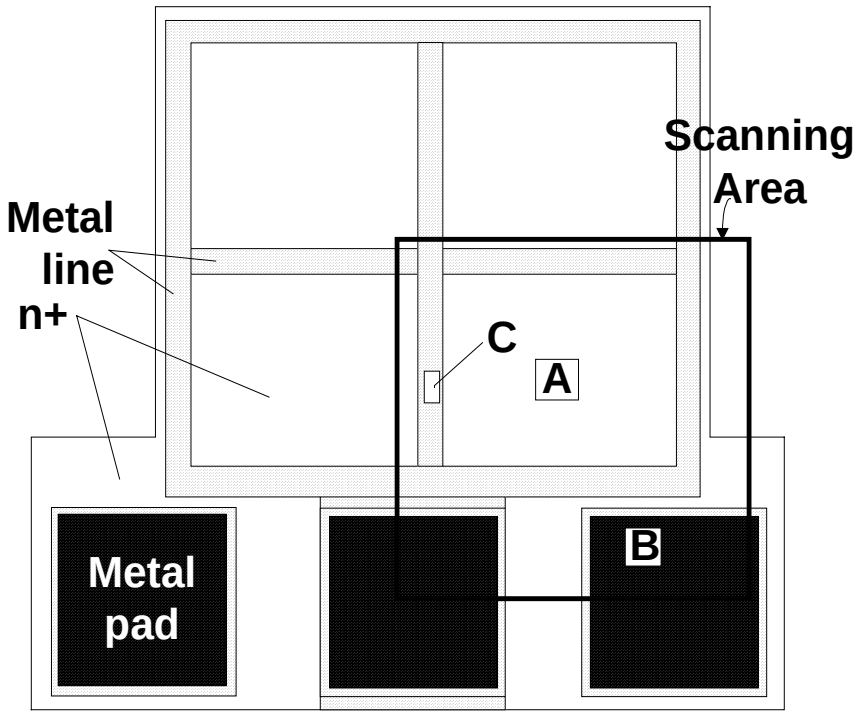

FIGURE 12. The design layout for the large diode. The areas labeled A, B, and C were selected to study charge collection efficiency with different reverse biases. A, B, and C correspond to the large diode with SiO_2, metal pad, and metal line as top layer, respectively. The solid areas of the metal pads were 100 μm x 100 μm window cuts used to bond wires.

Experimental Results and Discussion

FIGURE 13 and FIGURE 14 are IBICC measurements on the outer ring-gate-inner FET with gate G3 off (0V bias) and gate G3 on (4V bias), respectively. The drains of the source followers (V_{dd}) and the V_{in} in FIGURE 11 were tied together and fed into the preamplifier, which was biased at 3 V. The sources of the source followers were biased at -1.4 V. The gates (G1 and G2) were set on with 4V bias. The *p*-substrate was grounded. The microbeam was scanned over 60 μm x 60 μm area. The counting rate of charge collection was about 2 x 10^3 count per second (cps).

Because of the different charge collection efficiencies for different regions, the 3D images (FIGURE 13-A and FIGURE 14-A) show the differential charge collection abilities with reference to the IC layout. FIGURE 13-B and FIGURE 14-B are the images based on the median values of collected charge over the scanned region. FIGURE 13-C and FIGURE 14-C are charge collection cross sectional views from the slices shown in FIGURE 13-B and FIGURE 14-B, which are cut along with X-axis at the central Y-axis. FIGURE 13-D, -E, -F and FIGURE 14-D, -E, -F are images made by grouping the charge collection layers based on the design layout, which also correspond to the labeled collected charge ranges in FIGURE 13-C and FIGURE 14-C.

In FIGURE 13-A, -C and FIGURE 14-A, -C, the values of the Y-axis are calibrated by charge collection from a virgin spot of the pin diode (Hamamatsu Model S1223). As discussed above, the energy loss (~25 keV) for the 10 MeV carbon beam through the 1000 Å silicon dioxide top layer of the pin diode can be ignored. Since a 15 V reverse bias applied across the pin diode ensured that the width of the pin diode depletion layer was larger than the range of 10 MeV carbon ions, the induced charge can be assumed to be collected by the pin diode with 100% efficiency. Hence, the total charge collected by the pin diode was used to calibrate the electronics and the measurements.

In the central region of FIGURE 13-A and -F, the collected charge forms a square crater shape and a hollow square region, respectively. The crater and the hollow square correspond to the area enclosed by G3. As a comparison with the central region of FIGURE 14-A and -F, the charge forms a flat mesa and a square, respectively. The mesa and the square can be related to the entire area of the FET.

The discontinuities of the collected charge in FIGURE 13-C and FIGURE 14-C indicate the transition from the outside to the inside of the outer ring diode. Initially, the drift and funneling assisted charge collection are the dominant mechanism when the ions strike the region of the ring diode. In FIGURE 13-D, -E and FIGURE 14-D, -E, the charge is collected from the outside of ring diode except the central region of FIGURE 13-E. When ions strike outside the ring diode, charge is exclusively collected by the outer ring diode, whether the G3 is on or off, and the collected charge decreases as the ions strike spots further away from the diodes. In the central region of FIGURE 13-E, the charge is collected from the inner diode. There are two channels (through V_{in} and through V_{dd} of the source followers) to the preamplifier for charge collection. When the G3 is turned off, the charge is coupled in AC fashion to V_{dd} through the gate oxide capacitance of the source follower transistor. The collected charge is an indication of the voltage change when ions strike the inner diode. Also, charge is localized to the inner diode when ions directly strike the inner diode as seen in FIGURE 13-E. With reference to the FIGURE 13-C and FIGURE 14-C, the charge is localized to the diodes when ions directly strike the diodes, and the total charge collected by the diodes is about 80fC.

FIGURE 13-A

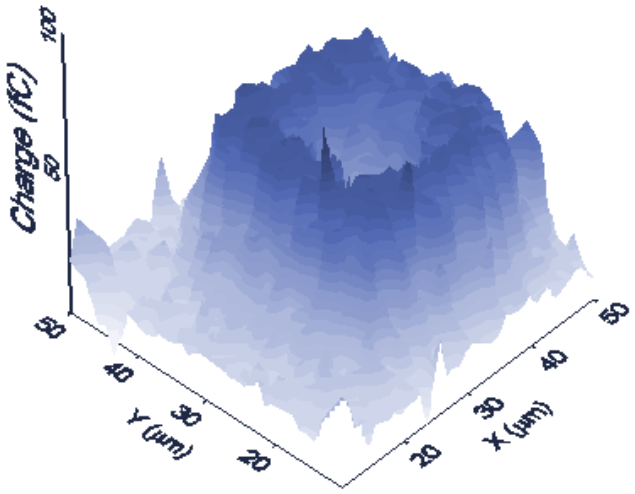

FIGURE 13-B

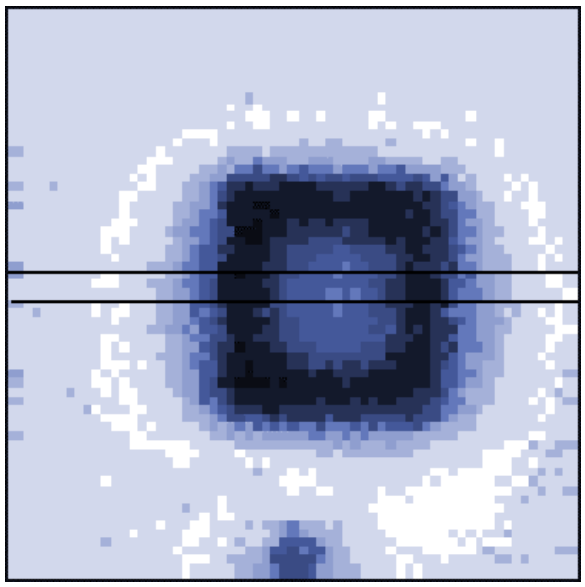

FIGURE 13-C

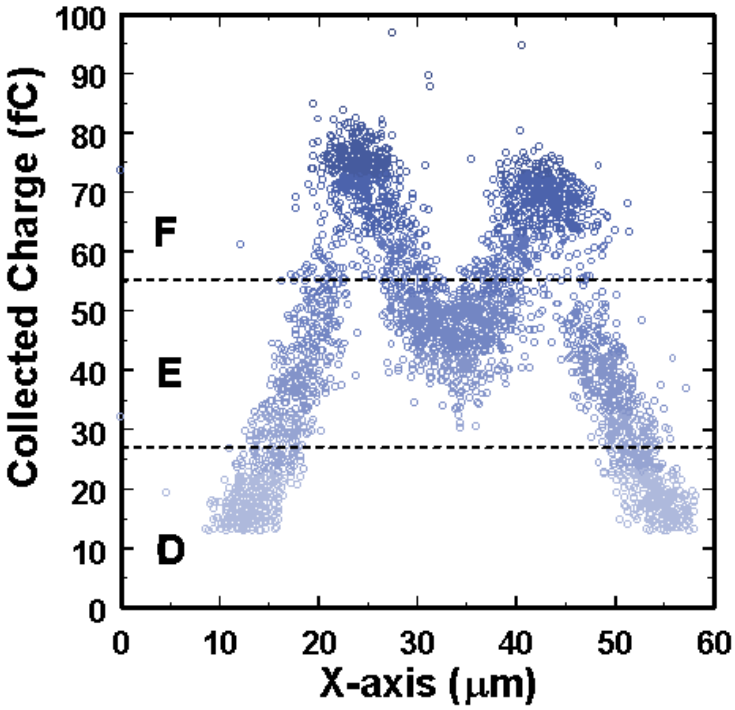

FIGURE 13-D

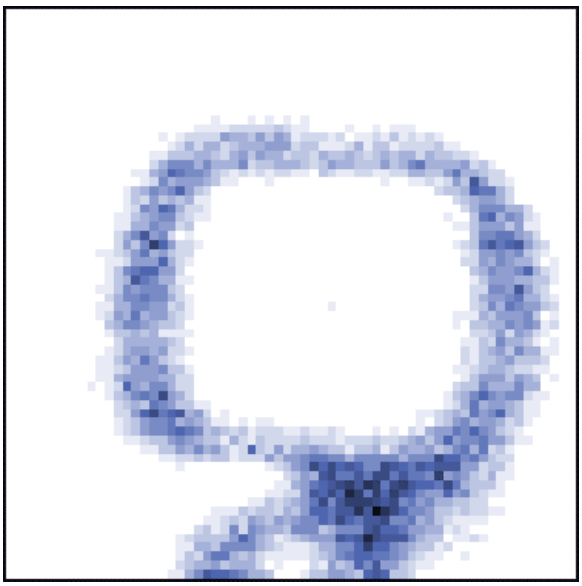

FIGURE 13-E

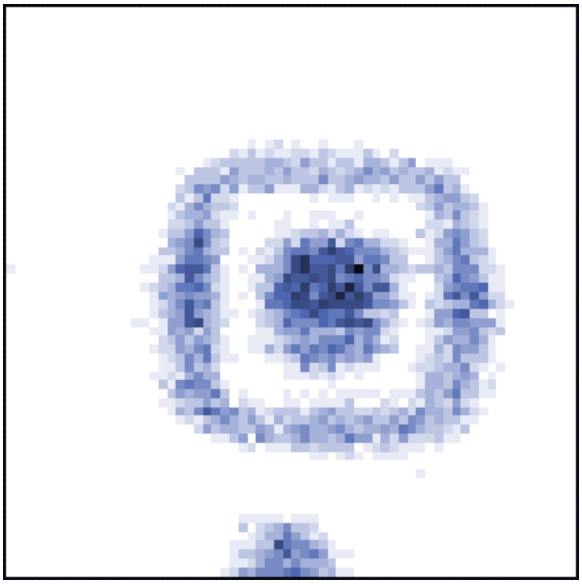

FIGURE 13-F

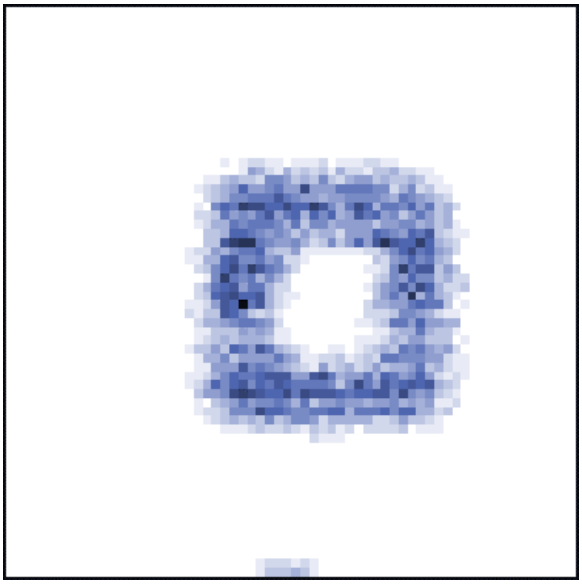

FIGURE 13. IBICC measurement on ring-gate-inner FET (Field Effect Transistor) of 6T-CMOS test structure with G3 off. The scanning area corresponds to the area surrounded by the thick dash line shown in FIGURE 11-A. The horizontal direction is X-axis, and vertical direction is Y-axis unless it is labeled otherwise. A is the 3D image around the FET. B is the median value image of the collected charge. C is the cross sectional view of the slice that is cut along the X-axis at the central Y-axis in D. Also, the labeled charge collection ranges in C are corresponding to D, E, and F, which are images formed by grouping the collected charge layers of the 3D image based on the design layout.

FIGURE 14-A

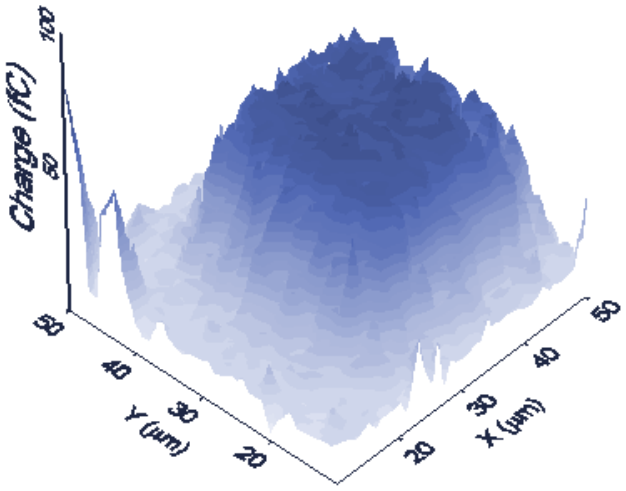

FIGURE 14-B

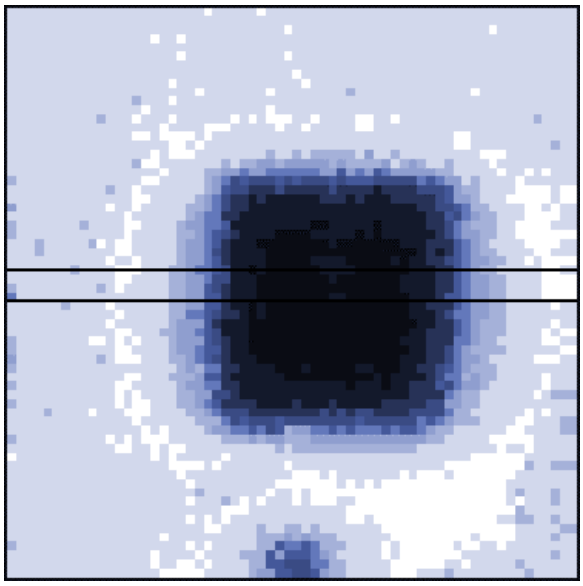

FIGURE 14-C

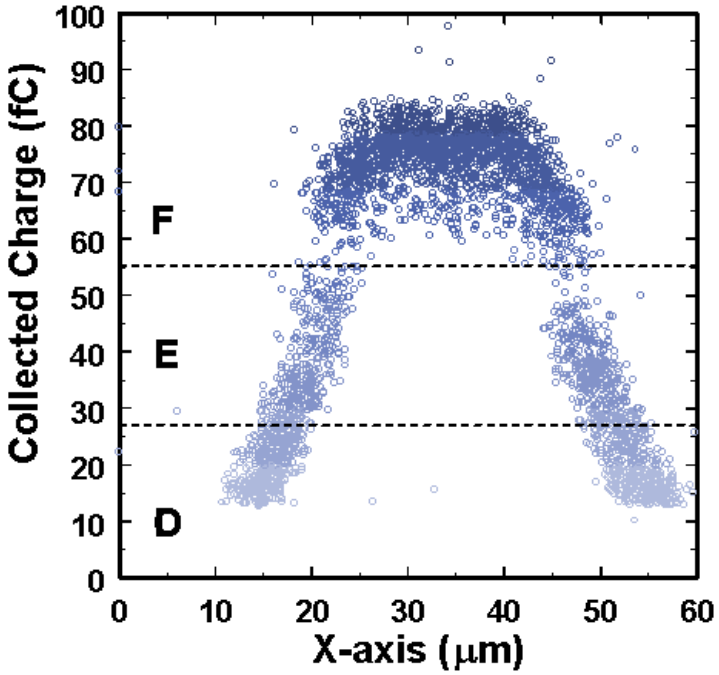

FIGURE 14-D

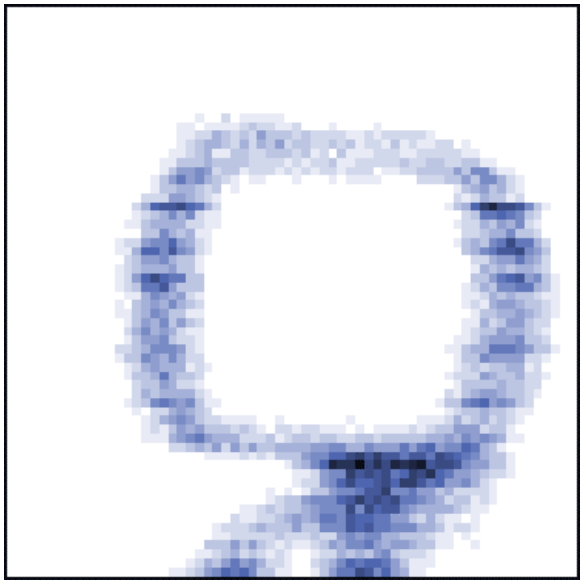

FIGURE 14-E

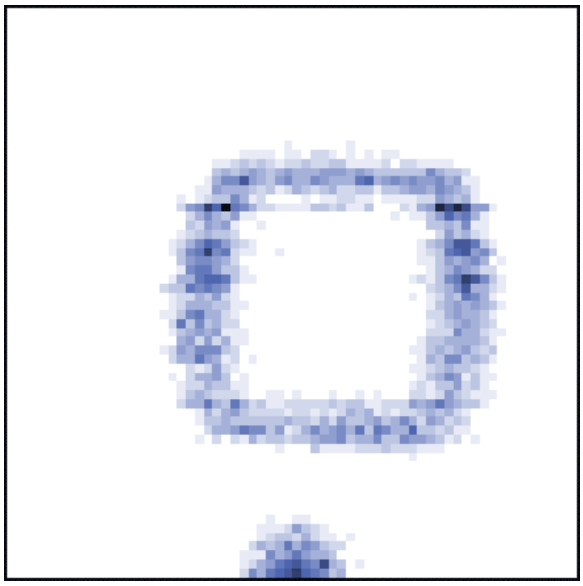

FIGURE 14-F

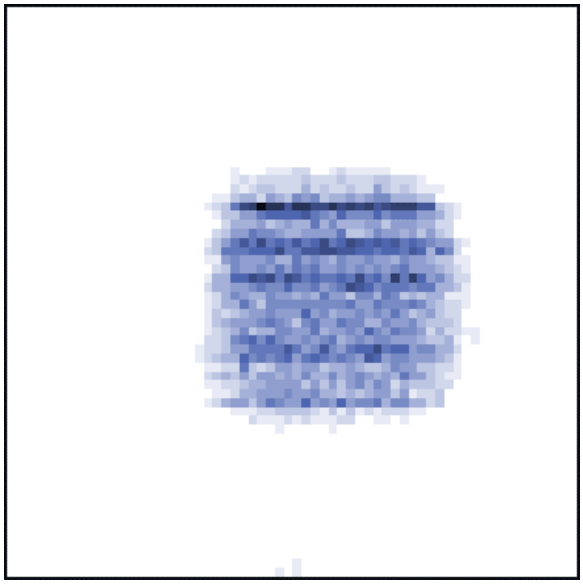

FIGURE 14. IBICC measurement on ring-gate-inner FET with G3 on. Other details are the same as in FIGURE 13.

When ions strike the gate area with G3 off, the collected charge is smaller than that with G3 on, and decreases with distance when the ions strike closer to the inner diode but further from the gate area (FIGURE 13-C). When G3 is turned off, only the charge coupled through the V_{dd} of the inner source follower is registered as the ions striking spot moves closer to the inner diode. When G3 is turned on, the charge from the gate area is totally collected through both channels. Therefore, the charge is shared between the inner and outer ring diodes when ions strike the G3 area as shown in FIGURE 11-D.

From FIGURE 13-A, -B, -C and FIGURE 14-A, -B, -C, the 3D images around the FET, median-value and cross sectional views of the collected charge confirm the above explanation. It is interesting to note that a junction is shown at the lower part in FIGURE 13-B and FIGURE 14-B, which locates another independent source follower. This source follower includes a *pn* junction directly coupled to V_{dd}. Also, this source follower is located outside of the FET. The charge collection from this source follower confirms that the charge collection from V_{dd} exists. But it is direct charge collection rather than the AC coupled charge collection to the inner diode through the source follower gate.

The measured charge is about 80 fC when ions directly strike the charge collection node from the outer ring-gate-inner FET (inner diode size 10 μm x 10 μm). Previous work using 11MeV F ions from a pin-hole apertured microbeam at UNT showed that the collected charge for ions directly striking the inner diode (5 μm x 5 μm) is about 110 fC [60,61]. With reference to the Bragg curves in FIGURE 4 for the different ion species with the same effective track length in silicon, the values are consistent. This leads to another interesting question about how much collected charge is

contributed by the AC charge coupling through the V_{dd} of the inner source follower. The flat top of the charge collection with gate G3 on (FIGURE 14) suggests that the AC coupling charge is a secondary contributor compared to the direct charge collection by the diode. This may be due to different response times between charge collection from the diode and the source follower. In FIGURE 13-C and FIGURE 14-C, charge collection has non-symmetric shoulders for the two sides of the ring diode. This is due to a metal line that runs above the right side of the outer ring diode (FIGURE 11-A). Because of the different energy losses of aluminum versus SiO_2 as the particles pass through the overlayers before reaching the junctions, the collected charge is slightly different for the two sides of the ring diode.

IBICC measurements on the large diode are shown in FIGURE 15. FIGURE 15-A is the 3D image rotated 90 degree counter-clockwise compared to the area shown in FIGURE 12. FIGURE 15-B shows the median values of the collected charge from selected areas (A, B, and C as shown for the large diode in FIGURE 12) plotted against the reverse biases, which were applied to the large diode through the charge collection preamplifier. Basically, the collected charge under the metal line and the metal pad follow the same ascending trend as the large diode with increasing reverse bias. The similarity among the trends can be demonstrated by shifting the curves with constant offsets. Because there are window cuts on the metal pads which are used to bond the packaging wires, the charge collected from the metal pad is more than that from the metal line. This indicates that the main difference in collected charge is the differential energy loss as the particles pass through the overlayers such as SiO_2, metal pad and metal line. These differential energy losses also confirm the explanation of the non-symmetric

shoulders for the two sides of the ring diode as shown in FIGURE 13-C and FIGURE 14-C.

It is observed that the charge collection from the large diode is about three times larger than that from the ring-gate-inner FET test structure. It has been suggested that the larger junctions have higher efficiencies for charge collection [148]. The reason is that the large diode has a bigger solid angle for collecting the induced charge along an ion penetrating track than that for the smaller outer ring-gate-inner FET test structure.

The ion induced damage would shorten the minority diffusion length, and therefore the reduction of the collected charge should be observed. During the IBICC experiments, the fluence was about 2000 cps and the accumulated dose was about 30 ions/μm^2. The experimental results were recorded in the list mode, and the data sequence preserved the variation of the charge collection with the accumulated dose. An off-line analysis of the experimental data shows that the reduction of the collected charge due to ion induced damage can not be distinguished from the poorer statistics of collected charge with small doses (~30 ions/μm^2).

FIGURE 15-A (in color)

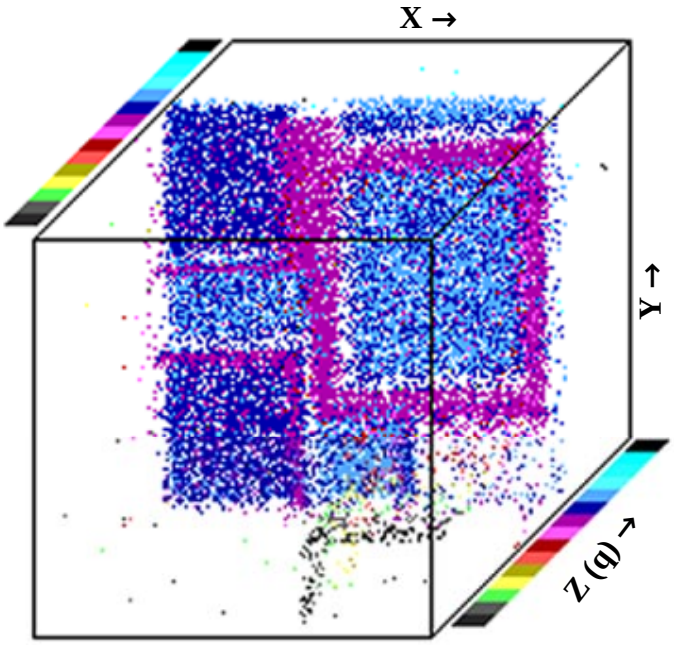

FIGURE 15-B

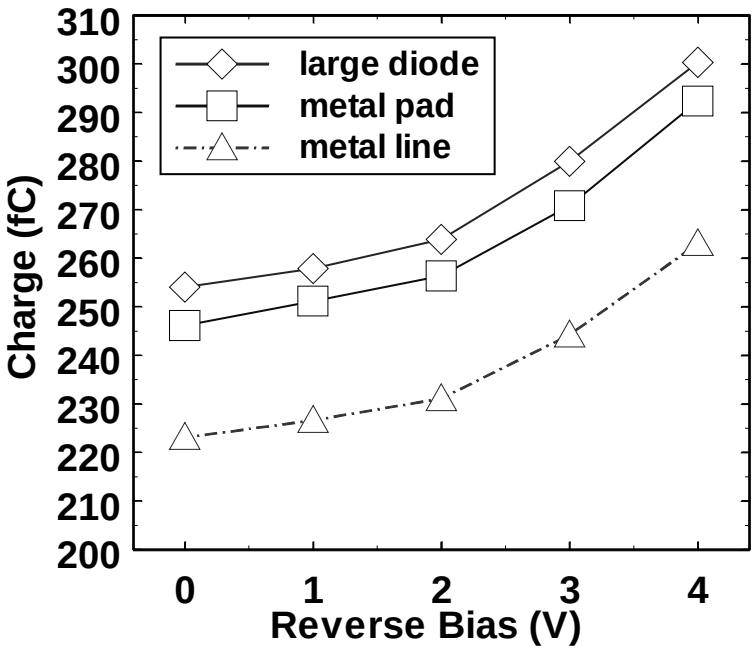

FIGURE 15. IBICC measurements on the large diode as shown in FIGURE 12. A is 3D image (in color) rotated 90 degree counter-clockwise compared to scanning area in FIGURE 12. B shows the median values of collected charge from the selected areas A, B, and C shown for the large diode in FIGURE 12 versus various reverse biases applied to the large diode.

Summary

A 10 MeV carbon microbeam with a 1 μm diameter beam spot was used to scan a test node of a 6T-CMOS test structure. With the aid of the test structure design information, the differential charge collection efficiency from several locations was analyzed. 1) When ions strike outside the FET, the charge was only measured on the outer ring and it decreased with strike distance from this diode. 2) When ions directly strike the inner and outer ring diodes, the collected charge was localized to these diodes. 3) The charge for ions striking the gate region was shared between the inner and outer ring diodes.

Previous IBICC experimental studies on 6T CMOS test structures employed a pin-hole aperture microbeam instead of the focused ion microbeam, and did not rely on resolving the charge collection from individual parts of the circuit, but rather relied upon coincident charge collection measurements between the inner and outer ring diodes. The present work, which use the high-resolution carbon microbeam, demonstrates the differential charge collection efficiency with the aid of the IC design information, and directly confirms the interpretations made in the earlier work [59-61].

The present IBICC experimental results indicate that charge sharing between the adjacent diodes can be significant. In particular, the effect of charge sharing between adjacent memory nodes in ICs such as SRAMs or DRAMs can result in Multiple Bit Upsets (MBU). MBU can pose a significant problem for Single Event Upset (SEU)

mitigation techniques. In order to detect and correct SEU in a 16-bit word using Error Detection And Correction (EDAC) technique, 6 extra bits are required. A 2-bit MBU in the 16-bit word requires several more bits for detection and correction [35].

As the size of IC continues to shrink, MBU could be more serious challenge to design reliable devices in the future. In Chapter 4, charge sharing between stripe-like junctions is further studied using Diffusion Time Resolved IBICC (DTRIBICC) technique. MEDICI simulations are also presented along with experimental results.

CHAPTER 4

DIFFUSION TIME RESOLVED IBICC (DTRIBCC)

Concepts for DTRIBCC

In order to design more robust semiconductor devices, it is important to evaluate the responses of microcircuits immediately following the ion striking. Transient charge collection can be measured using a nuclear microprobe and a wide GHz bandwidth sampling oscilloscope [90,149-152]. Microbeam techniques can ensure that the transient signal arises from only the interested region. For example, the Transient time Resolved IBICC (TRIBICC) has been used to measure induced transient current at Sandia National Laboratories [90]. This work used a focused ion microbeam to measure the entire current transient induced by single 12-MeV carbon ions at a 5GHz analog bandwidth. Multiple single ion transients at multiple locations of a single CMOS transistor were acquired, and the current transients reveal clear and discernible contributions from drift and diffusive charge collection.

As IC design moves to a smaller scale, it is found that some features of SEU cross sections can be better explained by using models based on the diffusion mechanism rather than models based on the drift and funneling assisted mechanisms [153,154]. Charge collection by lateral diffusion should be taken into account [155,156]. The time

duration of charge collection by the charge collection node can also be estimated to account for the diffused charge collection [157].

Considering the induced charge at the source point *x*, a statistical average arrival time associated with *x* can provide a means to measure the speed of the charge collection process. Assume that the transient current is *I(t)* through the node, then the total charge collection is

$$Q = \int_0^\infty I(t)dt \tag{28}$$

The average arrival time is then defined as

$$T = \frac{1}{Q}\int_0^\infty tI(t)dt \tag{29}$$

Since some carriers may be collected at a much later time, the average arrival time is not be as valuable. We can either ignore some of the late arrivals or use an artificial recombination to eliminate the carriers that would arrive later. Both approaches include some arbitrary approximations. For example, the first approach requires determining how late arrival carriers are ignored. With the second approach, the average arrival time and the charge collection associated with the selected lifetime τ can be defined as

$$T_\tau = \frac{1}{Q_\tau}\int_0^\infty tI_\tau(t) = \frac{1}{Q_\tau}\int_0^\infty tI(t)e^{-t/\tau}dt \tag{30}$$

$$Q_\tau = \int_0^\infty I_\tau(t)dt = \int_0^\infty I(t)e^{-t/\tau}dt\ . \tag{31}$$

Along the ion track, a series of source nodes can be defined. Therefore, the average arrival time can also be applied to estimate the speed of charge collection for the

ion track. Diffusion Time Resolved IBICC (DTRIBICC) can be used to measure the average arrival time for an ion track using a multiple parameter data acquisition system in addition to the charge collection by junctions (FIGURE 16). When ions strike an IC structure, say a long narrow *pn* junction extended in the Y direction, the charge collected by the junction is recorded along with the striking spot coordinates. The time it takes for the charge to reach the junction through diffusion can also be recorded as a new parameter for study. One can use a Time-to-Amplitude Converter (TAC) to measure the diffusion time. The start signals for the TAC can be trigged by Secondary Electrons (SE) emitted from the sample surface as a result of ions striking the sample [158]. A scintillating foil placed in front of the sample can also be used as the TAC start trigger [160]. The stop signals can be the timing output from the preamplifier that is connected to the junction to measure the collected charge. Thus, the diffusion time from a specific striking spot to the junction can be recorded along with the amount of the collected charge and the coordinates. The measured diffusion time can be regarded as the average arrival time of the diffused charge, which can be related to the first moment (or the average time) of the arrival carrier density at the junction. The magnitude of the average arrival time for diffused charge collection can be crucial to understanding and mitigating radiation induced circuit malfunctions during normal IC operations. The diffusion time can be used to window the diffusion charge collection by the junction relative to the beam striking spots. With the new diffusion time parameter, the induced charge transport in the semiconductor can be characterized more accurately, and other parameters such as the mobility can be obtained.

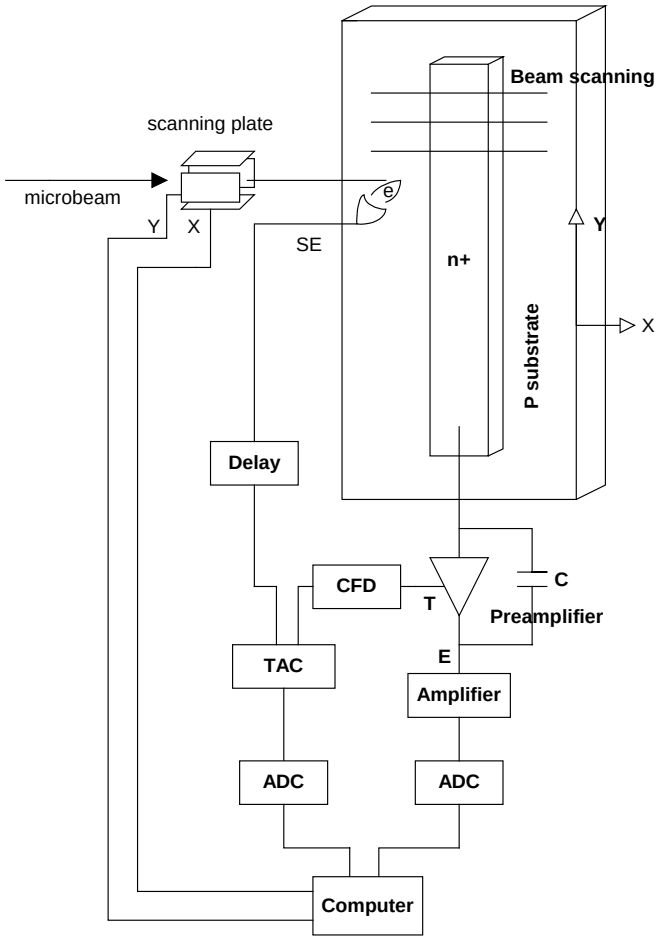

FIGURE 16. Schematic diagram for Diffusion Time Resolved IBICC measurement using multi-parameter data acquisition system. A Time-to-Amplitude Converter (TAC) is used to measure the diffusion time for the charge diffusion from the striking spots to the junctions.

Experimental Details

Test structure for DTRIBICC measurements

Since there is no suitable start trigger available yet, relative arrival time rather than absolute arrival time was measured on the stripe-like junction test structure. On the specially designed ICs, the outer-inner diode test structure (FIGURE 17-A) is suitable for the relative average arrival time measurement using the proposed DTRIBICC technique.

The inner and outer diodes are formed from the contact diffusion in a *p*-substrate. The inner diode consists of a 100 μm x 100 μm square region and two wings (100 μm x 2 μm) along the two edges. At the ends of wings, it shrinks as two tips (10 μm x 1 μm). The inner diode is surrounded by the continuous 2 μm wide outer diode. The 2 μm separation between the inner and outer diodes was chosen to be the approximate node-to-node spacing of memories. The inner and the outer diodes are connected through different metal pads to external package wiring. The surface passivation oxide layer and the diffusion doping barriers are also shown in cross sectional view AA' in FIGURE 17-B. FIGURE 17-C and -D are two separated IBICC measurements with a 10 MeV carbon microbeam from the outer and inner junctions, respectively. The experimental conditions were the same as the experimental setup on the large diode shown in Chapter 3. The microbeam was scanned over 240 μm x 240 μm, and both outer and inner junctions were biased at 0 V. FIGURE 17-C and -D clearly reveals the charge collection from the inner and outer junctions. When ions strike the large square portion of the inner junction, the inner junction has a larger solid angle to see the ion track compared with solid angle seen by the stripe portion of the inner junction. Hence, it is expected that the amount of charge is higher for the square portion than the winged portion of the inner diode (FIGURE 17-D).

FIGURE 17-A (in color)

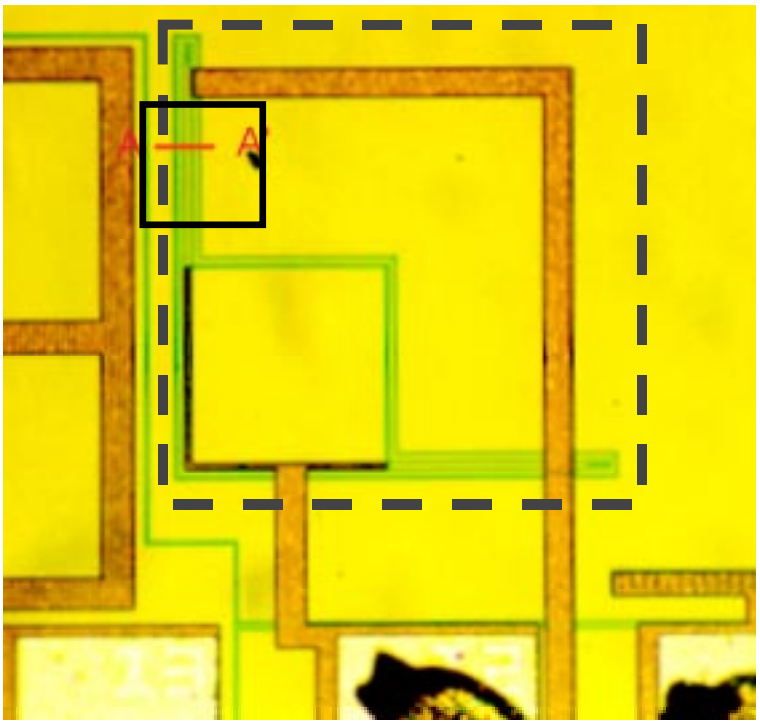

FIGURE 17-B

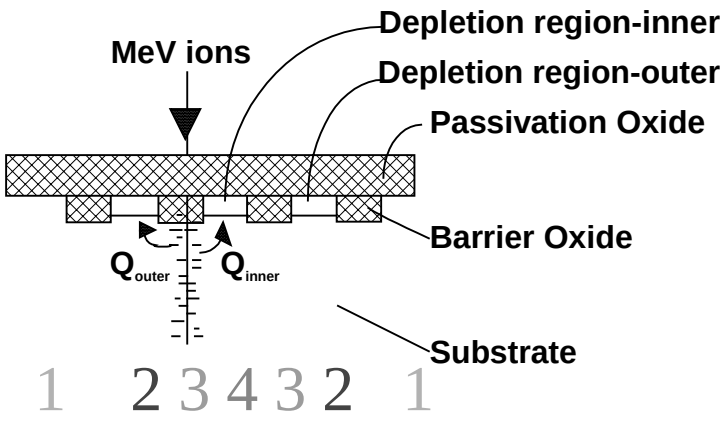

FIGURE 17-C (in color)

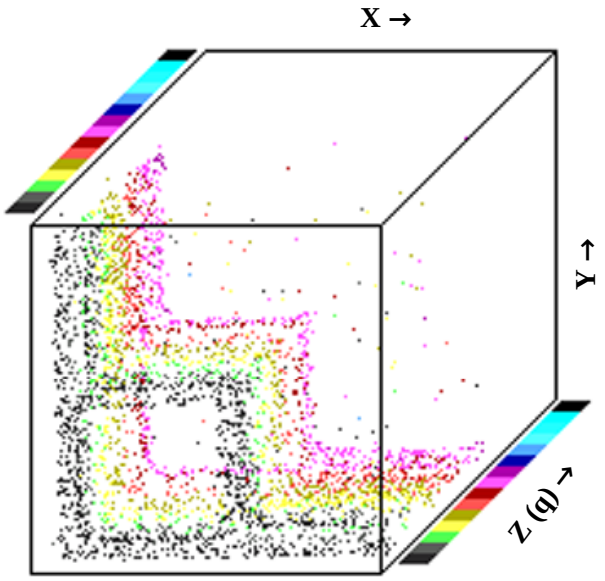

FIGURE 17-D (in color)

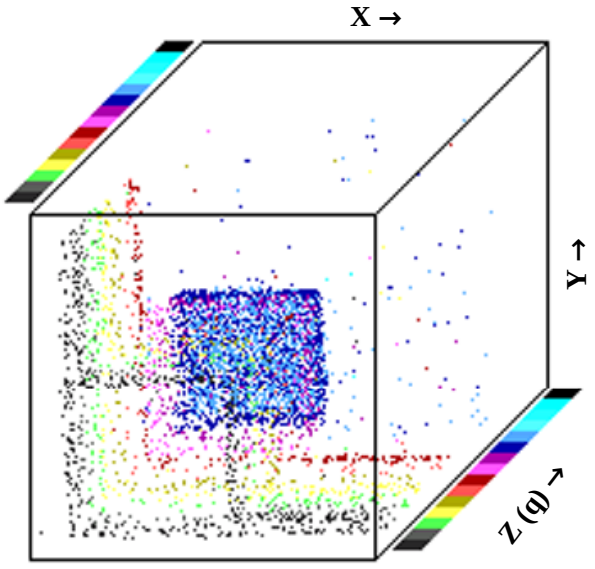

FIGURE 17. Photo of the inner-outer diode test structure for the Diffusion time Resolved Ion Beam Induced Charge Collection (DTRIBICC) measurement (A), and the cross sectional view along AA' (B). C and D are IBICC measurements with the 10 MeV carbon beam on outer and inner junctions, respectively. The scanning area (240 μm x 240 μm) corresponds to the area surrounded by the dash line shown in A.

Experimental setup

Three data collection channels were simultaneously used to measure the charge collection from the outer and inner diodes, and the relative diffusion time. The experimental setup for the charge collection from the outer and inner diodes was the same as described previously in Chapter 3. Two separated 4 V reverse biases were applied to outer and inner diodes through two preamplifiers (Ortec 142A). The *p*-substrate was grounded. The timing outputs from the two preamplifiers were fed into two Constant Fraction Discriminators (CFD, Ortec 583). The two fast timing outputs from CFDs were then fed into a TAC as the start (from the outer junction) and stop (from the inner junction) signals. The TAC signals were further digitized by an Amplitude-to-Digital Converter (ADC) and were coincidentally recorded along with striking spot coordinates and collected charge from the two junctions. The TAC range was set at 100 ns. A 48 ns offset was inserted into the stop signal channel to provide flexible measurements for different experimental conditions as described later. Also, the time scale was calibrated with an nanosecond delay box (Ortec DB463). The total charge collected by a pin diode was used to calibrate the charge collection electronics. The counting rate for charge collection was about 400 count per second (cps). The microbeam was scanned over a 60 μm x 60 μm area, which was calibrated with known feature sizes of scanning test structures. In order to minimize ion induced damage effects on the samples, the test structures were optically targeted using a front viewing microscope and then scanned by the beam. Because of the 2 μm separation between the outer and inner junctions, the microbeam size must be < 1 μm. The following are the experimental results on the stripe-

like junctions using a 12 MeV carbon microbeam with a multiple data acquisition system at Sandia National Laboratories. The beam diameter size was ≤ 1 μm.

DTRIBICC Experimental Results

With a multiple parameter data acquisition system, charge collection from the outer and inner diodes was simultaneously measured. As the beam scans along the AA' direction in FIGURE 17 -A, the time difference between the outer and inner diodes was measured using the DTRIBICC technique. When the beam scans across AA' as shown in FIGURE 17-B, the TAC registered the charge collection timing difference between the outer and inner junctions. The TAC functions in the following manner. When the start signal (from the outer junction) came before the stop signal (from the inner junction) and the time difference was within the TAC converting range, an output analog signal was given. The amplitude of the output analog signal is proportional to the time interval between the start and stop signals. However, when the stop signal comes before the start signal, or there is no stop signal at all, or the time interval is beyond the TAC range, the TAC will reset itself and give no output. In order to increase the dynamic measurement range, a 48 ns time delay was inserted into the stop signal channel to provide flexible measurements for different conditions as described later.

FIGURE 18 is a DTRIBICC charge collection measurement on the outer-inner junctions. FIGURE 18-A and -C are the median value images of charge collection from

the inner and outer junctions, respectively. FIGURE 18-B and -D are the cross sectional views of slices that are defined in FIGURE 18-A and -C. FIGURE 19-A is the cross sectional view of the DTRIBICC relative arrival time measurement, which also corresponds to positions of slice views defined in FIGURE 18-A and -C. FIGURE 19-B is the histogram of the relative arrival time measurements on the outer-inner junctions and corresponds to the times in FIGURE 19-A. FIGURE 18-B and -D are numerically-coded using the measured relative arrival time as shown in FIGURE 19-A. The numerical coding in FIGURE 18-B and -D corresponds to the relative arrival time high counting peak at t=0 ns (out of scale) and three peaks around (52-63), (44-52), (35-44) ns in the range of 35-63 ns as shown in FIGURE 19-B. There is no count below 35 ns except at t=0 ns. The numerical coding also corresponds to the striking spots shown in FIGURE 17-B.

The TAC start and stop signals were triggered from the timing outputs of two preamplifiers connected to the outer and inner junctions, respectively. When the ion strikes exactly in the center of the outer and inner junctions, the TAC should record the offset, 48 ns. When the ions strike closer to the outer junction, the TAC should give t>48 ns (or t<48 ns when closer to the inner junction). In FIGURE 18-A and -C, the images of the median filtered charge clearly reveal the inner and outer junctions. The charge collection projections in FIGURE 18-C and -D indicate:

1) When ions strike outside of and far away from the outer junction, the charge is collected by the outer junction through the diffusion process, and no charge is collected by the inner junction. As the beam strikes closer to the outer junction, the inner junction begins to pick up some charge through diffusion. When the ion strikes outside the outer

junction, the start signals come in ahead of the stop signals. If the induced charge takes more than 52 ns to be collected by the inner junction, then the TAC will be out of the 100 ns range and will give a zero TAC output. Compared with situations discussed below, the induced charge should diffuse and collect in less than ~20 ns by the inner junction, as shown in FIGURE 19. Also, as shown in FIGURE 18-B and -D, the charge collection by the inner junction for ions striking outside of the outer junction is not enough to trigger the CFD in the stop channel. Therefore, the TAC goes to full scale waiting for the stop. Since there is no stop timing signal triggered, the TAC resets itself and gives zero output as shown in FIGURE 19. The majority of the counts in the t=0 ns peak was attributed to the lack of stop signals.

2) As ions strike directly or closer to the outer junction from the outside, some charge is collected by the inner diode through diffusion. Once the stop timing signals are triggered, non-zero TAC signals are registered which correspond to the peak around (52-63) ns, shown in FIGURE 19-B.

3) When the ions strike between the outer and inner junctions, the induced charge is shared between the two junctions. The peak around the (44-52) ns, shown in FIGURE 19-B, corresponds to ion striking between the outer and inner junctions. Depending on the ion striking position between the inner and outer junctions, the timing signals arrive between (44-48) ns or (48-52) ns. When ions strike in the middle of the outer and inner junctions, the TAC will record the relative arrival time as 48 ns.

4) The peak around (38-44) ns, shown in FIGURE 19-B, corresponds to ions that directly strike the inner junction. As ions directly strike the inner junction, the inner junction can not totally collect the induced charge and the outer junction will pick up

some charge through diffusion. Since there are two paths for the diffused charge reaching both sides of the outer junction, the TAC will record the relative arrival time once the diffused charge reaches the closer side of the outer junction. Considering the fact that the ions scan along AA', passing through outer junction twice and inner junction once, the striking outer junction peak around (52-63) ns has more counts than the striking inner junction peak around (38-44) ns. Also, the inner junction peak has a narrower half width than the outer junction peak around (52-63) ns as shown in FIGURE 19-B.

5) The large increases at the peaks in FIGURE 18-B and -D indicate the transition from the outside (barrier oxide) to the inside of the junctions. Also, it indicates charge collection through diffusion is not as effective a mechanism to collect the charge compared with directly striking the junction, where the charge funneling is the main charge collection mechanism.

6) Charge collection by the outer junction in FIGURE 18-D revealed that there are some special features outside of the outer junction (the gaps at y=15 μm and y=35 μm) where there is no charge collection at all by the outer junction. Still, the charge collection beyond the gap follows the natural decay of the collected charge by the outer junction as shown in FIGURE 18-D. The gaps in FIGURE 18-A and -C do not have the same causes. In FIGURE 18-A. the gaps at y=15 μm y=35 μm are due to coincident measurements of the data acquisition system. Far from the gaps shown in FIGURE 18-A (y<15 μm and y>35 μm), the inner junction collected zero charge (FIGURE 18-B).

FIGURE 18-A

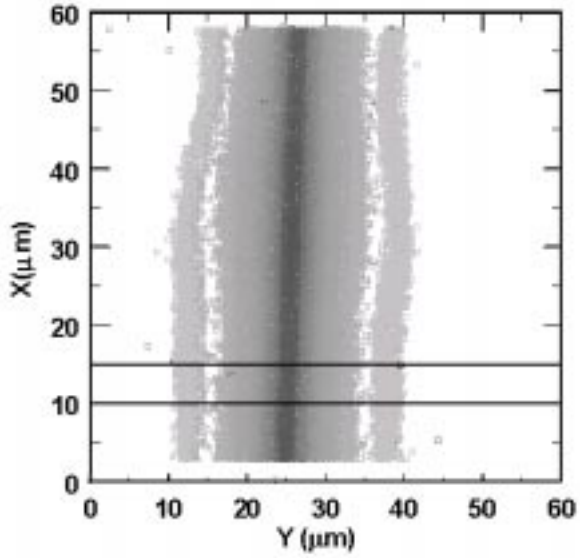

FIGURE 18-B

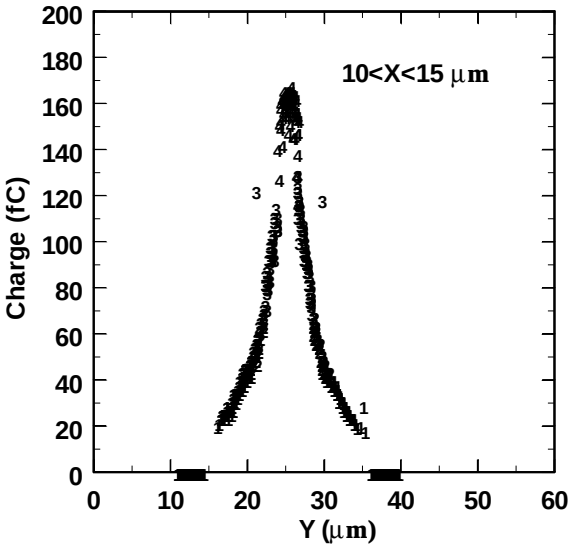

FIGURE 18-C

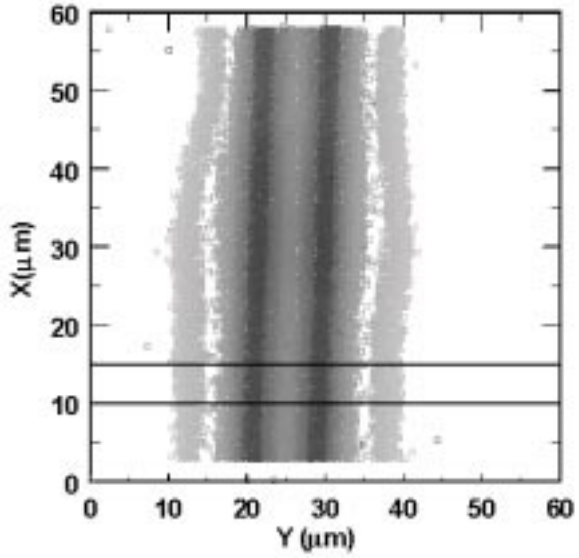

FIGURE 18-D

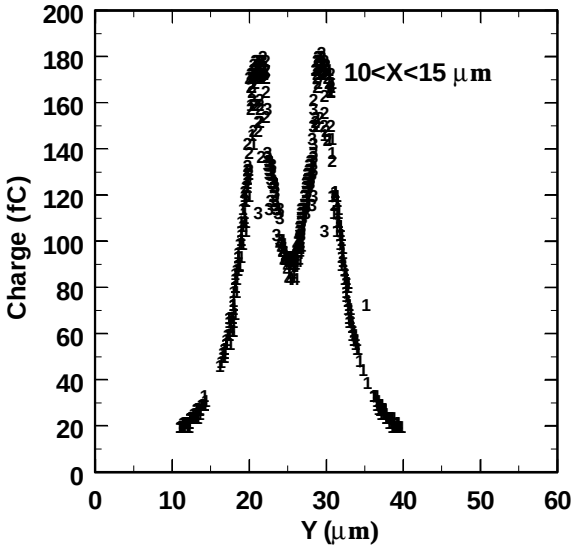

FIGURE 18. DTRIBICC measurement on the outer-inner diode test structure. A and C are the median value images of charge collection from outer and inner junctions. B and D are the cross sectional views of the slices that are defined in A and C. Also, B and D are numerically-coded using the measured relative diffusion times shown in FIGURE 19, which also corresponds to the striking spots shown in FIGURE 17-B.

FIGURE 19-A

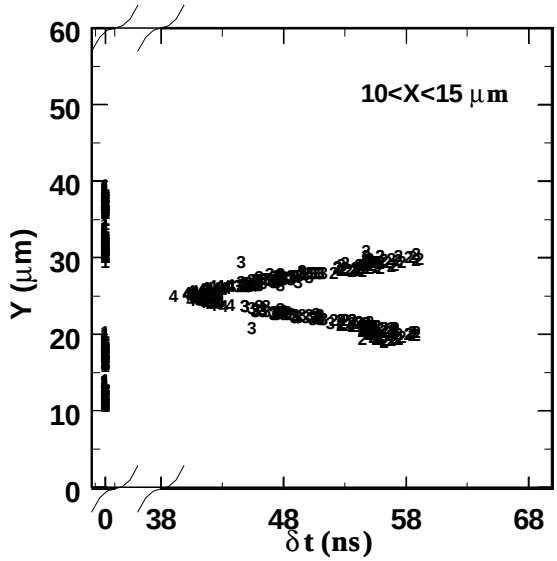

FIGURE 19-B

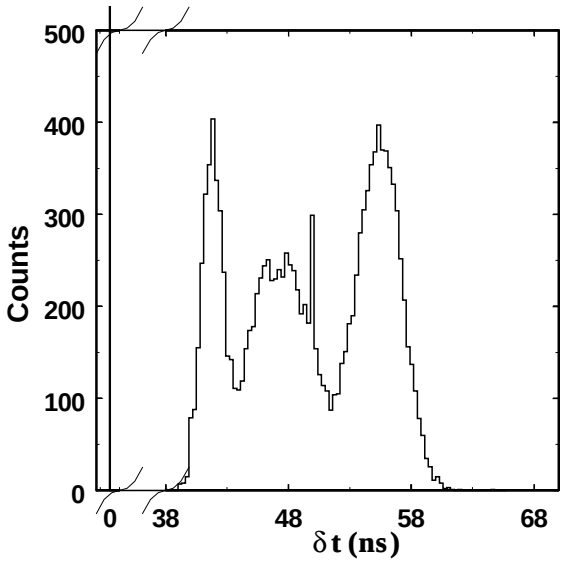

FIGURE 19. DTRIBICC relative arrival time measurement on the outer-inner junction structure. A is the cross sectional view of the relative arrival time measurement, which also corresponds to positions of slice views in FIGURE 18-B and -D. The TAC start and stop signals were triggered by the timing outputs of two preamplifiers which were connected to the outer and inner junctions, respectively. The start signal was delayed by 48 ns to increase the measurement dynamic scale. B is the histogram of relative arrival time measurements on the outer-inner junctions; the four peaks are shown in the range of t=0, (35-44), (44-52), (52-63). The t=0 peak is out of scale.

In FIGURE 20, the collected charge by the outer junction is plotted against the collected charge by the inner junction. The numerical labels correspond to the striking spots shown in FIGURE 17-B. The same numerical coding is used as shown in FIGURE 18. FIGURE 20 clearly reveals the charge sharing between the inner and outer junctions. 1) When ions directly strike the junctions, the striking junction will collect most of the charge, and the other junction shares charge through diffusion. 2) When ions strike between the two junctions, the charge is shared between the outer and inner junctions. In FIGURE 20, the charge sharing between the outer and inner junctions also indicates the ion striking spots, which is very similar to a Position Sensitive Detector. Since the distance between the outer and inner junctions is only 2 μm, the position can be inferred based on the charge sharing with potential ~0.1 μm resolution. 3) When ions strike outside of the outer junction, the inner junction can still pick up some charge through diffusion. The low threshold value of the CFD in the start channel was at about 40 fC during the measurements. The low threshold values of the charge collection preamplifiers were set at about 20 fC. Since the CFDs are used for timing measurements, their relatively high CFD trigger threshold (~40 fC) can only be surpassed by heavy ions with higher LETs.

The experimental results were recorded in list mode, and the accumulated dose was about 10 ions/μm^2. An off-line analysis of the collected data shows that ion induced damage did not affect the charge collected by the junctions at this low dose rate. The relative arrival times were measured using two CFDs, and the uncertainty of the CFD determined the uncertainty of the measurement. The CFDs were triggered by the rising

edges of the preamplifiers. The timing uncertainty was also affected by the capacitance of the junctions. It is estimated that the uncertainty was about 0.5 ns. Still, the timing measurement would provide useful information to determine the charge collection dynamics.

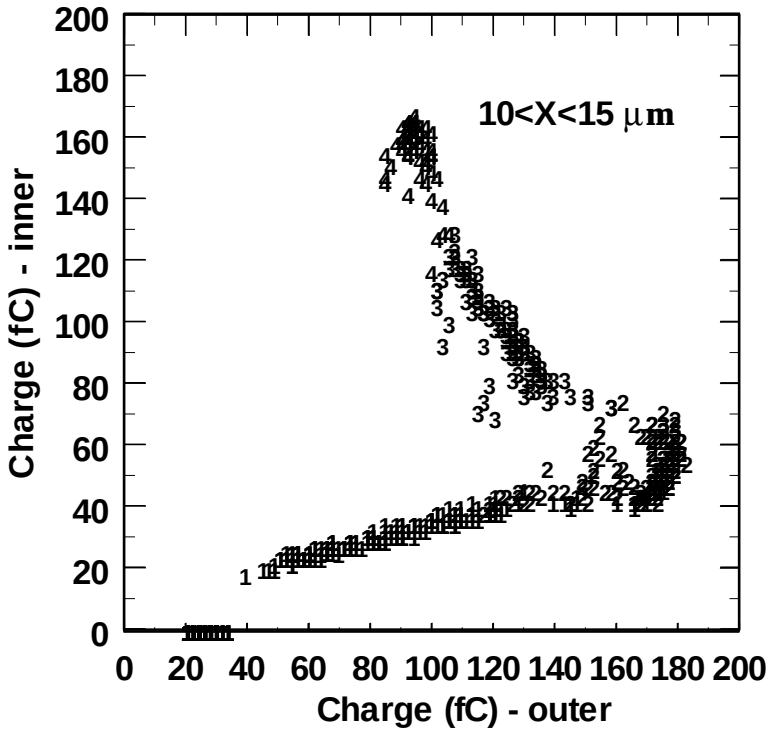

FIGURE 20. Charge collection from outer junction is plotted against that from inner junction.

DTRIBICC Experimental Data Modeling

Since MEDICI simulates the current transients in 2D, the device geometry is chosen to represent the stripe-like junctions (FIGURE 17-B). The induced cylindrical charge along the ion track is distorted in the MEDICI code (FIGURE 6). In Appendix B, MEDICI is used to simulate charge collection from junctions in a cylindrical grid. Most parameters defined in Appendix B also are used to simulate the charge collection from the stripe-like junctions (TABLE 1).

Simulate structure	Stripe-like junctions (FIGURE 17-B)
Top passivation layer	2.2 μm
Diffusion oxide barrier	0.5 μm
Inner junction reversed biases	4 V
Outer junction reversed biases	4 V
Coordinate	2D Cartesian (x,y)
Doping profiles	See FIGURE 32
Models	CCSMOB, FLDMOB, CONSRH, AUGER, BGN
LET (pC/μm)	12 MeV Carbon LET (SRIM96)
Ion track parameters	T_0=3.0x10^{-12} s T_C=1.5x10^{-12} s DCHR=0.2 μm

TABLE 1. MEDICI simulation parameters for the stripe-like junctions.

FIGURE 21 shows transient current responses for ions striking different spots and numbers 1-4 correspond to the labeled positions in FIGURE 17-B. FIGURE 21-A shows the current responses from the inner junction. When ion strikes the inner junction, the transient electron, hole, displacement currents (group #4 in FIGURE 21-A) are an indication of the neutralization of depletion regions (DR) and funneling assisted charge collection happens. When the ion strikes between junctions, diffused charge collection by

the junction becomes dominant (group #3 in FIGURE 21-A). When the ion strikes the outer junction, the collapsed DR leads to a voltage drop on the substrate. The inner junction's response due to this voltage drop on the substrate is shown as group #2 in FIGURE 21-A. When the ion strikes the outside of the outer junction, the inner junction collects charge by diffusion (group #1 in FIGURE 21-A). Similar analysis can be done for charge collection by the outer junction (FIGURE 21-B).

FIGURE 22 shows the MEDICI simulation results for charge collection from the stripe-like junctions. The charge collection is plotted against the simulation time τ

$$Q(\tau) = \int_0^{\tau} I(t)dt \,. \tag{32}$$

FIGURE 22-A is the charge collection from the inner junction as ions strike spots away from the middle of the inner junction, the charge collection is decreasing. The middle of the inner junction is assumed to be the origin in the simulations. When ions strike the inner junction, it is clear that funneling assisted charge collection happens (FIGURE 22-A). FIGURE 22-B and -C are MEDICI simulation results for charge collection from the outer junction. It is also clear that the outer junction collects more charge as ions strike spots closer to the outer junction.

FIGURE 23 are MEDICI simulation results for the average arrival time from the stripe-like junctions. The average arrival time is plotted against the simulation time τ

$$T(\tau) = \frac{1}{Q(\tau)} \int_0^{\tau} tI(t)dt \quad . \tag{33}$$

As ions strike spots closer to the outer junction, the diffused charge takes more time to be collected by the inner junction (FIGURE 23-A) and less time for outer junction (FIGURE 23-B).

From FIGURE 22 and FIGURE 23, charge collection and the average arrival time are about constants at τ>100 ns. Therefore, the charge collection and the average arrival time at junctions are assumed to be the values at the end of simulations.

FIGURE 24 is the comparison of the MEDICI simulation results with the microprobe experimental results. FIGURE 24-A and -B are MEDICI simulations and measurements for a 12 MeV carbon microbeam on the outer-inner diode test structures. FIGURE 24-C and -D are results using a 28 MeV silicon microbeam. The experimental setup for the silicon microbeam is essentially the same as that for carbon microbeam.

Since the stripe-like junction is symmetric along the inner junction, only half the structure is simulated. Simulated relative average arrival time has been adjusted with the 48 ns offset. From FIGURE 24, it is clear that the charge collection by the junction predicted by the MEDICI simulations are in agreement with the experimental results. Since MEDICI does not accurately describe the ion track and device structure in 2D, the difference between simulations and experimental data can be attributed to the distorted ion track in the MEDICI code. Also, a 12 MeV carbon ion has a relative constant LET along its ion track. However, a 28 MeV silicon ion has a decreasing LET along the penetration ion track. The 28 MeV silicon ion has about the same range as the 12 MeV carbon ion. Therefore, the initial several μm along the silicon ion track will have more contribution to relative average arrival time. It is expected that the measured relative

average times are different for different ion species. Simulations based on 3D code, such as DAVINCI, could better predict such differences caused by various ion species.

Summary

The average arrival time of the diffused charge can be related to the first moment (or the average time) of the arrival carrier density at junction. Diffusion Time Resolved IBICC (DTRIBCC) technique is proposed to measure the average arrival time. Charge collection and relative average arrival times are measured on the stripe-like junctions using a multiple parameter data acquisition system. Microbeams (12 MeV carbon and 28 MeV silicon) with a 1 μm diameter spot were used to scan the stripe-like junctions.

The MEDICI simulations are compared with microbeam measurements. 1) The MEDICI simulations are in qualitative and sometimes even quantitative agreement with the experimental results. 2) Lateral diffused charge collection increases the area of the sensitive regions beyond the junctions. 3) DTRIBICC can be used to measure the average arrival time of diffused charge collection at junctions. 4) The average arrival time may be used to define the effective sensitive regions during IC operations. 5) MEDICI can not accurately describe the ion track (correct total induced charge and incorrect induced charge density) and the device geometry at the same time in 2D. To better predict differences caused by different ion species, a 3D simulation code, such as DAVINCI, is required.

FIGURE 21-A (in color)

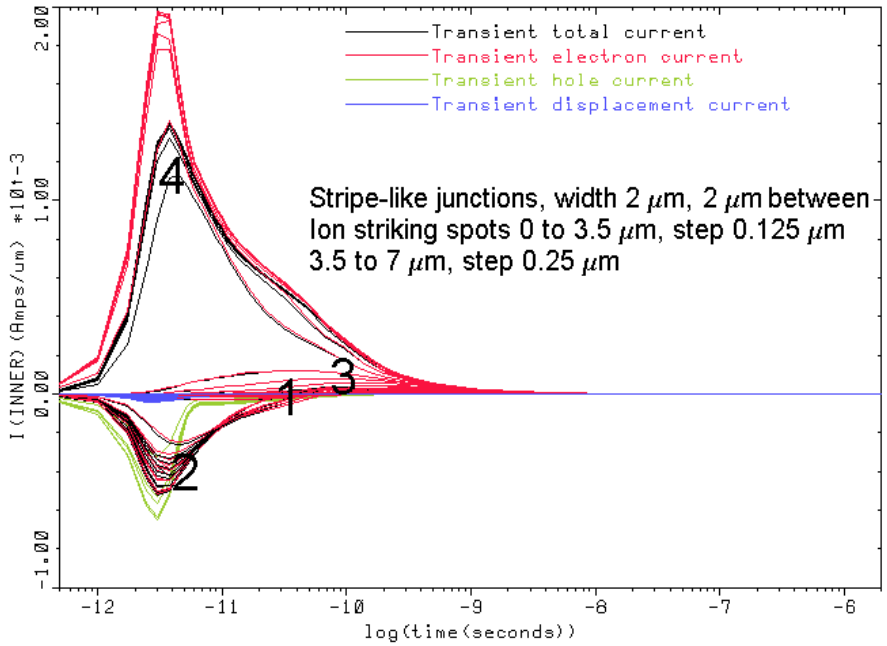

FIGURE 21-B (in color)

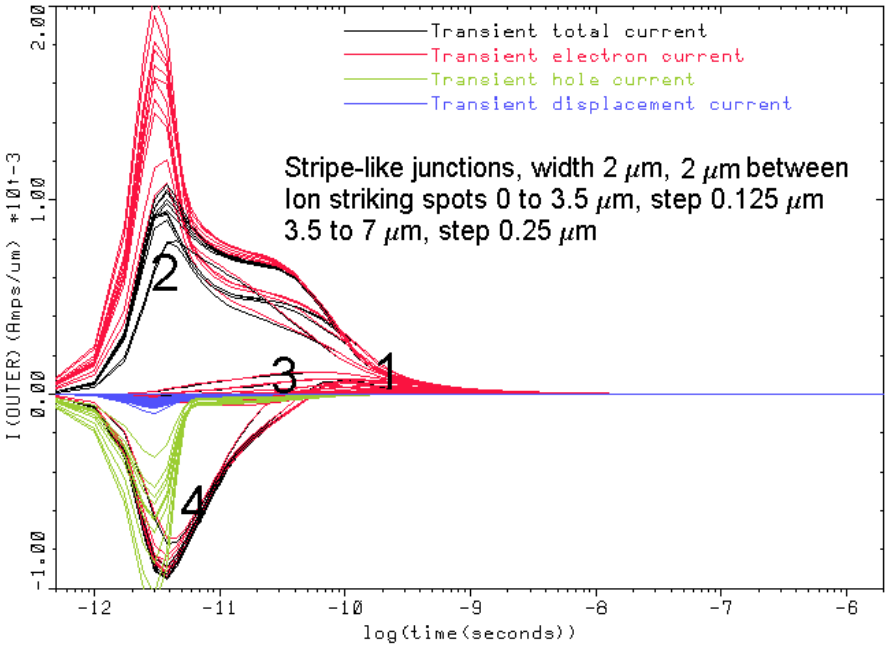

FIGURE 21. Variation of junction currents (total, electron, hole, and displacement transient currents) for different ion striking spots. Numbers 1-4 correspond to labeled positions in FIGURE 17-B. A is the simulation from the inner junction, B is from the outer junction.

FIGURE 22-A

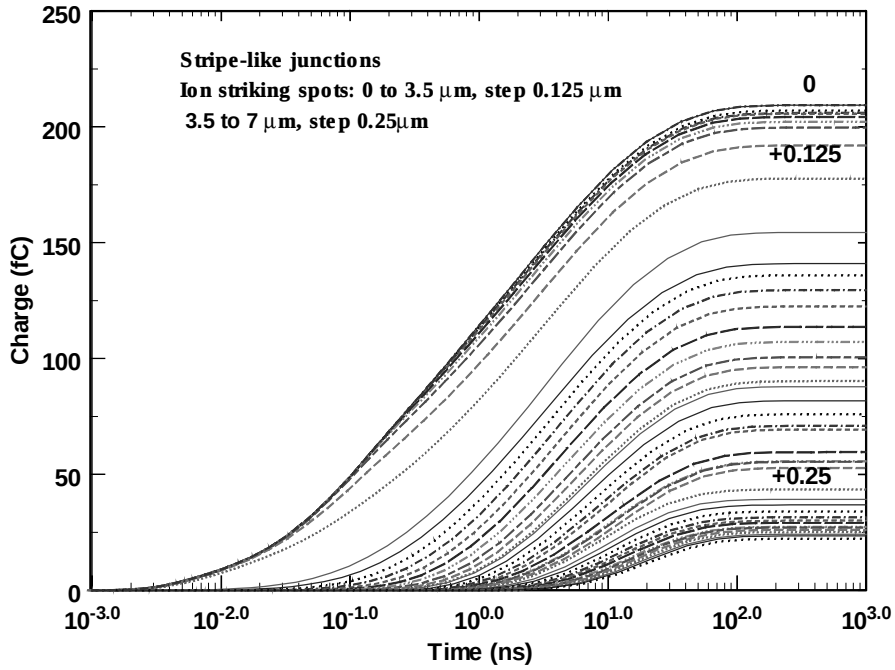

FIGURE 22-B

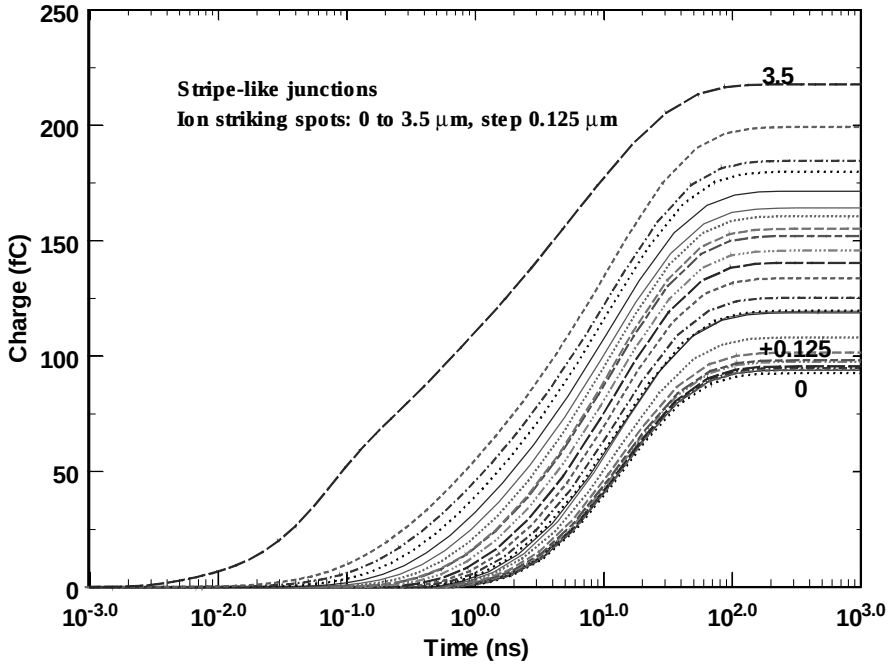

FIGURE 22-C

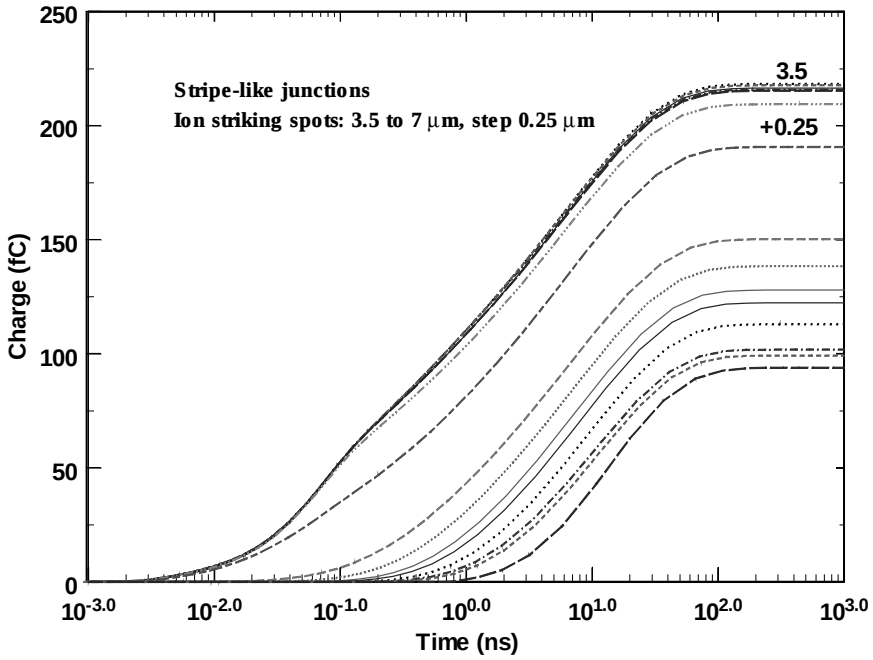

FIGURE 22. MEDICI simulation results for charge collection from stripe-like junctions. (A) Inner junction for ion strike spots from 0 to 3.5 μm, step 0.125 μm, 3.5 to 7 μm, step 0.25 μm. (B) Outer junction for ion strike spots from 0 to 3.5 μm, step 0.125 μm. (C) Outer junction for ion strike spots from 3.5 to 7 μm, step 0.25 μm. The middle of the inner junction is assumed to be origin.

FIGURE 23-A

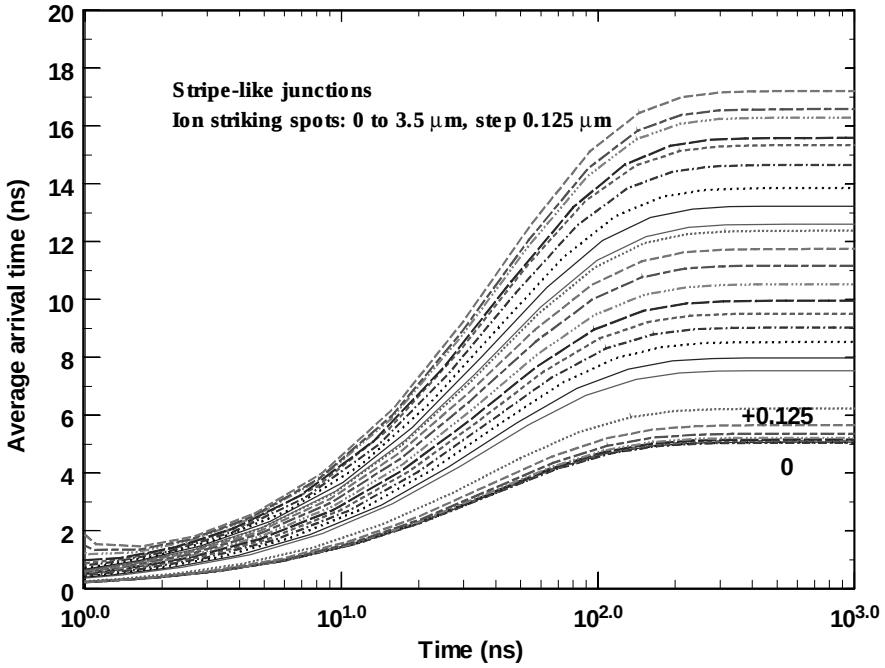

FIGURE 23-B

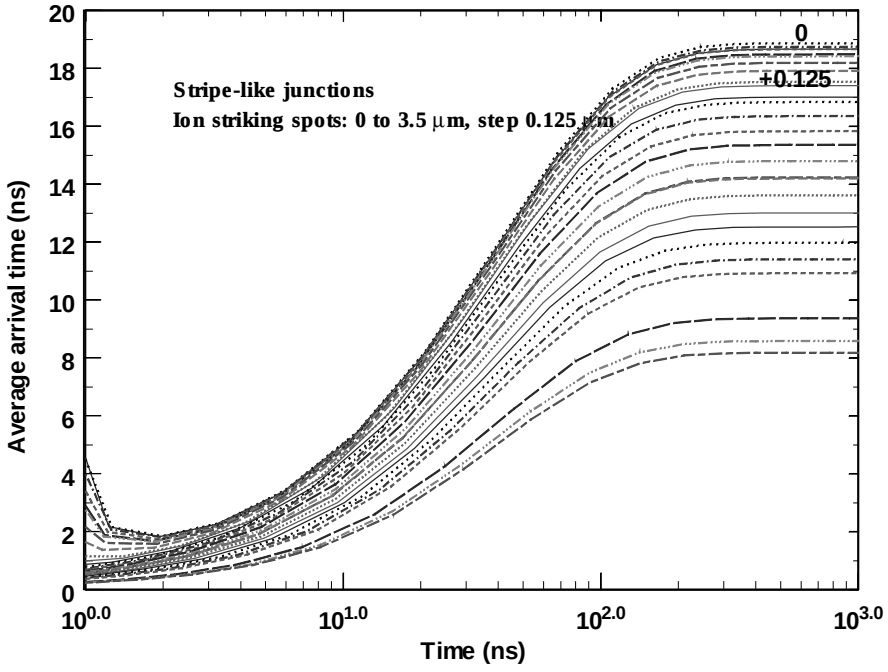

FIGURE 23. MEDICI simulation results for average arrival time from stripe-like junctions. (A) Inner junction for ion strike spots from 0 to 3.5 μm, step 0.125 μm. (B) Outer junction for ion strike spots from 0 to 3.5 μm, step 0.125 μm.

FIGURE 24-A

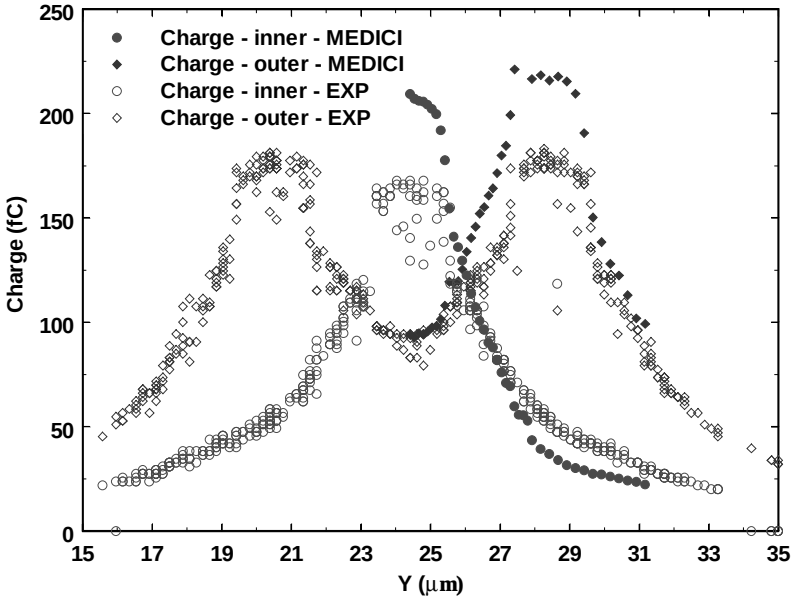

FIGURE 24-B

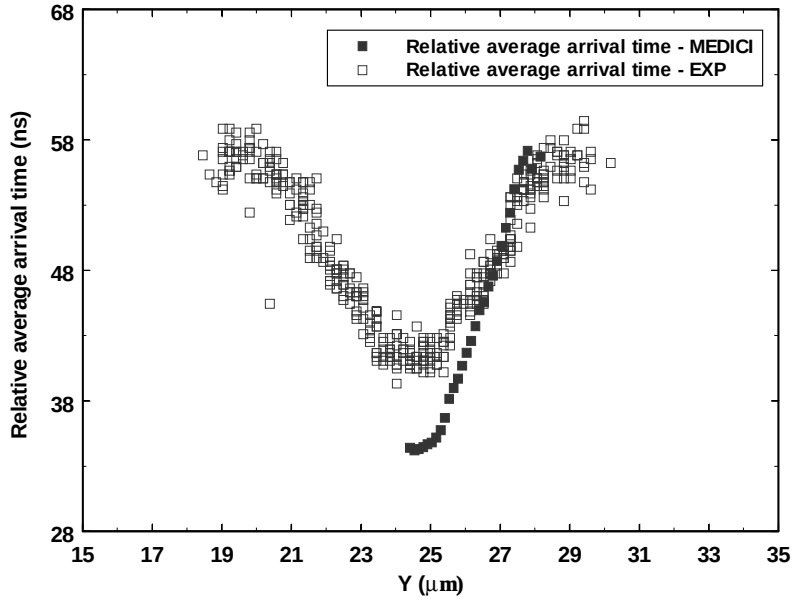

FIGURE 24-C

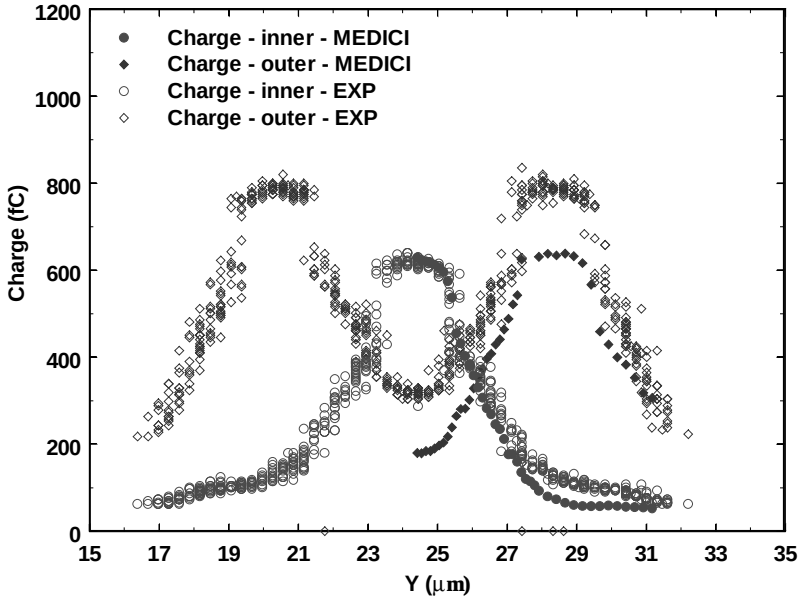

FIGURE 24-D

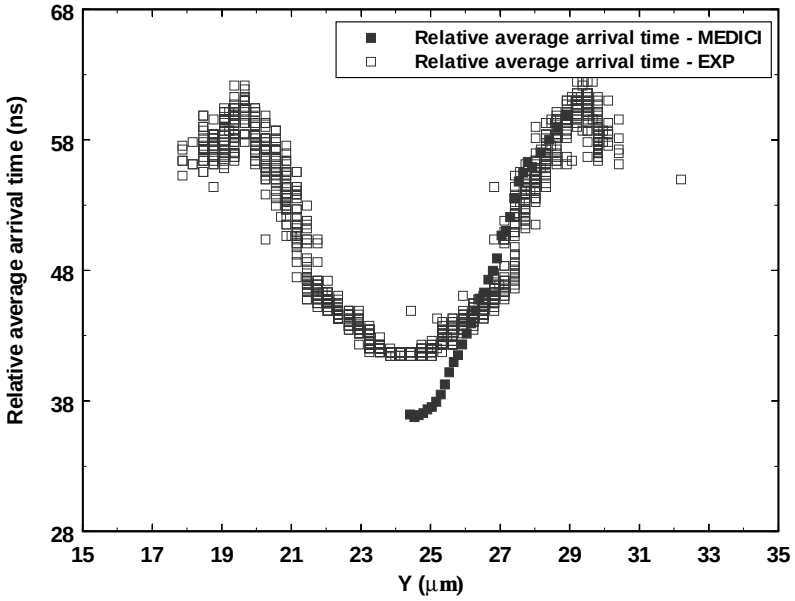

FIGURE 24. MEDICI simulation and experimental results. A and B are simulations and measurements using a 12 MeV carbon microbeam. C and D are results using a 28 MeV silicon microbeam.

CHAPTER 5

CONCLUSIONS

The continuing trend to scale down the size and operating voltages of circuits means higher susceptibility to natural radiation induced effects in semiconductor devices. The ionizing radiation can lead to the undesired generation and migration of charge within devices. The fundamental understanding of the dynamics of charge collection in electronic devices is essential to design more robust devices through the design and process modifications.

Simulation tools has been widely used to provide insight into the effects of ionizing radiation on devices. Ion Beam Induced Charge Collection (IBICC), Time Resolved IBICC (TRIBICC), and Diffusion Time Resolved (DTRIBICC) techniques can be used to experimentally study charge collection, transient charge collection, and diffusion time resolved charge collection from test structures. Experimental results can provide a basis for comparison with computer simulation tools to establish limitations, calibrate and validate simulation codes.

This research has focused on the study of charge collection dynamics on test structures using Ion Beam Induced Charge Collection (IBICC) techniques with microbeams. The test structures were provided by Texas Instruments Inc. The heavy-ion microbeams for this work were produced at the Ion Beam Materials Research Laboratory

(IBMRL) at Sandia National Laboratories. Carrier transport based on the drift-diffusion model is reviewed, and a 2D device simulation tool, the MEDICI code, is described and used to simulate the charge collection dynamics with test structures. The charge collection dynamics, especially funneling assisted charge collection, is reviewed based on recent theoretical work.

The IBICC measurements demonstrate the differential charge collection efficiency with the aid of the IC design information. The experimental results show the importance of diffused charge and charge sharing between adjacent junctions. Since Multiple Bit Upsets (MBUs) are extremely difficult to diagnose and correct, the charge sharing is especially significant to account for the MBUs in ICs. As the size of IC continues to shrink, MBU could be more serious challenge to design reliable devices in the future.

A new technique, DTRIBICC, is first proposed in this work to measure the average arrival time of the diffused charge, which can be related to the first moment (or the average time) of the arrival carrier density at the junction. The amount of charge collection and the magnitude of the average arrival time for diffused charge collection can be crucial to understanding and mitigating radiation induced circuit malfunctions during normal IC operations. The relative arrival time is measured on the highly symmetric stripe-like junctions along with the amount of collected charge using a multiple parameter data acquisition system. The MEDICI simulation is in qualitative and sometimes even quantitative agreement with the results from microbeam measurements. Lateral diffused charge collection increases the area of sensitive regions beyond the

junctions, and the average arrival time of the diffused charge may be used to define the effective sensitive regions during IC operations.

As the feature size of IC shrinks down to 0.25 μm, the high spatial resolution using microbeam technique is very difficult to achieve using magnetic or electrostatic focusing lenses. A new approach, Ion-Electron Emission Microscopy (IEEM), has been proposed to obtain such high resolution [158]. IEEM uses unfocused ion as a flood beam, the beam striking positions are obtained by projecting the Secondary Electrons (SEs) emitted from the sample surface as a result of ion striking using a Position Sensitive Detector (PSD). These position signals are coincidentally recorded with induced signals as they strike the sample.

IBICC, TRIBICC, and DTRIBICC techniques can be combined with IEEM technique to study charge collection dynamics within devices. Since IEEM uses unfocused ions as a flood beam, there are no special requirements of ions (such as ion species, energy spread, etc.). It is possible to use alpha particles emitted from radiation sources (such as ^{241}Am). Thus, compact test stations can be built for charge collection studies without accelerator facilities [159].

The SEs emitted from the sample surface as a result of ion striking can also be used as trigger signals as required by TRIBICC and DTRICC techniques, the transient charge collection and diffused time (absolute average arrival time) resolved charge collection can be measured from devices. During DTRIBICC timing measurement in the present work, the Constant Fraction Discriminators (CFDs, Ortec 583) are used. The CFD trigger threshold is about 40 fC. This high trigger threshold may limit the DTRIBICC technique to heavy ions with higher Linear Energy Transfer (LET).

However, if CFD can be optimized so that alpha particles emitted from radiation sources can produce trigger signals, DTRIBICC will be very useful to study diffused charge collection. DTRIBICC can also be used in the lateral mode, which can be used to directly measure carrier transport properties such as minority carrier mobility.

APPENDICES

APENDIX A

FOCUSED HEAVY ION NUCLEAR MICROPROBE (FHINM) FACILITY

A nuclear microprobe system can be used as a tool for many applications, such as semiconductor development [161,162], and structural and electrical characterization of semiconductor materials [163]. Ion beam analytical techniques at MeV energies, such as Particle Induced X-ray Emission (PIXE), Rutherford Backscattering Spectrometry (RBS), Nuclear Reaction Analysis (NRA), Elastic Recoil Detection Analysis (ERDA), and Ion Beam Induced Luminescence (IBIL), may also employ a focused microbeam. The focused microbeam can obtain spatially resolved information, which leads to techniques such as ion beam induced electron image, Ion Beam Induced Charge Collection (IBICC), Scanning Transmission Ion Microscopy (STIM), and Ion Micro-Tomography (IMT) [116].

A Focused Heavy Ion Nuclear Microprobe (FHINM) facility has been constructed at the University of North Texas (UNT). The microprobe facility mainly consists of an ion source, either a Source of Negative Ions by Cesium Sputtering (SNICS) or an Alphatross ion source, an NEC 3MV Pelletron tandem accelerator, bending magnets, various beam steering accessories, and microprobe beamline. The negative ions produced in the SNICS source or negative helium ions produced in the Alphatross source can be extracted from the source and injected into the low energy end of the accelerator after passing through the 30 and 90 degree magnets. After acceleration to the terminal, the negative ions are then converted to positive ions by stripping several electrons when they pass through gas or solid strippers in the terminal of the accelerator. Depending on the

various charge states produced, the positive ions gain different energies when they exit at the high-energy end of the accelerator. The high-energy ions in specific charge states can be selected for momentum/charge by the HVEC switching magnet and transmitted to different beam lines. FIGURE 25 is the Ion Beam Modification and Analysis Laboratory (IBMAL) layout. Two microbeam lines are shown in FIGURE 25, one is an apertured microbeam system, which was constructed in collaboration with Texas Instruments Inc. (TI), another is the recently built FHINM microbeam line. FIGURE 26 is the end stage of the apertured microprobe. FIGURE 27 is the photo of the focused microprobe beamline. In FIGURE 26 and FIGURE 27, major microbeam components are labeled.

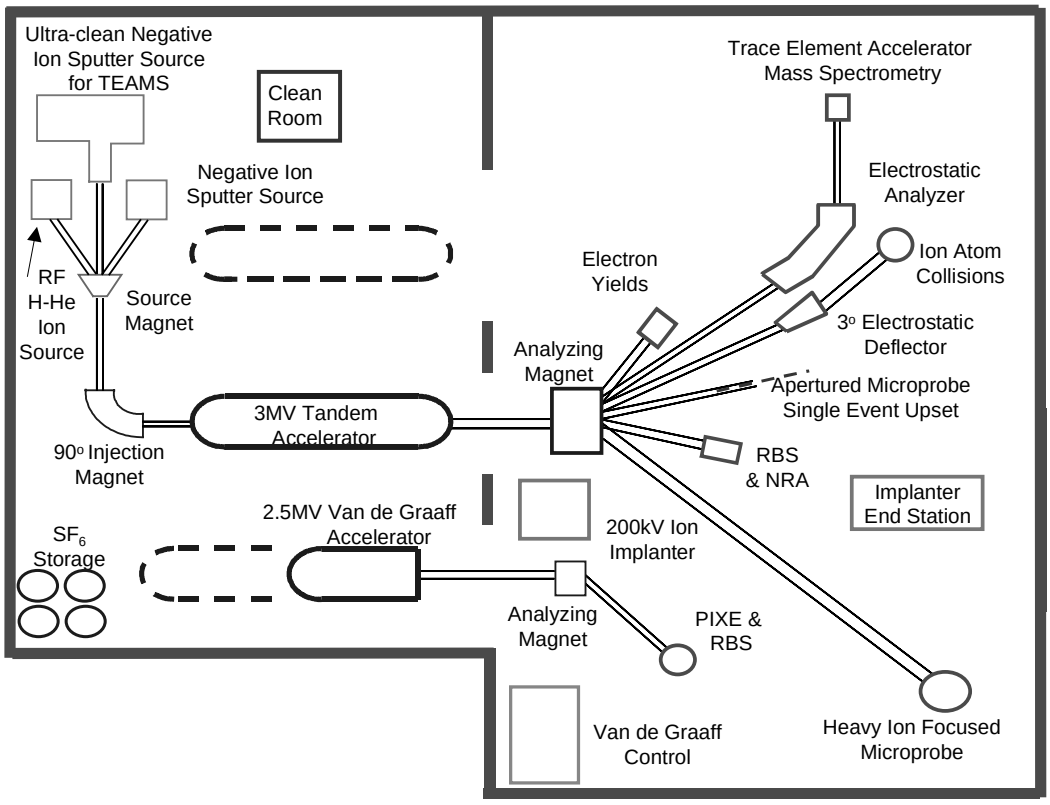

FIGURE 25. Ion Beam Modification and Analysis Laboratory (IBMAL) layout. Two microbeam systems are shown, one is the apertured microprobe system, and the other is the focused ion microprobe system.

Apertured Microbeam System

In FIGURE 26, the beam is collimated by the aperture. The aperture, mounted on a 3.8 cm long tube, is the final wall of a differential pumping system. The ions are extracted into the air to strike the interested regions of the Device Under Test (DUT), which is mounted on the X-Y-Z-ϕ stage. The computer-controlled stage can expose specific test regions to the apertured microbeam. A fast electrostatic blanking system is used to control the ion arrival time and number of ions striking the device structures. The number of ions can be controlled by the pulse width of the blanking system and the beam flux. Also, the blanking system eliminates any radiation exposure other than during the measurement cycle. Therefore, the apertured microbeam system ensures precise experimental control of the energy, arrival time, location, and angle of the ion strike. A number of internal reports and papers were published based on the experimental SEU and charge collection measurements on digital devices, such as prototype SRAM and DRAM memories, using the apertured microbeam system [59-61]. However, the size and quality of the apertured microbeam is deteriorated due to the scattering particles from the defining apertures as discussed in Chapter 1. The constructed focused ion microprobe facility at UNT is the recent effort to improve capabilities and enhance these SEU related studies.

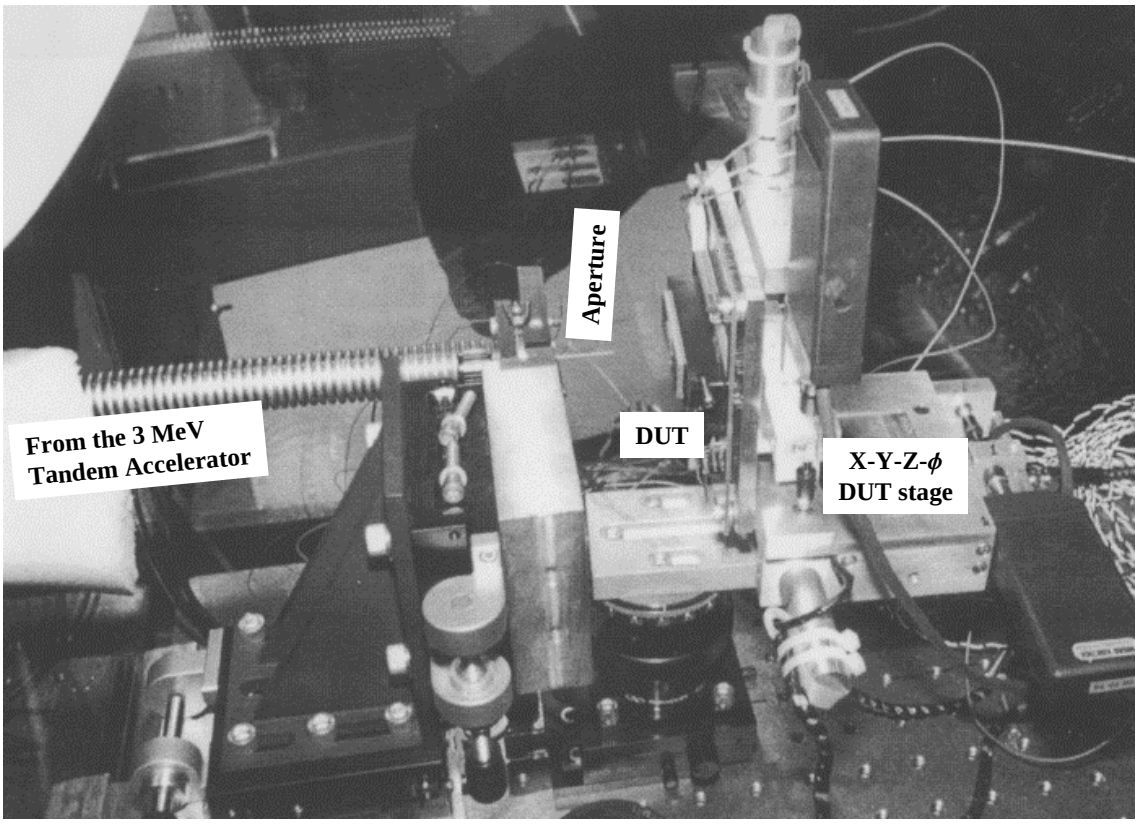

FIGURE 26. The apertured microprobe end stage at the IBMAL. The external microbeam is obtained through a differential pumping system (not shown). The beam is collimated by a pin-hole aperture. The Device Under Test (DUT) is installed in the X-Y-Z-ϕ DUT stage. The movement of the DUT stage can position the interested areas under the bombardment of the apertured microbeam.

Focused Microprobe System

Focused microprobe beamline

As shown in FIGURE 27, the main components of the focused ion microprobe beamline are an object box, an aperture box, two pairs of separated Russian magnetic quadrupole doublet lenses, scan coils (not shown), sample chamber with front and rear viewing microscopes. To minimize the effects of mechanical vibration, all of these components are mounted on a 7-meter long steel girder, which sits on two massive bases cushioned with heavy-duty vibration absorbers. Both object and aperture boxes are UHV compatible steel chambers to house all vacuum components needed at the entrance to the microprobe beam line and at the pre-lens point in the microprobe beam line, respectively. The boxes are of heavy construction to minimize the effects of vibration. They are of large internal dimensions to provide high pumping speed and to provide space for incorporation of diverse instrumentation. Both object and aperture boxes are equipped with diaphragm mounting plate, faraday cup, and quartz viewer (later replaced with Cr-doped Al_2O_3, strong luminescent materials). Since the Cr-doped Al_2O_3 can release reddish luminescent light with beam bombardment, it is suitable for CCD cameras (very sensitive to red light) to monitor and optimize the beam spot. The boxes have space for future incorporation of micro-slits and other devices. Two sets of individually replaceable precision diaphragms (diameters range from 5 to 600 μm) are mounted in both the object and aperture plates, respectively. The object or aperture plates can be adjusted using the precision X-Y manipulators, which ensures that the beam passes through or to align the beam with the centers of selected diaphragms.

The microprobe focusing lens system consists of two separated Russian magnetic quadrupole doublet lenses, their alignment supports, two sets of precision rails and trolleys on heavy steel base plates, a power supply and a high precision lens current controller with a precision Digital Voltage Meter (DVM) readout. The pole pieces of the lenses are driven in place and clamped between heavy corner pieces to complete the symmetrical yoke. The lenses are mounted on X-Y precision alignment supports, which are mounted on the trolleys to adjust the position from the specimen chamber along the Z direction to change focusing conditions. FIGURE 28 is the first order focused ion optics with ~60 symmetric demagnification factor through the focusing lens system. The parameters of the focusing lens system are provided in TABLE 2. The separated Russian quadruplets provide a large and symmetric demagnification factor so that the critical object collimator can be relative large and therefore with less aperture scattering. The lens system with ~60 times demagnification has the ability to focus proton, alpha particle, and heavier ions down to a spot size of ~ 1 μm. To minimize effects due to the external magnetic field, the beam tube is wrapped with μ-metal.

FIGURE 29 is the focused microprobe schematic diagram. A high precision digitally stabilized and computer-controlled current supply is used to provide the two independent lens currents required by the two Russian quadruplets. The lens currents can be adjusted to focus the beam through average value and ratio of the two lens currents, which allow the size and the shape of the beam spot to be optimized independently.

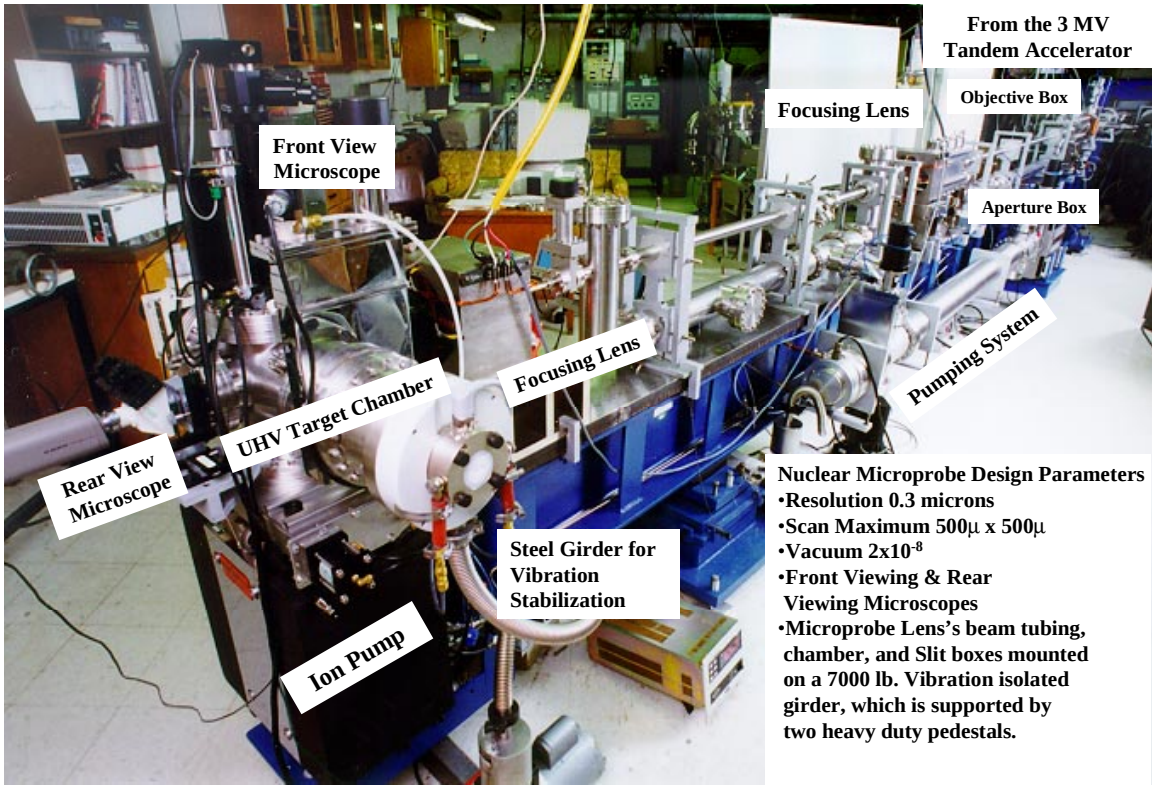

FIGURE 27. The color photo of the nuclear microprobe beamline at the University of North Texas (UNT). The labeled major components in the picture are object and aperture boxes, a pair of quadrupole doublet with Russian configuration, front and rear viewing microscopes, UHV target chamber, and pumping system. All components are mounted on the 7 meter long girder with massive bases cushioned with heavy-duty vibration absorbers. The scanning coil is located between the target chamber and second set focusing lens (not shown in the picture).

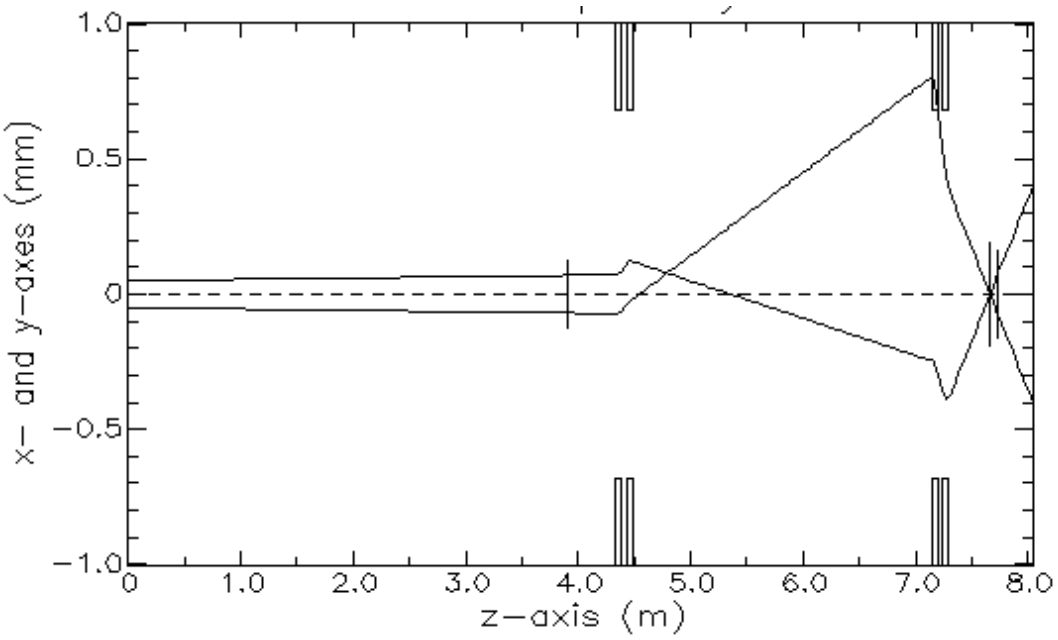

FIGURE 28. The first order focused ion optics using the separated Russian quadrupole doublet (demagnification factor Dx=Dy=60).

Object to aperture	3.83 m
Aperture to Q1	0.48 m
Q2 to Q3	2.61 m
Q4 to sample (image plane)	0.34 m
Pole length of each lens	57 mm
Spacing Q1 to Q2 and Q3 to Q4	40 mm
Turns per pole in Q1 and Q4	125
Turns per pole in Q2 and Q3	108
Bore radius of all lens	6.35 mm
Demagnification factor	Dx=Dy=60
Maximum magnetic rigidity	12 amu.MeV/q2

TABLE 2. Specification of the focused microprobe. Q1, Q2, Q3 and Q4 are the quadrupole lenses of the separated Russian quadruplet downstream.

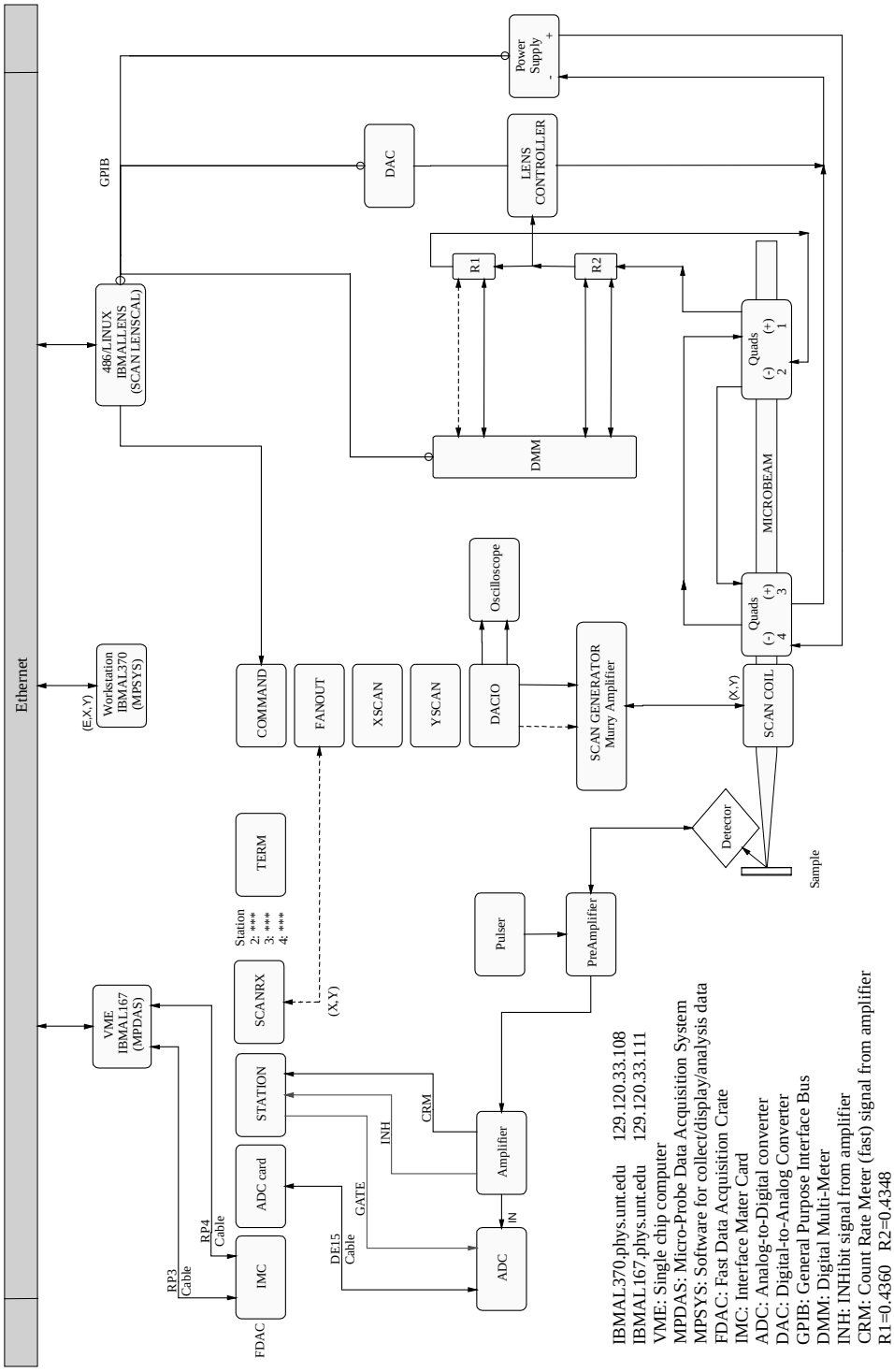

FIGURE 29. IBMAL microprobe facility system schematic diagram.

The programmable digital beam scan system is comprised of a ferrite cored set of post lens X-Y deflection coils, a dual trans-conductance amplifier, and a digital scan generator. The ferrite cored deflection coils are ~70 mm in total length. All of these are under scanning control from a scan controller through a General Purpose Interface Board (GPIB). The scan controller accepts the scanning parameters from a 486-computer running LINUX. This computer is also used to control the lens current supply. The coils are tapped to enable accuracy with ultra small scans. A dual fast wide band trans-conductance amplifier provides the currents needed to power the deflection coils. The amplifier gives independent X and Y scans and offset currents over a frequency range of 0 to 10 kHz for large pixel scans. The maximum scan frequency is limited by the 2 μs delay in the amplifier. The digital scan generator is a variable frequency, dual, digital scan generator with an addressable field of 4096 x 4096 pixels. It employs two wide band (0 to 5 MHz) voltage to frequency converters, giving step frequencies up to 5 MHz and line frequencies of 1.25 kHz with 4096 digital resolution. The scan system also supplies digital scanning position signals to the fast data acquisition crate and has an analog output for monitoring by an oscilloscope.

A rear-viewing zoom microscope (40-200 variable magnification) is used to observe the light emission as the ion beam strikes the CsI or quartz crystals. The beam can be initially focused by adjusting the current supplies to the quadruplet. To achieve the highest resolution, the beam is first focused with the help of the rear optical microscope with large current, and large object and aperture diaphragms, and then the object and aperture diaphragms are reduced in size. The final beam focusing is completed using a front viewing microscope (300 magnification). The adopted front viewing microscope

has an annular aperture to allow the focused microbeam through and strike the sample. The ring shape illumination light of the front viewing microscope can illuminate the sample surface. The built-in prisms of the microscope will transmit reflected light from the sample surface to the viewer or a Charge Coupled Device (CCD) camera. Compared with the features of sample surface and the images extracted from the collected data, the precise beam striking spots can be located. The STIM (Scanning Transmission Ion Microscopy) image from a pin diode with TEM grid on top can be used to locate and evaluate the beam. A Si (Li) X-ray detector may be mounted in the chamber. For the IBICC (Ion Beam Induced Charge Collection) measurement, the sample itself is the detector. A sample holder is mounted on a X-Y-Z-ϕ manipulator, which ensure that the sample can be accurately positioned on the same focusing plane with the aid of the front viewing microscope.

Data acquisition system

A VersaModule Eurocard (VME) based data acquisition computer system acts as the central control hub for all of the real time functions in the multi-parameter data collection system of the nuclear microprobe. The following modular components are mounted in a VME chassis: a high performance DR11W-VME card, a single-board CPU with 16MB DRAM, integrated Small Computer System Interface (SCSI), and Ethernet support with VXWORKS operating system. The VME system collects data from the Fast Data Acquisition Crate (FDAC), presorts it, and passes it rapidly via the Ethernet to a dedicated Reduced Instruction Set Computer (RISC) workstation for analysis. The VME system has a VXWORKS operating system and is booted up and controlled from a

dedicated RISC workstation running UNIX via Ethernet. The adopted RISC workstation, RISC6000/POWERserver 370, runs the X-Windows graphics programs. The RISC workstation is used as the host to collect, display and analyze the data.

Fast Data Acquisition Crate (FDAC) system program runs under "UNIX-like" real time operating system VXWORKS in a VME computer. It is designed to handle event by event data from multiple stations (scan generator and multiple, independent ADCs), collecting the data from a fast data acquisition crate and, if required, processing the data before passing the data on for analysis. The user can interface to the total system via software on the workstation. All commands and data sent to or from the RISC workstation go via Ethernet. The FDAC can collect scanning data (E,X,Y) from up to four independent detection channels. Each detection channel can collect data at up to 10,000 events/s simultaneously, or very high speed collections of data from any one channel at up to 40,000 events/s. Once the data are in the VME memory, the software performs all the necessary preprocessing of the data that is then recorded on a disk.

The generalized data handling and control system program, MicroProbe SYStem (MPSYS), is a multi-parameter data acquisition, display, and analysis program for multi-dimensional data from the microprobe. Data are collected in event mode (E,X,Y) and stored in real time sequence. Maintaining the real time sequence permits the study of target deterioration as a function of time. The MPSYS program is modularized and written in a macro language. New function modules may be easily added. The program runs under UNIX and X-Window graphics system. It incorporates cooperative multiprocessing for flexibility and expandability. The MPSYS contains general

commands, data object commands, data acquisition demands, window commands, spectrum and manipulation commands, and mapping commands.

The MPSYS has control of the FDAC through the high-speed Direct Memory Access (DMA) interface in the VME crate, which is connected to the FDAC via the Ethernet. It can display the histogram of individual spectra as data is being collected. It can also set windows in these spectra, set markers, expand or contract a displayed spectrum to observe peaks of interest, calibrate the X axis to represent physical units such as energy. The interactive display of multiple 2D-color pixel maps of any user selectable range of interest can subtract background, bind adjacent pixels, adjust colors etc.

During the experimental measurements, care should be excised to establish correct timing sequence between the measured and control signals. The timing sequence can be reset within MPSYS, and the oscilloscope is especially useful for such task.

FHINM facility testing results

Some preliminary testing results on TEM grids with STIM technique are presented as following. FIGURE 30 is the charge collection from a pin diode (S1223) with 400 Au TEM mesh, the ion beam is 2 MeV H^+. In FIGURE 30, the energy (or collected charge) spectrum is shown. Also, the images for energy windows in the ranges of 100-300, 300-380, 380-450, and whole spectra are provided with an intensity legend. Since the 2 MeV H^+ can penetrate through the mesh bar, there are two peaks in the energy spectrum. The high-energy peak corresponds to ions passing through the holes of the mesh, and the low energy peak corresponds to the ions passing through the bars of the mesh. Since the beam scanning area is the pin diode edge, the charge collection clearly

reveals that active area of the pin diode (on the left side shown in the images) and inactive area (on the right side shown in the images). In the images of 100-300 and 300-380, the vertical band corresponds to the metallization line on the top of the pin diode.

FIGURE 31 is STIM image from pin diode (S1223) with 1000 Cu TEM mesh (bar 9 μm wide, hole 16 μm on a side), the ion beam is 4 MeV C^{3+}. In FIGURE 31, the energy (or collected charge) spectrum is shown. Also, the median image is provided with a intensity legend. There is a significant difference shown in the energy spectra between FIGURE 30 and FIGURE 31. Since the 4 MeV C^{3+} ions can not penetrate through the bars of the mesh, there is only one peak on the energy spectrum shown in the FIGURE 31. Also, the ion induced damage is more severe for the carbon ions than that for protons. During the data collection process, one can observe the energy spectrum is boarding toward low energy. It is an indication that the charge collection efficiency is decreasing with increasing dose. Also, from the median image shown for FIGURE 31, it is inferred that the ion beam spot size is about ~3 microns in this preliminary measurement. Further improvement of the system alignment and stability will be required to deliver beam with submicron spatial resolution and higher beam quality for the future SEU research.

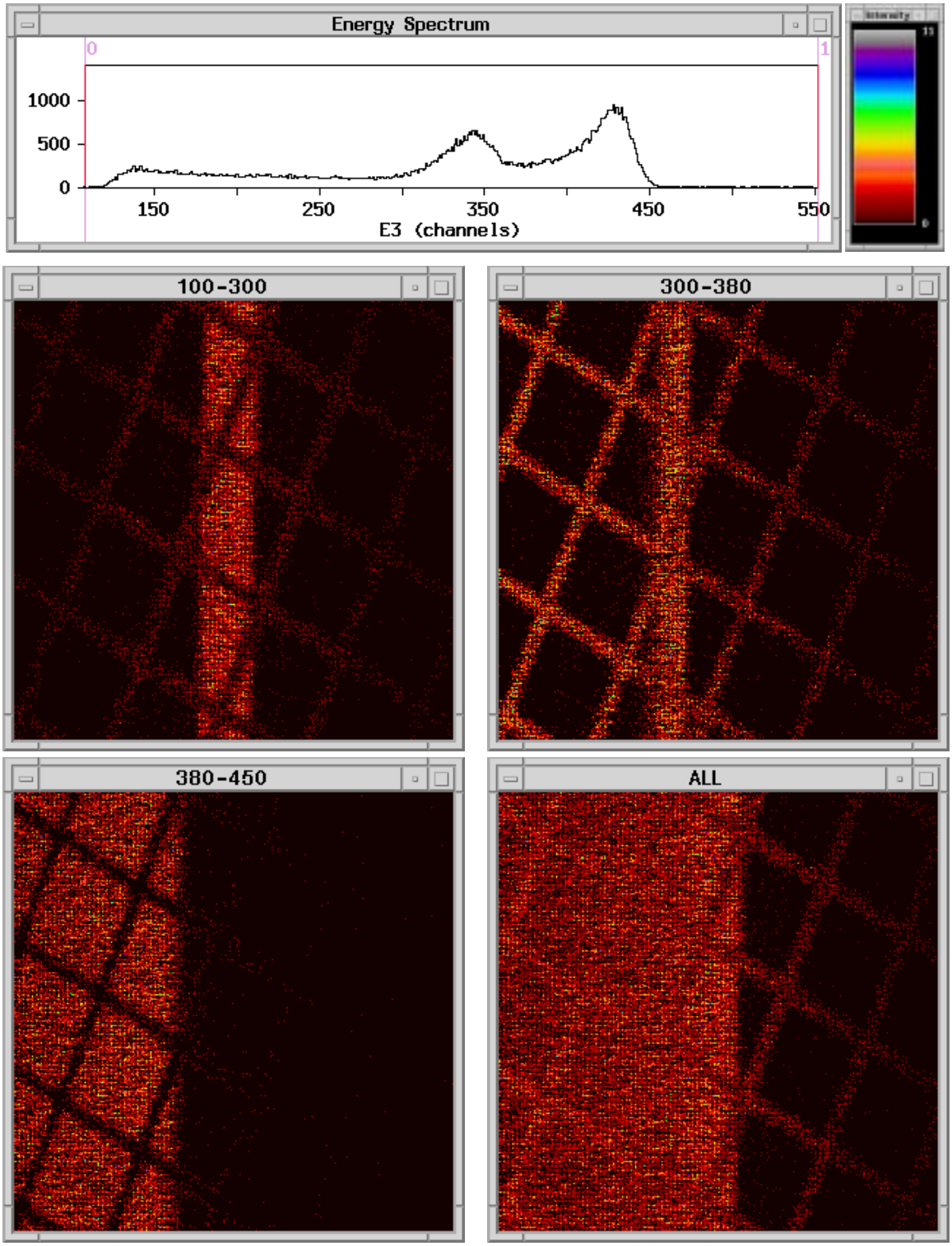

FIGURE 30. STIM image (in color) with a 2 MeV H^+ beam, sample is 400 Au TEM mesh and pin diode (S1223). The energy (or collected charge) spectrum and the images for energy windows in the ranges of 100-300, 300-380, 380-450, and whole spectrum with intensity legend are shown.

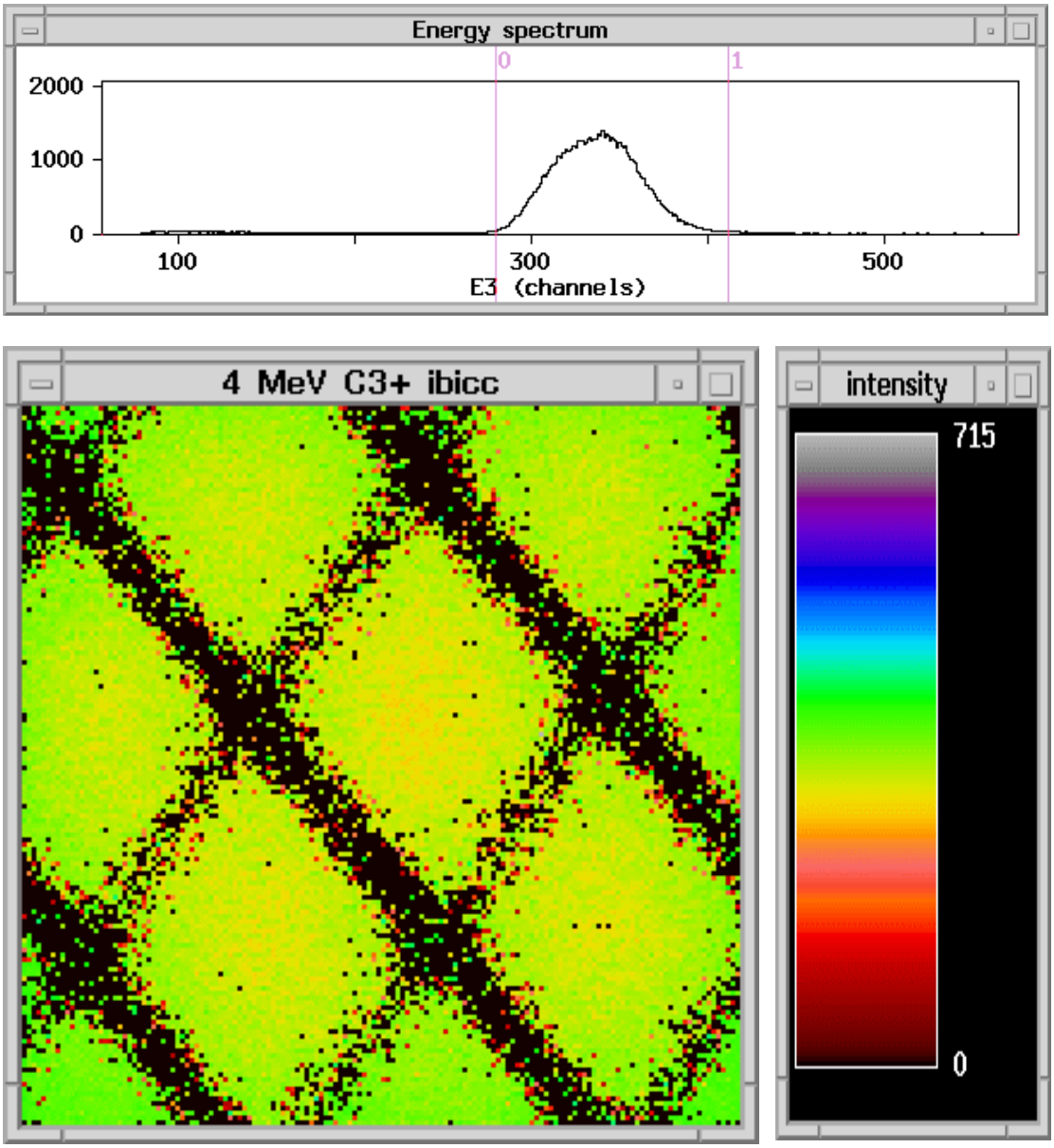

FIGURE 31. STIM median image (in color) with a 4 MeV C^{3+} beam, the sample is 1000 Cu TEM mesh (bar 9 μm wide, hole 16 μm on a side), and pin diode (S1223). The ion beam spot size is inferred to be about ~3 microns in this preliminary result.

APENDIX B

MEDICI SIMULATION CODES FOR JUNCTIONS

MEDICI is a 2D-device simulator, which can be used study steady state or time dependent injection of electrons and holes. In this work, a table of LET (Linear Energy Transfer) in pC/μm is read from a formatted file based on calculation with SRIM96 to represent the length dependence of the electron-hole pair generation along the incident ion track. The following example codes are used to solve the ion induced electron-hole pairs by a 12 MeV carbon ion in cylindrical coordinates. The junction sizes are varied from 0.5 to 4 μm with step of 0.5 μm. Some important parameters discussed in Chapter 2 are defined in TABLE 3.

Simulate structure	Disc junctions (variable radius)
Junction size (radius)	0.5 to 4 μm with step of 0.5 μm
Junction reversed biases	0.5 to 4.5 V with step of 0.5 V
Coordinate	Quasi-3D cylindrical (r,z)
Doping profiles	See FIGURE 32
Models	CCSMOB, FLDMOB, CONSRH, AUGER, BGN
LET (pC/μm)	12 MeV Carbon LET (SRIM96)
Ion track parameters	T_0=3.0x10^{-12} s T_C=1.5x10^{-12} s DCHR=0.2 μm

TABLE 3. MEDICI simulation parameters for the disc junctions (variable radius).

MEDICI Codes for n+/p Junction

```
TITLE     AVANT! MEDICI - IBICC SIMULATION WITH N+/P JUNCTION
COMMENT   DEFINE A NON-UNIFORM MESH USING CYLINDRICAL COORDINATES
+         (THE X-DIRECTION CORRESPONDS TO THE RADIAL DIRECTION).
+         PUT THE FINEST GRID ALONG THE R=0 COLUMN AND AT THE
+         JUNCTION. N+/P, CARBON 12 MeV IONS.
+         SIZES OF JUNCTIONS 0.5 TO 4 MICRONS
+         TOP PASSIVATION LAYER 2.2 MICRONS
+         REVERSED BIAS 4 V
+         DOPING PROFILES PROVIDED BY TEXAS INSTRUMENTS

LOOP STEPS=8
ASSIGN    NAME=TOPLAYER N.VAL=2.2
ASSIGN    NAME=REVERSED N.VAL=4
ASSIGN    NAME=RID C.VAL=00 DEL=5
ASSIGN    NAME=RADIUS N.VAL=0.5 DEL=0.5

MESH      CYLINDRI
X.MESH    WIDTH=5.0  H1=0.02  H2=0.25
Y.MESH    N=1 L=0
Y.MESH    N=2 L=@TOPLAYER
Y.MESH    DEPTH=15-@TOPLAYER  H1=0.05 H2=0.5

REGION    NAME=SILICON   SILICON Y.MIN=@TOPLAYER
REGION    NAME=PASSIVATION OXIDE Y.MAX=@TOPLAYER

COMMENT   ELECTRODES
ELECTRO   NAME=COLLECTOR X.MAX=@RADIUS Y.MIN=@TOPLAYER-0.1
Y.MAX=@TOPLAYER
ELECTRO   NAME=SUBSTRATE  BOTTOM

COMMENT   PROFILES FOR N+/P, TI DATA FILE - NMOSDOPING
PROFILE   Y.MIN=@TOPLAYER Y.MAX=10+@TOPLAYER IN.FILE=NMOSDOPING
+         1D.ASCII Y.COLUMN=1 Y.OFF=@TOPLAYER IMPURITY=B D.COLUMN=3
+         OUT.FILE=JUNCDOPING
PROFILE   Y.MIN=@TOPLAYER Y.MAX=10+@TOPLAYER IN.FILE=NMOSDOPING
+         1D.ASCII Y.COLUMN=1 Y.OFF=@TOPLAYER
IMPURITY=P D.COLUMN=4
+         X.MAX=@RADIUS X.CHAR=0.1
PROFILE   Y.MIN=@TOPLAYER Y.MAX=10+@TOPLAYER IN.FILE=NMOSDOPING
+         1D.ASCII Y.COLUMN=1 Y.OFF=@TOPLAYER IMPURITY=AS D.COLUMN=5
+         X.MAX=@RADIUS X.CHAR=0.1
PROFILE   Y.MIN=10+@TOPLAYER UNIFORM P-TYPE  N.PEAK=7.61E15

COMMENT   GRID REFINEMENT BASED ON DOPING
REGRID    DOPING  LOG  RATIO=0.5  SMOOTH=1 IN.FILE=JUNCDOPING
+         IGNORE=PASSIVATION

COMMENT   SPECIFY PHYSICAL MODELS TO USE
MODELS    CCSMOB  FLDMOB  CONSRH  AUGER  BGN
```

```
COMMENT   CALCUATE A STEADY STATE SOLUTION REVERSED BIAS.
+         PERFORM A ZERO CARRIER SOLUTION AS AN INITIAL GUESS.
SYMBOL    NEWTON CARR=0
METHOD    DAMPED
SOLVE     V(COLLECTOR)=@REVERSED

COMMENT   GRID REFINEMENT BASED ON POTENTIAL
REGRID    POTEN RATION=0.2 MAX=1 Y.MIN=@TOPLAYER SMOOTH=1
+         IN.FILE=JUNCDOPING
SAVE      MESH OUT.FILE="JUNC_TOP_MS"@RID"" W.MODELS

COMMENT   FULL TWO CARRIERS SOLUTION WITH TIME=0, AND REVERSED BIAS
SYMBOL    NEWTON  CARRIERS=2
SOLVE     OUT.FILE="J_SOL_EH"@RID""

COMMENT   INDUCED ELECTON-HOLE CARRIERS BY 12 MeV CARBON IONS
+         IGNORE THE PASSIVATION LAYER
PHOTOGEN  X.START=0  X.END=0  Y.START=0 Y.END=10.5885 DCHR=0.2
+         T0=3.0E-12  TC=1.5E-12  LETFILE=C12MeVLET  PC.UNITS  GAUSS
+         Y.MIN=@TOPLAYER

LOG       OUT.FILE="DIO_C12_LOG_MS"@RID""

COMMENT   SIMULATE THE 2 MICROSECOND OF TRANSIENT RESPONSE
SYMBOL    NEWTON CARRIERS=2
SOLVE     TSTEP=0.5E-12  TSTOP=2E-6  OUT.FILE="DIO_C12_V"@RID"MS01"

L.END
```

MEDICI Simulation Results

FIGURE 32 are the junction doping profiles. Phosphorus and arensic are used to form *n*+, the boron doped p-substrate has a *p*+ retrograde boron well. During MEDICI simulations, the p+ well is assumed to be extended radially through the simulation mesh. FIGURE 33 is transient current responses for different junction sizes. The transient electron, hole, displacement currents are an indication of the neutralization of depletion regions (DR). At the moment t~0.5 ns, the DR recovered, and minority carriers (electrons in this case) are collected by the junction through diffusion. The smaller junction size and the larger transient currents also indicate that the smaller area junction can be much more easily disturbed by incident ions and led to the funneling process. FIGURE 34 is voltage drops along the central lines of the ion track at various moments immediately following the ion striking for junction with radius 0.5 μm. The voltage includes the built in potential. At t~11 ps, the voltage drops previously on the DR is now on the substrate due to the partial collapsed DR. At t~0.5 ns, the DR recovered from the collapse and holds most of the potential, which is an indication of the end of the funneling process. FIGURE 35 is the concentration distributions of holes and electrons at t=6.75 ps. The partially collapsed DR leads to the voltage drops on the substrate. Potential contour lines separated in 0.5 V steps form the “funnel” shape. FIGURE 36 are several carrier distributions along the central lines of the ion track at t=6.75 ps (A), 63.7 ps (B), 0.56 ns (C), and 6.94 ns (D) for junctions with a radius of 0.5 μm. FIGURE 36-A shows the initial collapse of the junction due to excess electron-hole pairs. FIGURE 36-B shows the recovery of the junction, holes are pushed down and electrons are moving up. FIGURE 36-C and -D

shows recovered junction, electrons continuously move up. The concentration variations in FIGURE 36 along the ion track also show the radial diffusion of carriers. FIGURE 37 shows MEDICI simulation results for charge collection (A) and average arrival time (B) for junctions with different radii. In FIGURE 37-A, the charge collection shows the smaller size junction can easily lead to funneling assisted charge collection compared with the larger size junction. However, the larger size junction can collect more charge through diffusion as the dissipation of the ion track. It therefore takes much longer for charge to be collected by the larger size junction through diffusion (FIGURE 37-B).

FIGURE 38 shows MEDICI simulation results for charge collection (A) and average arrival time (B) for junctions with different reversed biases (0 to 4.5 V in steps of 0.5 V). The junction radius is 1.0 μm. As shown in FIGURE 38-A, the funneling assisted charge collection is much faster and more pronounced as the reversed biases increased. At later stages when diffusion is more dominate, the charge collection is not very much dependent on the reversed biases applied to the junction (FIGURE 38-A). Therefore, the average arrival time for the diffused charge collection is not dependent on the reversed biases (FIGURE 38-B).

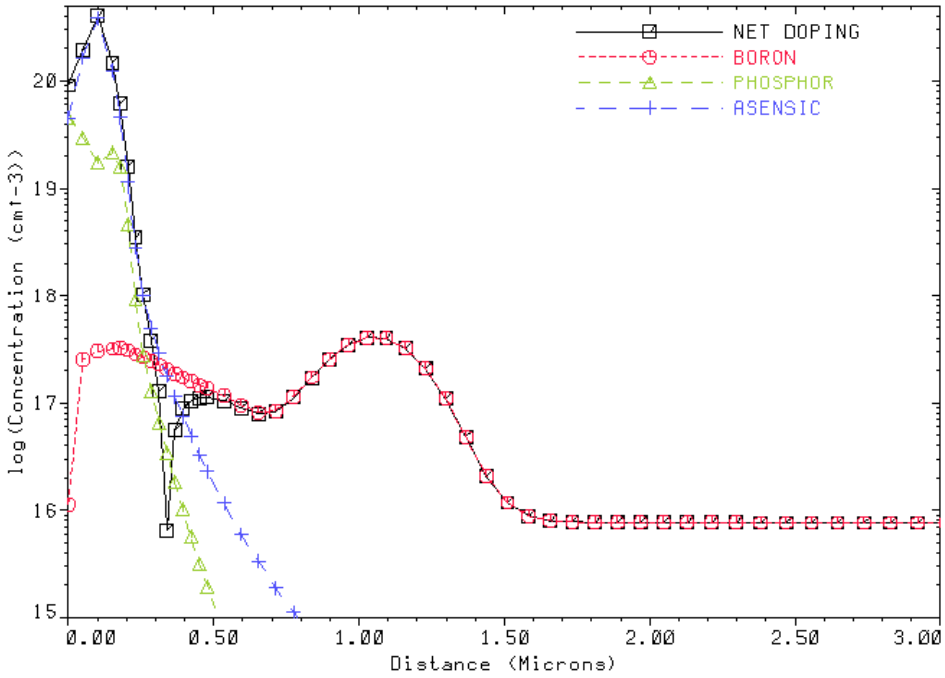

FIGURE 32. Junction doping profiles, Phosphorus and arsenic are used to form *n*+. The substrate has a *p*+ retrograde boron well. In the MEDICI simulations, the *p*+ doping is extended radially through simulation mesh.

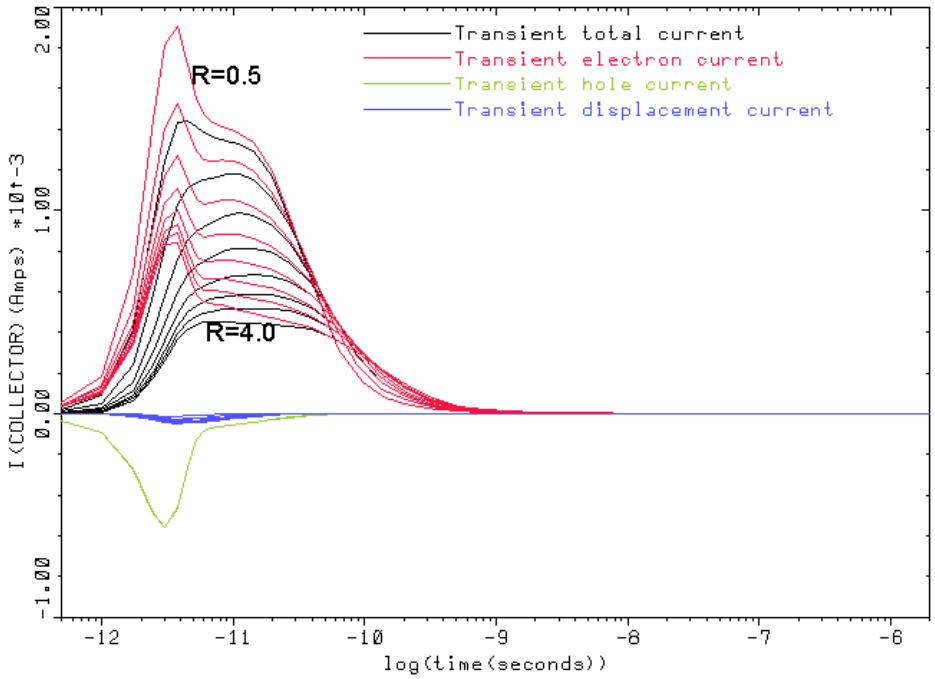

FIGURE 33. Variation of junction transient currents (total currents, electron currents, hole currents, and displacement currents) for different junction sizes (0.5 μm to 4 μm in steps 0.5 μm) (in color).

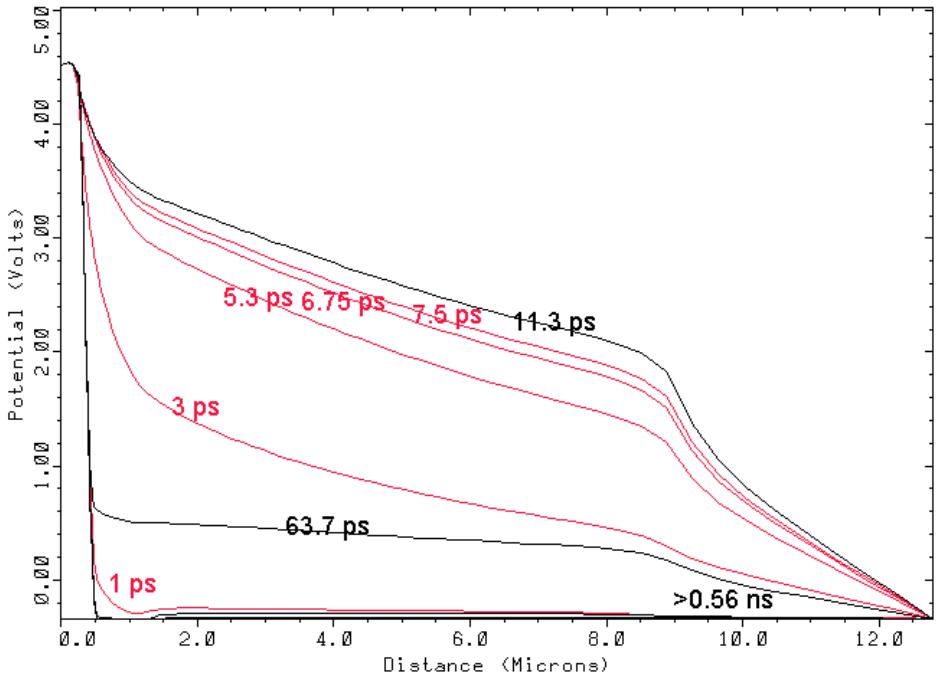

FIGURE 34. Voltage drops along the central lines of the ion track at various times (junction radius 0.5 μm).

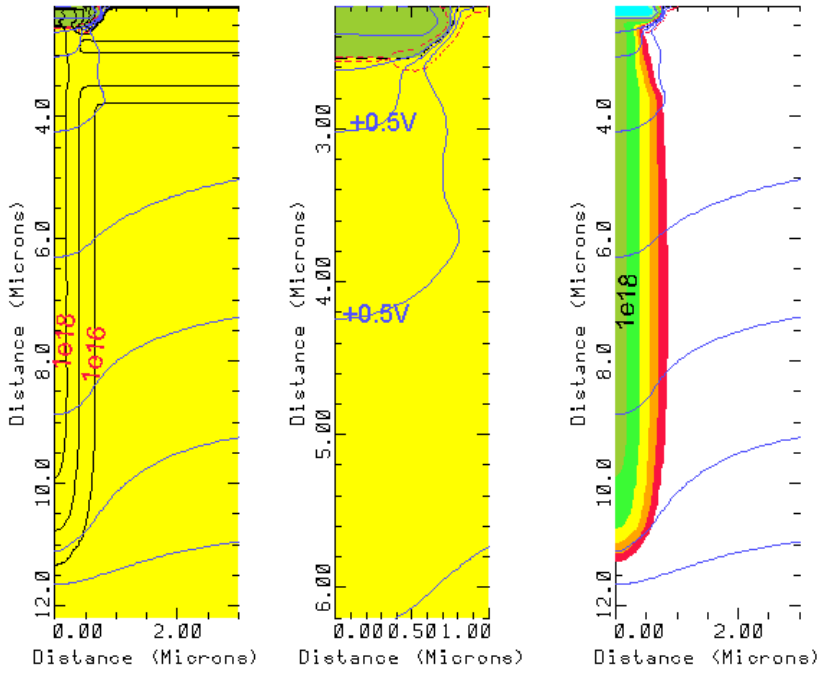

FIGURE 35. The concentration distributions of holes and electrons (junction radius 0.5 μm) (in color) at t=6.75 ps with potential contours (step 0.5 V). Also, the partial collapsed junction demonstrated the occurrence of the funneling effect.

FIGURE 36-A

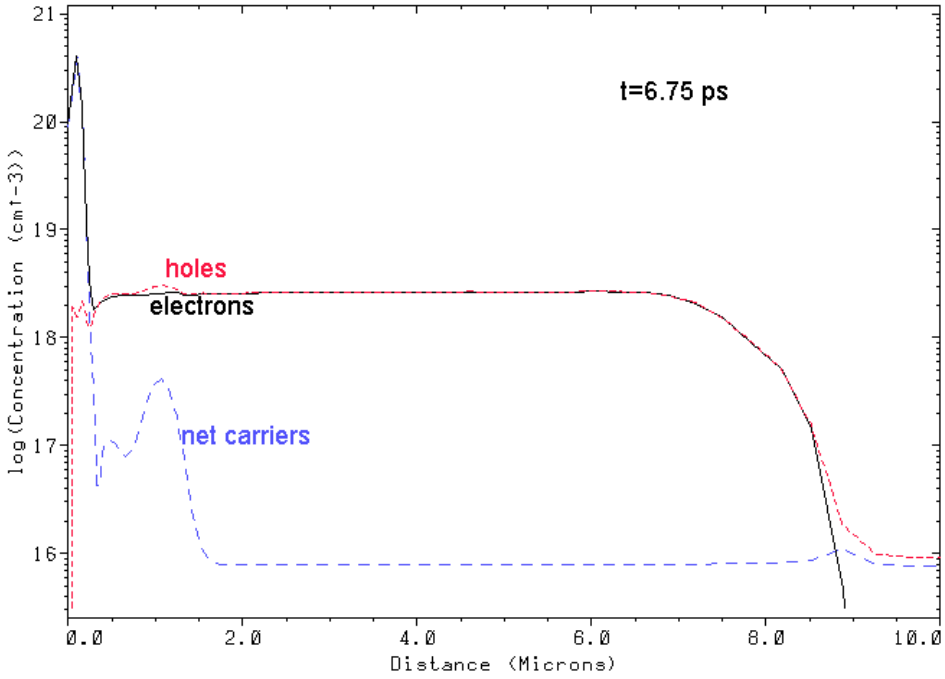

FIGURE 36-B

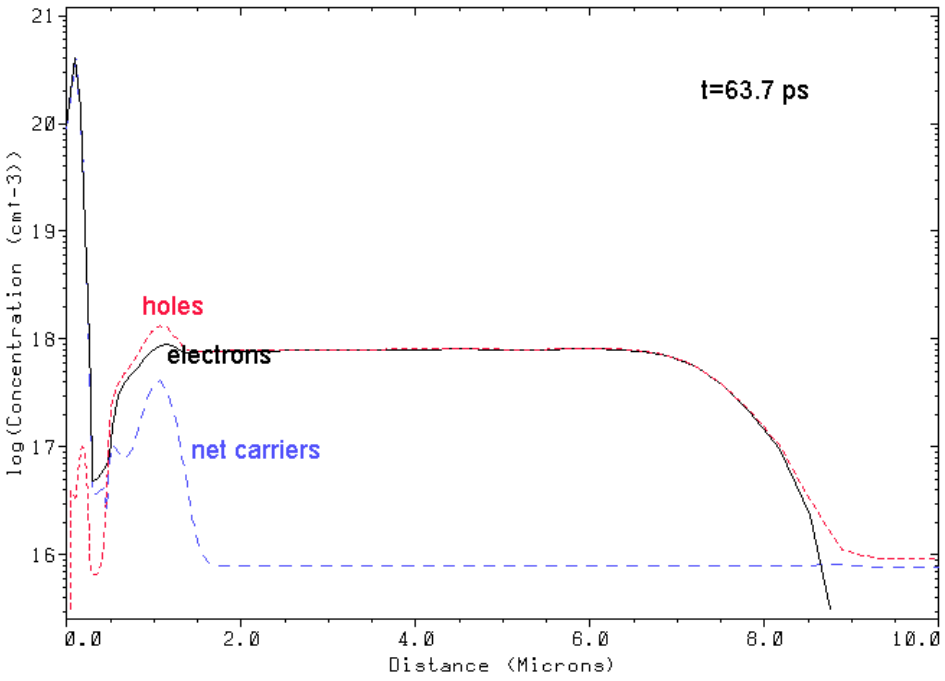

FIGURE 36-C

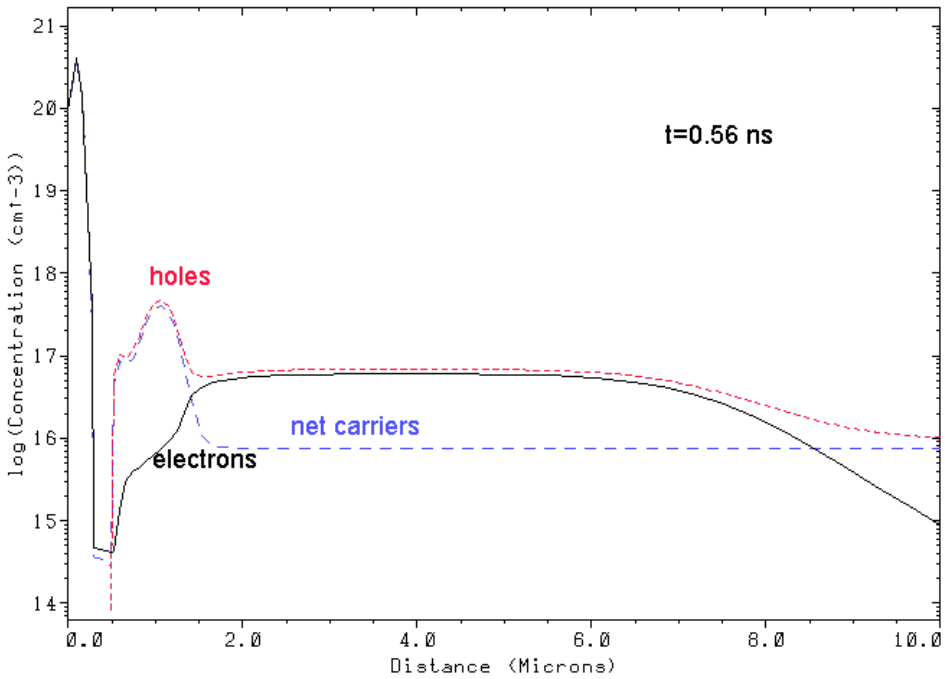

FIGURE 36-D

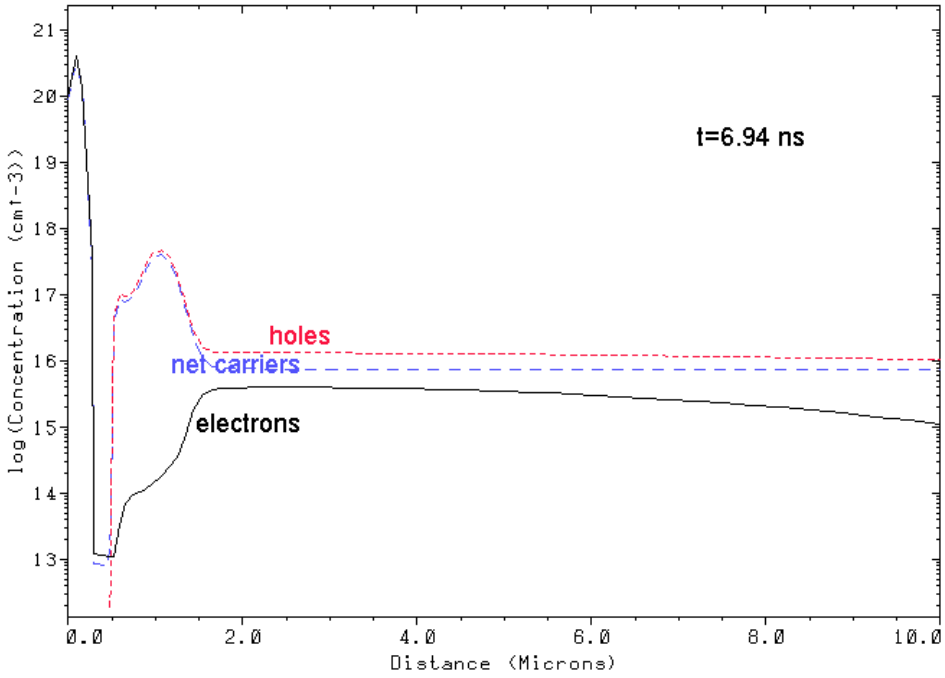

FIGURE 36. Charge distributions along the central lines of the ion track at t=6.75 ps (A), 63.7 ps (B), 0.56 ns (C), and 6. 94 ns (D) for junctions with a radius of 0.5 μm.

FIGURE 37-A

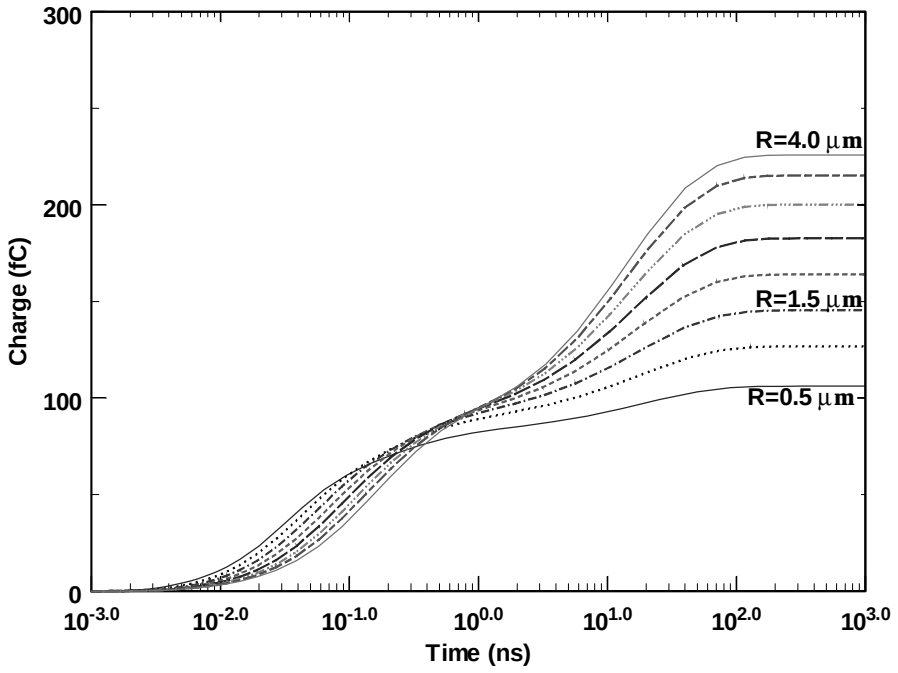

FIGURE 37-B

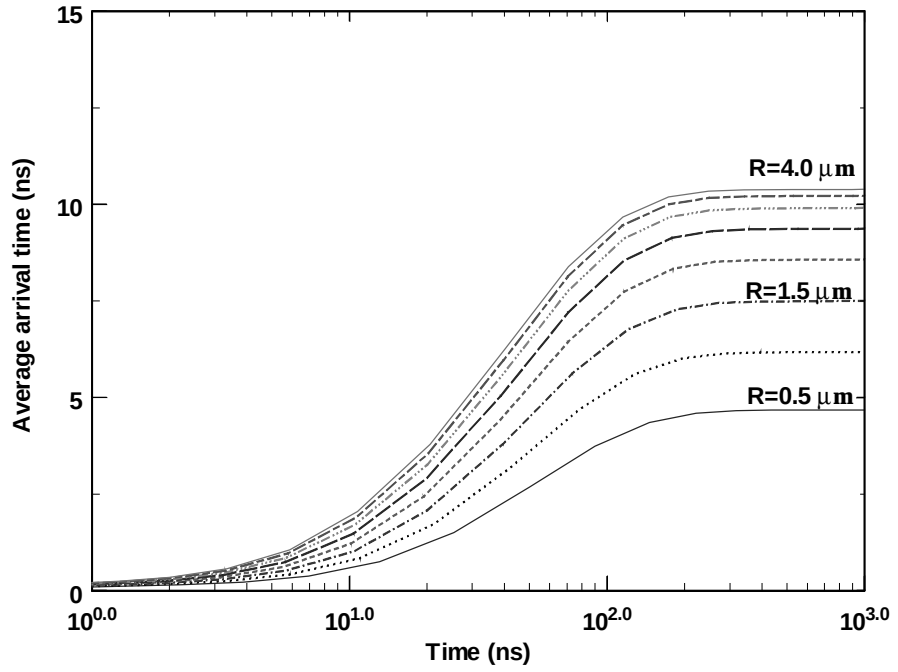

FIGURE 37. MEDICI simulation results for charge collection (A) and average arrival time (B) for junctions with different radii (0.5 to 4.0 μm step 0.5μm).

FIGURE 38-A

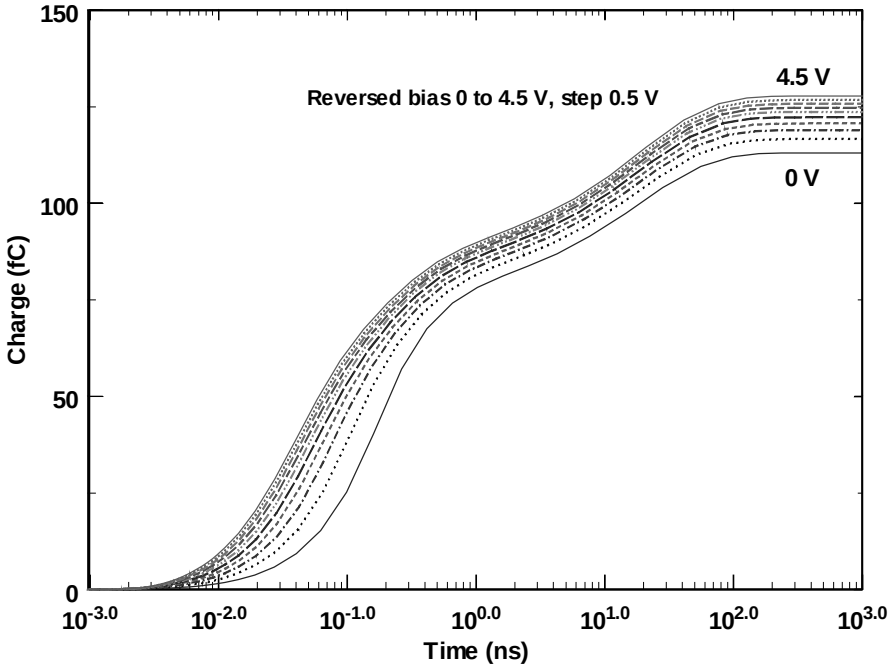

FIGURE 38-B

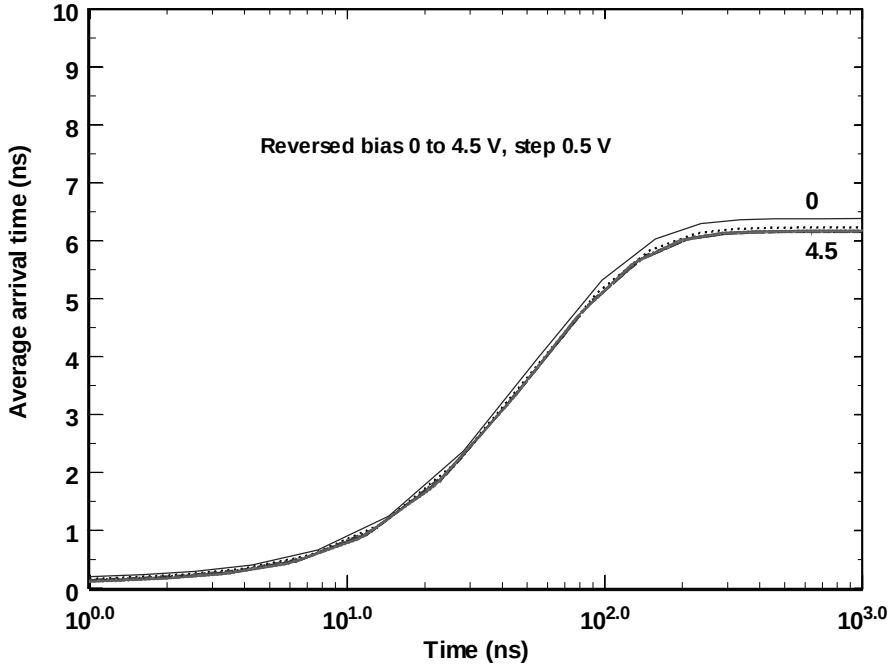

FIGURE 38. MEDICI simulation results for charge collection (A) and average arrival time (B) for junction with different reversed biases (0 to 4.5 V step 0.5 V). Junction radius is 1.0 μm.

REFERENCES

1. D. Binder, E.C. Smith, and A.B. Holman, *Satellite anomalies from galactic cosmic rays*, IEEE Trans. on Nucl. Sci. **NS-27**, No. 7, (1975), 2675.

2. T.C. May and M.H. Woods, *Alpha particle induced soft errors in dynamic DRAMs*, IEEE Trans. on Electron Devices **ED-26** (1979), 2.

3. G.C. Messenger and M. Ash, *The effects of radiation on electronic systems*, Van Nostrand Reinhold Company, New York, (1986).

4. C.M. Hsieh, P.C. Murley, and R.R. O'Brien, *Dynamics of charge collection from alpha-particle tracks in integrated circuits*, IEEE Inter. Rel. Phys. Sym. (IRPS) Proc. (1981), 38.

5. C.M. Hsieh, P.C. Murley, and P.R. O'Brien, *A field-funneling effect on the collection of alpha-particle-generated carriers in silicon devices*, IEEE Trans. on Electron Device Letter **EDL-2** (1981), 103.

6. C.M. Hsieh, P.C. Murley, and R.R. O'Brien, *Collection of charge from alpha-particle tracks in silicon devices*, IEEE Trans. on Electron Devices **ED-30** (1983), 686.

7. F.B. McLean and T.R. Oldham, *Charge funneling in N- and P-type Si substrate*, IEEE Trans. on Nucl. Sci. **NS-29**, No. 6, (1982), 2018.

8. L.D. Edmonds, *Electric currents through ion tracks in silicon devices*, IEEE Trans. on Nucl. Sci. **NS-45**, No.6, (1998), 3153.

9. J.F. Ziegler and J.P. Biersack, *SRIM-96: The Stopping and Range of Ions in Matter*, (1996), http://www.research.ibm.com/ionbeams/.

10. P.E. Dodd and F.W. Sexton, *Critical charge concepts for CMOS SRAMs*, IEEE **NS-22**, No. 6, (1995), 1764.

11. L.B. Freeman, *Critical charge calculations for a bipolar SRAM array*, IBM J. Res. Develop. **40**, No. 1, (1996), 119.

12. E.L. Petersen and P.W. Marshall, *Single event phenomenon in the space and SDI arenas*, J. Rad. Effects Res. Eng. **6**, No. 2, (1988), 1.

13. J. Barak, J. Levinson, A. Akkerman, M. Hass, M. Victoria, A. Zentner, D. David, O. Even, and Y. Liftshitz, *A new approach to the analysis of SEU and SEL data to obtain the sensitive volume thickness*, IEEE Trans. on Nucl. Sci. **NS-43**, No. 6, (1996), 907.

14. L.D. Edmonds, G. Swift, and A. Johnston, *Non-destructive measurements for CMOS devices using charge collection techniques*, IEEE Trans. on Nucl. Sci. **NS-43**, No.6, (1996), 2833.

15. C. Detcheverry, C. Dachs, E. Lorfevre, C. Sudre, G. Bruguier, J.M. Palau, J. Gasiot, R. Ecoffet, *SEU critical charge and sensitive area in a submicron CMOS technology*, IEEE Trans. on Nucl. Sci. **NS-44**, No. 6, (1997), 2266.

16. C. Detcheverry, R. Ecoffet, S. Duzellier, E. Lorfevre, G. Bruguier, J. Barak, Y. Lifshitz, J.M. Palau, and J. Gasiot, *SEU sensitive depth in a submicron SRAM technology*, IEEE Trans. on Nucl. Sci. **NS-45**, No. 3, (1998), 1612.

17. A.R. Knudson, A.B. Campbell, J.R. Hauser, M. Jessee, W.J. Stapor, and P. Shapiro, *Charge transport by the ion shunt effect*, IEEE Trans. on Nucl. Sci. **NS-33**, No. 6, (1986), 1560.

18. C.L. Axness, H.T. Weaver, and J.S. Fu, *Mechanisms leading to single event upset*, IEEE Trans. on Nucl. Sci. **NS-33**, No. 6, (1986), 1577.

19. C.L. Axness, J.R. Schwank, P.S. Winokur, J.S. Browning, R. Koga, and D.W. Fleetwood, *Single event upset in irradiated 16k CMOS SRAMs*, IEEE Trans. on Nucl. Sci. **NS-35**, No. 6, (1988), 1602.

20. J.A. Zoutendyk, E.C. Secrest, and D.F. Berndt, *Investigation of single event upset (SEU) in an advanced bipolar process*, IEEE Trans. on Nucl. Sci. **NS-35**, No. 6, (1988), 1573.

21. P.V. Dressendorfer, *Effects of radiation on microelectronics and techniques for hardening*, Nucl. Instr. and Meth. **B40/41** (1989), 1291.

22. B.W. Hughlock, G.S. LaRue, and A.H. Johnston, *Single event upset in GaAs E/D MESFET logic*, IEEE Trans. on Nucl. Sci. **NS-37**, No. 6, (1990), 1894.

23. V. Zajic, K. Kloesel, D. Ngo, P.M.Kibuule, A. Oladipupo, T.N. Fogarty, R.A. Kohler, and E.G. Strassinopulos, *Single event upset and total dose radiation effects on rad-hard SRAMs*, J. of Electronic Mat. **19** (1990), 689.

24. J.A. Zoutendyk, L.S. Smith and L.D. Edmonds, *Response of a DRAM to single ion tracks of different heavy ion species and stopping powers*, IEEE Trans. on Nucl. Sci. **NS-37**, No. 6, (1990), 1844.

25. O. Mausseau, J.L. Leray, V. Ferlet, A. Umbert, Y.M. Coic, and P. Hesto, *Charge collection mechanisms in MOS/SOI transistors irradiated by energetic heavy ions*, IEEE Trans. on Nucl. Sci. **NS-38**, No. 6, (1991), 1226.

26. M.P. Baze, W.G Bartholet, J.C. Braatz, and T.A. Dao, *Single event upset test structures for digital CMOS applications specific integrated circuits*, IEEE Trans. on Nucl. Sci. **NS-40**, No. 6, (1993), 1703.

27. A.O. Brown, B. Bhuva, S.E. Kerns, and W.J. Stapor, *Practical approach to determine charge collected in multi-junction structures due to the ion shunt effect*, IEEE Trans. on Nucl. Sci. **NS-40**, No. 6, (1993), 1918.

28. K. Gulati, L.W. Massengill, and G.R. Agrawal, *Single event mirroring and DRAM sense amplifier designs for improved single event upset performance*, IEEE Trans. on Nucl. Sci. **NS-40**, No. 6, (1994), 2026.

29. E. Normand, D.L. Oberg, J.L. Wert, J.D. Ness, P.P. Majewski, S. Wender, and A. Gavron, *Single event upset and charge collection measurements using high energy protons and neutrons*, IEEE Trans. on Nucl. Sci. **NS-41**, No. 6, (1994), 2203.

30. E. Normand, L.L. Oberg, J.L. Wert, and P.P. Majewski, *Comparison implications of charge collection measurements in silicon and InGaAs irradiated by energetic protons and neutrons*, IEEE Trans. on Nucl. Sci. **NS-42**, No. 6, (1995), 1815.

31. L.W. Massengill, *Cosmic and terrestrial single event radiation effects in Dynamic Random Access Memories*, IEEE Trans. on Nucl. Sci. **NS-43**, No. 2, (1996), 576.

32. J.F. Ziegler, H.W. Curtis, H.P. Muhlfeld, C.J. Montrose, B. Chin, M. Nicewicz, C.A. Russell, W.Y. Wang, L.B. Freeman, P.Hosier, L.E. LaFave, J.L. Walsh, J.M. Orro, G.J. Unger, J.M. Ross, T.J. O'Gorman, B. Messina, T.D. Sullivan, A.J. Sykes, H. Yourke, T.A. Enger, V. Tolat, T.S. Scott, A.H. Taber, R.J. Sussman, W.A. Klein, and C.W. Wahaus, *IBM experiments in soft fails in computer electronics (1978-1994)*, IBM J. Res. Develop. **40**, No. 1, (1996), 3.

33. T.J. O'Gorman, J.M. Ross, A.H. Taber, J.F. Ziegler, H.P. Muhlfeld, C.J. Montrose, H.W. Curtis, and J.L. Walsh, *Field testing for cosmic ray soft errors in semiconductor memories*, IBM J. Res. Develop. **40**, No. 1, (1996), 41.

34. J.F. Ziegler and G.R. Srinivasan, editors, special issue, IBM J. Res. Develop. **40**, No. 1, (1996).

35. V. Pless, Introduction to the theory of error-correcting codes, 3rd edition, Wiley-Interscience, New York, (1998).

36. A. Hasain and A. Ditali, *Building-in reliability: soft errors – a case study*, IEEE Inter. Rel. Phys. Sym. (IRPS) Proc., (1992), 276.

37. MIL STD883D, Method 1032.1.

38. J.F. Ziegler and W.A. Lanford, *Effect of cosmic rays on computer memories*, Science **206** (1979), 776.

39. J.F. Ziegler and W.A. Lanford, *The effect of sea level cosmic rays on electronic devices*, J. Appl. Phys. **52** (1981), 4305.

40. J.R. Letaw and E. Normand, *Guidelines for predicting single-event upsets in neutron environments*, IEEE Trans. on Nucl. Sci. NS-38, No. 6, (1991), 1500.

41. E. Normand and T.J. Baker, *Altitude and latitude variations in avionics SEU and atmospheric neutron flux*, IEEE Trans. on Nucl. Sci. **NS-40**, No. 6, (1993), 1484.

42. C.A. Gosset, B.W. Hughlock, M. Katoozi, G.S. LaRue, and S.A. Wender, *Single event phenomena in atmospheric neutron environments*, IEEE Trans. on Nucl. Sci. **NS-40**, No. 6, (1993), 1845.

43. T.J. O'Gorman, *The effect of cosmic rays on the soft error rate of a DRAM at ground level*, IEEE Trans. on Electron Devices **ED-41** (1994), 553.

44. E. Normand, *Single event upset at ground level*, IEEE Trans. on Nucl. Sci. **NS-43**, No. 6, (1996), 2742.

45. J.C. Pickel and J.T. Blandford, Jr., *Cosmic ray induced errors in MOS RAMs*, IEEE Trans. on Nucl. Sci. **NS-27**, No. 2, (1980), 1006.

46. W.R. McKee, H.P. McAdams, E.B. Smith, J.W. McPherson, J.W. Janzen, J.C. Ondrusek, A.E. Hyslop, D.E. Russell, R.A. Coy, D.W. Bergman, N.Q. Nguyen, T.J. Aton, L.W. Block, and V.C. Huynh, *Comic ray neutron induced upsets as a major contributor to the soft error rate of current and future generation DRAMs*, IEEE Inter. Rel. Phys. Sym. (IRPS) Proc. (1996), 1.

47. E.A. Amerasekera and F.N. Najm, *Failure mechanisms in semiconductor devices*, 2nd Edition, John Wiley & Sons, Chichester, (1997).

48. Semiconductor Industry Association (SIA), *The National Technology Roadmap for Semiconductors*, (1997).

49. S. Hayakawa, *Cosmic ray physics*, Wiley-Interscience, New York, (1969).

50. J.F. Ziegler, *Terrestrial cosmic rays*, IBM J. Res. Develop. **40**, No. 1, (1996), 19.

51. H.H.K. Tang, *Nuclear physics of cosmic ray interaction with semiconductor materials: particle-induced soft errors from a physicist's perspective*, IBM J. Res. Develop. **40**, No. 1, (1996), 91.

52. R.C. Baumann, T. Hossain, S. Murata and H. Kitagawa, *Boron compounds as a dominant source of alpha partilces in semiconductor devices*, IEEE Inter. Rel. Phys. Sym. (IRPS) Proc., (1995), 296.

53. T.R. Oldham, S. Murrill, and C.T. Self, *Single event upset of VLSI memory circuits induced by thermal neutrons*, J. Rad. Effects Res. Eng. **5**, No. 1, (1986), 6.

54. E.L. Petersen, *Nuclear reactions in semiconductors*, IEEE Trans. on Nucl. Sci. **NS-27**, No. 6, (1980), 1494.

55. S. El-Teleaty, P.J. McNulty, W.G. Abdel-Kader, and W.J. Beauvais, *Soft fails in microelectronic circuits due to proton induced nuclear reactions in materials surrounding the SEU sensitive volume*, Nucl. Instr. and Meth. **B40/41** (1989), 1300.

56. Y. Takami, F. Shiraishi, T. Goka, Y. Shimano, M. Sekiguchi, K. Shida, N. Kishida, H. Kadotani, T. Kikuchi, N. Hoshino, S. Murakami, H. Anayama, and A. Morio, *Investigation of single event upset subject to protons of intermediate energy range*, IEEE Trans. on Nucl. Sci. **NS-37**, No. 6, (1990), 1953.

57. J.F. Ziegler, H.P. Muhlfeld, C.J. Montrose, H.W. Curtis, T.J. O'Gorman, and J.M. Ross, *Accelerated testing for cosmic soft-error rate*, IBM J. Res. Develop. **40**, No. 1, (1996), 51.

58. E. Normand, D.L. Oberg, J.L. Wert, T.J. Baker, and C.M. Castaneda, *Considerations in single event upset testing with energetic neutrons*, presented at the Eighth Single Event Effects Symposium, LA, April, 1992.

59. T.J. Aton, J.A. Seitchik, S.D. Jantz, and H. Shichijo, *Accurate measurements of small charges collected on junctions from alpha particle strikes using an accelerator-produced microbeam*, IEEE Inter. Rel. Phys. Sym. (IRPS) Proc., (1995), 303.

60. T.J. Aton, J.A. Seitchik, and H. Shichijo, *Comparison of charge collection from energetic ions typical of neutron-recoil events with charge collection from alpha particle strikes*, IEEE Inter. Rel. Phys. Sym. (IRPS) Proc., (1996), 7.

61. T.J. Aton, J.A. Seitchik, S.H. Yang, and H. Shichijo, *Ion beam studies of events typical of soft errors in semiconductor memories*, Nucl. Instr. and Meth. **B130** (1997), 507.

62. K.M. Horn, P.E. Dodd, M.B.H. Breese, and B.L. Doyle, *Verification of three-dimensional charge transport simulation using ion microbeams*, Nucl. Instr. and Meth. **B130** (1997), 470.

63. P.T. McDonald, W.J. Stapor, A.B. Campbell, and L.W. Massengill, *Non random single event upset trends*, IEEE Trans. on Nucl. Sci. **NS-36**, No. 6, (1989), 2324.

64. J.F. Dicello, M. Paciotti, and M.E. Schillaci, *An estimate of error rates in integrated circuits at aircraft altitudes and at sea level*, Nucl. Instr. and Meth. **B40/41** (1989), 1295.

65. A.J. Tylka, W.F. Dietrich, P.R. Boberg, E.C. Smith, and J.H. Adams Jr., *Single event upsets caused by solar energetic heavy ions*, IEEE Trans. on Nucl. Sci. **NS-43**, No. 6, (1996), 2758.

66. D. Chlouber, P. O'Neill, and J. Pollock, *General upper bound on single event upset rate*, IEEE Trans. on Nucl. Sci. NS-37, No. 2, (1990), 1065.

67. J.R. Letaw, *Single event effects rate predictions in space*, Nucl. Instr. and Meth. **B56/57** (1991), 1260.

68. F.W. Sexton, *Microbeam studies of single event effects*, IEEE Trans. on Nucl. Sci. **NS-43**, No. 2, (1996), 687.

69. A.B. Campbell and A.R. Knudson, *Charge collection measurements for energetic ions in silicon*, IEEE Trans. on Nucl. Sci. **NS-29**, No. 6, (1982), 2067.

70. A.R. Knudson and A.B. Campbell, *Investigation of soft upsets in integrated circuit memories and charge collection in semiconductor test structures by the use of an ion microbeam*, Nucl. Instr. and Meth. **218** (1983), 625.

71. F. Watt, T. Osipowicz, T.F. Choo, I. Orlic, and S.M. Tang, *Nuclear microprobe analysis and imaging: current state of the art performance*, Nucl. Instr. and Meth. **B136-138** (1998), 313.

72. T. Kamiya, N. Utsunomiya, E. Minehara, R. Tanaka, I. Ohdomari, *Microbeam system for study of single event upset of semiconductor devices*, Nucl. Instr. and Meth. **B64** (1992), 362.

73. T. Kishimoto, H. Sayama, M. Takai, Y. Ohno, K. Sonoda, T. Nishimuar, A. Kinomura, Y. Horino, and K. Fujii, *Optimization of buried implanted layer in dynamic random access memories by soft error mapping and ion beam-induced current*, Nucl. Instr. and Meth. **B104** (1995), 515.

74. M. Koh, K. Horita, B. Shigeta, K. Igarashi, T. Matsukawa, T. Tanii, S. Mori, and I. Ohdomari, *Quantitative investigation of localized ion irradiation effects in n-channel metal-oxide-*

semiconductor field effect transistors using single ion microprobe, App. Phys. Lett. **68**, (1996), 3467.

75. T. Matsukawa, K. Noritake, M. Koh, K. Hara, M. Goto, and I. Ohdomari, *Single event upset test of static random access memory using single ion microprobe*, Japanese App. Phys. **31**, Pt. 1, No. 12A, (1992), 4025.

76. M. Takai, H. Sayama, H. Kimura, Y. Ohno, and S. Satoh, *Soft error immunity in a DRAM investigated by nuclear microprobes*, Nucl. Instr. and Meth. **B77** (1993), 344.

77. T. Matsukawa, A. Kishida, M. Koh, K. Hara, K. Horita, M. Goto, S. Matsuda, S. Kuboyama, and I. Ohdomari, *Identification of soft-error sensitive junction in SRAM's using a single ion microprobe*, IEEE Electron Device Lett. **EDL-15** (1994), 199.

78. H. Sayama, H. Kimura, Y. Ohno, K. Sonoda, N. Kotani, S. Satoh, and M. Takai, *Charge collection and soft error in DRAMs investigated using 400 keV proton microprobe*, Nucl. Instr. and Meth. **B85** (1994), 703.

79. H. Dussault, J.W. Howard Jr., R.C. Block, M.R. Pinto, W.J. Stapor, and A.R. Knudson, *High energy heavy ion induced single event transients in epitaxial structures*, IEEE Trans. on Nucl. Sci. **NS-41**, No. 6, (1994), 2018.

80. H. Dussault, J.W. Howard Jr., R.C. Block, W.J. Stapor, A.R. Knudson, P.T. McDonald, and M.R. Pinto, *High energy heavy ion induced charge transport across multiple junctions*, IEEE Trans. on Nucl. Sci. **NS-42**, No. 6, (1995), 1780.

81. M. Takai, T. Kishimoto, H. Sayama, Y. Ohno, K. Sonoda, T. Nishimura, A. Kinomura, Y. Horino, and K. Fujii, *Direct measurement and improvement of local soft error susceptibility in dynamic random access memories*, Nucl. Instr. and Meth. **B99** (1995), 562.

82. M. Takai, T. Kishimoto, Y. Ohno, H. Sayama, K. Sonoda, S. Satoh, T. Nishimura, H. Miyoshi, A. Kinomura, Y. Horino, And L. Fujii, *Soft error susceptibility and immune structures in Dynamic Radnom Access Memories (DRAMs) investigated by nuclear microprobe*, IEEE Trans. on Nucl. Sci. **NS-43**, No. 2, (1996), 696.

83. T. Matsukawa, S. Mori, T. Arimura, M. Koh, K. Igarashi, T. Sugimoto, and I. Ohdomari, *Evaluation of soft-error hardness of DRAMs under quasi-heavy ion irradiation using he single ion microprobe technique*, IEEE Trans. on Nucl. Sci. **NS-43**, No. 6, (1996), 2849.

84. B.L. Doyle, K.M. Horn, D.S. Walsh, and F.W. Sexton, *Single event upset imaging with a nuclear Microprobe*, Nucl. Instr. and Meth. **B64** (1992), 313.

85. K.M. Horn, B.L. Doyle, and F.W. Sexton, *Nuclear Microprobe Imaging of Single-Event Upsets*, IEEE Trans. on Nucl. Sci. **NS-39**, No. 1, (1992), 7.

86. M.B.H. Breese, P.J.C. King, G.W. Grime, and F. Watt, *Microcircuit imaging using an ion-beam-induced charge*, J. Appl. Phys. **72** (1992), 2097.

87. K.M. Horn, B.L. Doyle, F.W. Sexton, J.S. Laird, A. Saint, M. Cholewa, and G.J.F. Legge, *Ion beam induced charge collection (IBICC) microscopy of ICs: relation to single event upsets (SEU)*, Nucl. Instr. and Meth. **B77** (1993), 355.

88. F.W. Sexton, K.M. Horn, B.L. Doyle, J.S. Laird, M. Cholewa, A. Saint, and G.J.F. Legge, *Ion beam induced charge collection imaging of CMOS ICs*, Nucl. Instr. and Meth. **B79** (1993), 436.

89. M.B.H. Breese, G.W. Grime, and F. Watt, *The generation and application of ion beam induced charge images*, Nucl. Instr. and Meth. **B77** (1993), 301.

90. H. Schöne, D.S. Walsh, F.W. Sexton, B.L. Doyle, P.E. Dodd, J.F. Aurand, R.S. Flores, N.Wing, *Time Resolved Ion Beam Induced Charge Collection (TRIBICC) in micro-electronics*, Nucl. Instr. and Meth. **B158** (1999), 424.

91. J.C. Pickel, *Effect of CMOS miniaturization on cosmic ray induced error rate*, IEEE Trans. on Nucl. Sci. **NS-29**, No. 6, (1982), 2049.

92. P.E. Dodd, *Device simulation of charge collection and single-event upset*, IEEE Trans. on Nucl. Sci. **NS-43**, No. 2, (1996), 561.

93. G.F. Carey, W.B. Richardson, C.S. Reed, and B.J. Mulvaney, *Circuit, device and process simulation: mathematical and numerical aspects*, John Wiley & Sons, Chichester, (1996).

94. S. Velacheri, L.W. Massengill, and S.E. Kerns, *Single-event-induced charge collection and direct channel conduction in submicron MOSFETs*, IEEE Trans. on Nucl. Sci. **NS-41**, No. 6, (1994), 2103.

95. P.E. Dodd, F.W. Sexton, G.L. Hash, M.R. Shaneyfelt, B.L. Draper, A.J. Farino, and R.S. Flores, *Impact of technology trends on SEU in CMOS SRAMs*, IEEE Trans. on Nucl. Sci. **NS-43**, No. 6, (1996), 2797.

96. DAVINCI/MEDICI device simulation tools, Avant! Corporation, 46871 Bayside Parkway, Fremont, CA 94538, http://www.avanticorp.com/.

97. S.M. Sze, *Physics of semiconductor devices*, 2nd edition, Wiley-interscience, New York, (1981).

98. S.M. Sze, editor, *VLSI Technology*, 2nd edition, McGraw-Hill, New York, (1988).

99. J.W. Mayer and S.S. Lau, *Electronic Materials Science: For Integrated Circuits in Si and GaAs*, Macmillan, New York, (1990).

100. R.J. Baker, H.W. Li, and D.E. Boyce, *CMOS circuit design, layout, and simulation*, IEEE press, New York, (1998).

101. J.W. Jerome, *Analysis of charge transport: a mathematical study of semiconductor devices*, Springer, Berlin, (1996).

102. G.R. Srinivasan, P.C. Murley, and H.K. Tang, *Accurate, predictive modeling of soft error rate due to cosmic rays and chip alpha radiation*, IEEE Inter. Rel. Phys. Sym. (IRPS) Proc. (1994), 12.

103. G.R. Srinivasan, *Modeling the cosmic-ray-induced soft-error rate in integrated circuits: An overview*, IBM J. Res. Develop. **40**, No. 1, (1996), 77.

104. P.C. Murley and G.R. Srinivasan, *Soft-error Monte Carlo modeling program, SEMM*, IBM J. Res. Develop. **40**, No. 1, (1996), 109.

105. K.M. Kramer, W. Nicholas, and G. Hitchon, *Semiconductor devices – a simulation approach*, Prentice Hall, New Jersey, (1997).

106. H. Dussault, J.W. Howard Jr., R.C. Block, M.R. Pinto, W.J. Stapor, and A.R. Knudson, *Numerical simulation of heavy ion charge generation and collection dynamics*, IEEE Trans. on Nucl. Sci. **NS-40**, No. 6, (1993), 1926.

107. Y. Moreau, S. Duzellier, J. Gasiot, *Evaluation of the upset risk in CMOS SRAM through full three dimensional simulation*, IEEE Trans. on Nucl. Sci. **NS-42**, NO. 6, (1995), 1789.

108. R.L. Woodruff and P.J. Rudeck, *Three-dimensional numerical simulation of single event upset of an SRAM cell*, IEEE Trans. on Nucl. Sci. **NS-40**, No. 6, (1993), 1795.

109. P.E. Dodd, F.W. Sexton, and P.S. Winokur, *Three-dimensional simulation of charge collection and multiple-bit upset in Si Devices*, IEEE Trans. on Nucl. Sci. **NS-41**, No. 2, (1994), 2005.

110. P.E. Dodd, M.R. Shaneyfelt, and F.W. Sexton, *Charge collection and SEU from angled ion strikes*, IEEE Trans. on Nucl. Sci. **NS-43**, No. 6, (1997), 2256.

111. MEDICI user manual, Version 1999.2, Avant! Corporation.

112. T.T. Mnatsakanov, I.L. Rostovtsev, and N.I. Hilatov, *Investigation of the effect of nonlinear physical phenomena on charge carrier transport in semiconductor devices*, Solid State Electron., **30**, No. 6, (1987), 579.

113. M. Rosling, H. Bleichner, P. Jonsson, and E. Nordlander, *The ambipolar diffusion coefficient in silicon: dependence on excess-carrier concentration and temperature*, J. Appl. Phys. **76**, No. 6, (1994), 2855.

114. W. Shockley and W.T. Read, *Statistics of the recombination of holes and electrons*, Physical Review, **87** (1952), 835.

115. R.N. Hall, *Electron-hole recombination in germanium*, Physical Review, **87** (1952), 387.

116. M.B.H. Breese, D.N. Jamieson, and P.J.C. King, *Materials Analysis Using a Nuclear Microprobe*, Wiley-Interscience, New York, (1996).

117. J.R. Hauser, S.E. Diehl-Nagle, A.R. Knudson, A.B. Campbell, *Ion track effects in multi-junction structures*, IEEE Trans. on Nucl. Sci. **NS-32**, No. 6, (1985), 4115.

118. R.C. Martin, N.M. Ghoniem, Y. Song, and J.S. Cable, *The size effect of ion charge tracks on single event multiple bit upset*, IEEE Trans. on Nucl. Sci. **NS-34**, No. 6, (1987), 1305.

119. J.W. Howard Jr., R.C. Bolck, H. Dussault, W.J. Stapor, P.T. McDonald, A.R. Knudson, and M.R. Pinto, *A novel approach for measuring the radial distribution of charge in a heavy ion track*, IEEE Trans. on Nucl. Sci. **NS-41**, No. 6, (1994), 2077.

120. O. Musseau, V. Ferlet-Cavrois, A.B. Campbell, A.R. Knudson, and S. Buchner, *Application of an ion microbeam to determine the radial carrier density in an ion track*, Nucl. Instr. and Meth. **B146** (1998), 607.

121. O. Musseau, V. Ferlet-Cavrois, A.B. Knudson, S. Buchner, B. Fischer, and M. Schlogl, *Technique to measure an ion track profile*, IEEE Trans. on Nucl. Sci. **NS-45**, No. 6, (1998), 2563.

122. M.B.H. Breese, *A theory of ion beam induced charge collection*, J. Appl. Phys. **74** (1993), 3789.

123. L.D. Edmonds, *A simple estimate of funneling-assisted charge collection*, IEEE Trans. on Nucl. Sci. **NS-38**, No. 2, (1991), 828.

124. C. Hu, *Alpha particle induced field and enhanced collection of carriers*, IEEE Electron Device Letters **EDL-3**, No. 2, (1982), 31.

125. T.R. Oldham and F.B. McLean, *Charge collection measurements for heavy ions incident on n- and p-type silicon*, IEEE Trans. on Nucl. Sci. **NS-30**, No. 6, (1983), 4493.

126. T.R. Oldham and F.B. McLean, *Revised funnel calculations for heavy particles with high dE/dx*, IEEE Trans. on Nucl. Sci. **NS-33**, No. 6, (1986), 1646.

127. L.D. Edmonds, *Charge collection from ion tracks in simple EPI diodes*, IEEE Trans. on Nucl. Sci. **NS-44**, No. 3, (1997), 1448.

128. L.D. Edmonds, *The influence of spatial variation of diffusion length of charge collected by diffusion from ion tracks*, IEEE Trans. on Nucl. Sci. **NS-45**, No.1, (1998), 30.

129. F.W. Sexton, K.M. Horn, B.L. Doyle, M.R. Shaneyfelt, and T.L. Meisenheimer, *Effects of ion damage on IBICC and SEU imaging*, IEEE Trans. on Nucl. Sci. **NS-42**, No. 6, (1995), 1940.

130. D. Angell, B.B. Marsh, N.Cue, and J.W. Miao, *Charge collection ion microscopy: imaging of defects in with a positive ion microbeam*, Nucl. Instr. and Meth. **B44** (1989), 172.

131. M.B.H. Breese, G.W. Grime, and M. Dellith, *The effect of ion induced damage on IBIC images*, Nucl. Instr. and Meth. **B77** (1993), 332.

132. M. Takai, S. Hara, T. Kishimoto, and J. Yanagisawa, *Nuclear microprobe analysis of implantation damage induced by focused gallium ion beams in GaAs*, Nucl. Instr. and Meth. **B104** (1995), 524.

133. M. Jaksic, S. Fazinic, T. Tadic, M. Bogovac, I. Bodanovic, and Z. Pastuovic, *IBIC study of charge collection properties in Si(Li) detectors*, Nucl. Instr. and Meth. **B136-138** (1998), 1327.

134. R. Nipoti, C. Donolato, D. Govoni, P. Rossi, G.P. Egeni, and V. Rudello, *A study of He^+ ion-induced damage in silicon by quantitative analysis of charge collection efficiency data*, Nucl. Instr. and Meth. **B136-138** (1998), 1340.

135. T. Osipowicz, J.L. Sanchez, I. Orlic, F. Watt, S. Kolachina, D.S.H. Chan, and J.C.H. Phang, *Fluence dependence of IBIC collection efficiency of CMOS transistors*, Nucl. Instr. and Meth. **B136-138** (1998), 1345.

136. M.B.H. Breese, K.M. Horn, *The influence of ion induced damage on lateral charge collection and IBIC image contrast*, Nucl. Instr. and Meth. **B136-138** (1998), 1349.

137. M.B.H. Breese, A. Amaku, and P.R. Wilshaw, *A comparison between the use of EBIC and IBIC microscopy for semiconductor defect analysis*, Nucl. Instr. and Meth. **B136-138** (1998), 1355.

138. C. Manfredotti, F. Fizzotti, P. Polesello, E. Vittone, M. Jaksic, I. Bodganovic, and V. Valkovic, *Scanning ion beam microscopy: A new tool for mapping the transport properties of semiconductors and insulators*, CP392, Application of Accelerators in Research and Industry, edited by J.L. Duggan, I.L. Morgan, AIP press, New York, (1997), 705.

139. C. Manfredotti, F. Fizzotti, P. Polesello, E. Vittone, P. Rossi, G. Egeni, V. Rudello, M. Jaksic, I. Bodganovic, and V. Valkovic, *Proton microbeam investigations on electrical properties of natural and CVD diamond*, Nucl. Instr. and Meth. **B130** (1997), 491.

140. C. Manfredotti, F. Fizzotti, P. Polesello, E. Vittone, M. Truccato, A. Lo Giudice, M. Jaksic, and P. Rossi, *IBIC and IBIL microscopy applied to advanced semiconductor materials*, Nucl. Instr. and Meth. **B136-138** (1998), 1333.

141. M.B.H. Breese, A. Saint, F.W. Sexton, K.M. Horn, H. Schöne, B.L. Doyle, J.S. Laird, and G.J.F. Legge, *Optimization of ion-beam induced charge microscopy for the analysis of integrated circuits*, J. Appl. Phys. **77** (1995), 3734.

142. P.H.A. Mutsaers, *Nuclear microprobe design*, Nucl. Instr. and Meth. **B113** (1996), 323.

143. B.L. Doyle, N.D. Wing, and P.C. Peercy, *Nuclear microprobe analysis*, Microbeam analysis, H. Geiss ed., San Francisco press, (1981), 79.

144. B.L. Doyle, K.M. Horn, F.W. Sexton, J.S. Laird, A. Saint, M. Cholewa, and G.J.F. Legge, *Microbeam single event upset testing*, presented at the RADSCON-96 Short course on Space Environments and simulation for SEU tests, April 23, 1996, Prairie View A&M University, Prairie View, TX.

145. L.R. Doolittle, *Algorithms for the rapid simulation of Rutherford Backscattering spectra*, Nucl. Inst. Meth. **B9** (1985), 344.

146. F.D. McDaniel, B.N. Guo, S.N. Renfrow, M. El Bouanani, J.L. Duggan, B.L. Doyle, D.S. Walsh, and T.J. Aton, *Ion Beam Induced Charge Collection (IBICC) Studies on Integrated Circuits using 10 MeV carbon microbeam*, the 6th International Conference on Nuclear Microprobe Technology and Applications, Spier Estate, Stellenbosch, South Africa, 11-16 October 1998, Nucl. Instr. and Meth. **B158** (1999), 264.

147. B.N. Guo, S.N. Renfrow, B.L. Doyle, D.S. Walsh, T. J. Aton, M. El Bouanani, J.L. Duggan, and F.D. McDaniel, *Ion Beam Induced Charge Collection (IBICC) studies on the Integrated Circuits test structures using a 10 MeV carbon microbeam*, CP475, Application of Accelerators in Research and Industry, edited by J.L. Duggan, I.L. Morgan, AIP press, New York, (1999), 1121.

148. E. Takeda, K. Takeuchi, D. Hisamoto, T. Toyabe, K. Ohsihima, and K. Itoh, *A cross section of α-particle-induced soft-error phenomena in VLSI's*," IEEE Trans. on Electron Devices **ED-36** (1989), 2567.

149. Z. Shanfield, M.M. Moriwaki, W.M. Digby, J.R. Srour, and D.E. Campbell, *Characteristics of SEU current transients and collected charge in GaAs and Si devices*, IEEE Trans. on Nucl. Sci. **NS-32**, No. 6, (1985), 4104.

150. Nashiyama, T. Nishijima, H. Sekiguchi, Y. Shimano, and T. Goka, *Study of basic mechanisms of single event upset using high-energy microbeams*, Nucl. Instr. and Meth. **B54** (1991), 407.

151. T. Nashijima, H. Sekiguchi, S. Takeuchi, N. Shiono, H. Anayama, and A. Morio, *Study of basic mechanisms of single event upset in low-capacitance Si and GaAs diodes using high-energy microbeams*, Nucl. Instr. and Meth. **B104** (1995), 525.

152. T. Hirao, I. Nashiyama, T. Kamiya, and T. Nishijima, *Effects of micro-beam induced damage on single-event current measurements*, Nucl. Instr. and Meth. **B104** (1995), 508.

153. E.C. Smith, E.G. Stassinopoulos, K. LaBel, and C.M. Seidlick, *Application of a diffusion model to SEE cross sections of modern devices*, IEEE Trans. on Nucl. Sci. **NS-42**, No. 6, (1995), 1772.

154. L.D. Edmonds, *SEU cross sections derived from a diffusion analysis*, IEEE Trans. on Nucl. Sci. **NS-38**, No. 6, (1996), 3207.

155. J.A. Zoutendyk, H.R. Schwartz, and L.R. Nevill, *Lateral charge transport from heavy-ion tracks in integrated circuit chips*, IEEE Trans. on Nucl. Sci. **NS-35**, No. 6, (1988), 1644.

156. L.D. Edmonds, *Charge collected by diffusion from an ion track under mixed boundary conditions*, IEEE Trans. on Nucl. Sci. **NS-38**, No. 2, (1991), 834.

157. L.D. Edmonds, *A graphical method for estimating charge collected by diffusion from an ion track*, IEEE Trans. on Nucl. Sci. **NS-43**, No. 4, (1996), 2347.

158. B.L. Doyle, G. Vizkelethy, D.S. Walsh, B. Sehftinger, and M. Mellon, *A new approach to nuclear microscopy: the ion-electron emission microscope*, Nucl. Instr. and Meth. **B158** (1999), 6.

159. B.L. Doyle, private communications.

160. D. Bernarid, G.P. Egeni, F. Parere, M. Pegoraro, P. Rossi, V. Rudello, H. Somacal, E. Vittone, and M. Viviani, *Focused microbeam single event with a scintillating foil trigger and magnetic blanking*, Nucl. Inst. Meth. **B152** (1999), 377.

161. M. Takai, *Nuclear microprobe development and application to microelectronics*, Nucl. Instr. and Meth. **B85** (1994), 664.

162. M. Takai, *Application of nuclear microprobes to semiconductor process developments*, Nucl. Instr. and Meth. **B104** (1995), 501.

163. D.N. Jamieson, *Structural and electrical characterisation of semiconductor materials using a nuclear microprobe*, Nucl. Instr. and Meth. **B136-138** (1998), 1.